GENERALIZED PROCESSING OF FBG/FRP STRAIN DATA FOR STRUCTURAL HEALTH MONITORING

A THESIS SUBMITTED TO THE GRADUATE DIVISION OF THE UNIVERSITY OF HAWAIʻI AT MĀNOA IN PARTIAL FULFILLMENT OF THE REQUIREMENTS FOR THE DEGREE OF

MASTER OF SCIENCE

IN

CIVIL AND ENVIRONMENTAL ENGINEERING

MAY 2012

By

Gabriel L. Stockdale

Thesis Committee:

H. Ronald Riggs, Chairperson

Ian Robertson

David T. Ma

ACKNOWLEDGEMENTS

I would first like to thank the Hawai‘i Department of Transportation (HDOT) for both approving and financing the Salt Lake Boulevard Bridge Project, which was the primary catalyst for this work. I would also like to thank Dr. Gaur Johnson for his work in the development and installation of the SHM system applied to the Salt Lake Boulevard Bridge. Finally, I would like to thank my wife Dayana Stockdale for her continual encouragement and support, without which none of this would have been possible.

ABSTRACT

In order to promote the widespread application of sensor-based structural health monitoring (SHM) systems, complete and standardized systems need to be developed that are adaptable, can immediately begin to monitor the structure's performance to some degree, and be incorporated into the rehabilitation practices. The combination of fiber reinforced polymer (FRP) laminates and fiber Bragg grating (FBG) strain sensors have the potential to produce such a system for concrete structures. In this work, general processing procedures are developed that efficiently: (1) manage and process the recorded data; (2) ensure the recorded data is accurate and the sensors are working properly; and (3) monitor the limit states of the FRP laminates regardless of their application. The effectiveness of these procedures are then demonstrated through a case study involving the FBG instrumentation of a carbon FRP laminate rehabilitation applied to the Salt Lake Boulevard Bridge for shear strengthening.

TABLE OF CONTENTS

LIST OF TABLES

LIST OF FIGURES

LIST OF ABBREVIATIONS AND SYMBOLS

α – Thermal expansion coefficient

β – Noise amplification factor

ΔT – Change in temperature

ε – Strain

ε_{abs} – Absolute strain

ε_{absi} – Absolute strain of an individual set

ε_G – Global strain

ε_{GM} – Absolute global strain

ε_{GMi} – Global strain of an individual set

ε_L – Local strain

ε_{LM} – Absolute maximum local strain

ε_{LMi} – Maximum local strain of an individual set

ε_T – Absolute equivalent temperature strain

ε_{Ti} – Equivalent temperature strain of an individual set

Λ – Bragg grating period

λ – Wavelength

λ_B – Bragg wavelength

ξ – Thermo-optic coefficient

ρ_e – Effective photo-elastic constant

AASHTO – American Association of State Highway Transportation Officials

c – Maximum difference between any two adjacent data points in a dataset

DLAC – Damage Localization Assurance Criterion

FBG – Fiber Bragg grating

FOS – Fiber optic sensor

FRP – Fiber reinforced polymer

LRFD – Load and Resistance Factor Design

LT – Long term

N – Total number of data points in a dataset

n – A subset of data points in a dataset

NCHRP – National Cooperative Highway Research Program

n_{eff} – Effective refractive index

NWC – Null wavelength calculator

RC – Reinforced concrete

SHM – Structural health monitoring

SLBB – Salt Lake Boulevard Bridge

SRH – Steel rod hanger

ST – Short term

T1 – Threshold strain level one

T2 – Threshold strain level two

UV – Ultra violet

CHAPTER 1. INTRODUCTION

1.1 Background

Over the past two decades, the investigation and application of sensor-based structural health monitoring (SHM) systems to civil structures has gained the attention of many researchers across the globe. The definition of SHM has adapted over time but is currently accepted as the use of "in situ, continuous or regular (routine) measurement and analysis of key structural and environmental parameters under operation conditions, for the purpose of warning of impending abnormal states or accidents at an early stage, as well as giving maintenance and rehabilitation advice*"* [1]. The reason for this recent attention into the application of SHM systems to civil structures can be attributed to: (1) the continued technological advancements in data transmission and storage capabilities which has made it possible to transfer and store mass amounts of data with relative ease; (2) the development and refinement of new sensor systems based on fiber optic technologies, which provide many advantages to their traditional counterparts; and (3) the development of new composite materials, known as fiber reinforced polymers (FRPs), which has both fueled the application of sensor systems to civil structures in order to observe the long term performance of these composite materials [2–4], as well as providing a packaging system for the fiber optic sensors (FOSs) [5].

FOSs has many favorable attributes for their application in SHM systems. They are small, highly precise and stable, provide a wide range of linear response to strain and temperature, are electrically passive and immune to electromagnetic interference, and can be multiplexed and incorporated into large sensor networks [5-6]. In the application to civil structures, FOSs have been used to measure strain, temperature, load, pressure, acceleration, rotation, displacement, concrete cracking, and the monitoring of the corrosion of reinforcement [1, 6–8]. Of the different FOS technologies and applications, Fiber Bragg Grating (FBG) point sensors, used for measuring strain, have been the most frequently used system applied to bridges and civil structures [6, 9]. The reasons for the popularity of FBG sensors, when compared to other fiber sensor schemes, are that they have a relatively low cost, good linearity, and are resistant to harsh environments and the transduction mechanism. They also have the capacity for wavelength multiplexing. With over two decades of active research and development behind them the technology is on the verge of maturity [9]. Furthermore, FBG sensors have the ability to be attached to the surface of the structure at any time or imbedded within the structure during its construction [9].

The use of FRP laminates for the rehabilitation of existing concrete structures has become an attractive alternative to many of the traditional methods. FRP systems have a high tensile strength to weight ratio, high stiffness, low maintenance costs, and are resistant to corrosion and quick to install [10–12]. FRPs were originally developed for uses in the defense and aerospace industries, but the increase in their production and reduction in manufacturing costs prompted their application to civil engineering structures [13]. The accepted application of FRPs requires that the long-term in-service reliability be established. This has promoted the application of sensor-based SHM systems for the purposes of monitoring the long-term performance of in-service FRP rehabilitations, and to provide ample warning against the possible debonding failure of the fabric from the concrete [12]. FOS became a broadly accepted SHM device for FRP materials [14]. Furthermore, the small fiber size of FOSs allows them to be embedded in between the fiber layers of the FRPs allowing the FRP to act as a packaging material for the FOSs.

1.2 Problem Statement

Although the number of civil structures in the United States being implemented with sensor based SHM systems continues to increase, the widespread application of these systems still faces several challenges. First, civil structures are large, highly complex systems designed using a set of theoretical assumptions, mathematical simplifications, and safety implementations to withstand a semi-fictitious set of loading conditions based on the size, location, and functionality of the structure. The result of this is that each structure is a unique, one-of-a-kind system whose behavior may or may not act as predicted. Second, the development of sensor based SHM systems for civil structures requires the long-term testing of the systems applied to actual structures. The result of this is that all of the equipment required to operate these systems has to be solely invested to each system, which ultimately increases the cost of developing these SHM systems. Finally, the development of sensor based SHM systems has been driven by a “technology push” rather than by an “applications pull” [15]. The result of this push is that the collection of the data from the implementation of these technologies has been the primary emphasis. Consequently, data management and problem identification techniques necessary for the widespread application of SHM systems have all but been ignored.

The result of these challenges is that no standardizations for the sensor packaging or for the application procedures of SHM systems has been established [9]. Furthermore, the application of SHM systems in capitalistic societies, such as the United States, faces the problem of the “chicken and the egg”. Since the actual behavior of a structure is both unique and unknown, the

potential success of a sensor application scheme is difficult to predict. The actual behavior of the structure can be determined after an initial implementation of some sensors, at which point an application scheme can be established. However, the funding for the initial implementation of the system will only occur after the potential of the system is demonstrated to lie within a justifiable level of investment risk. Therefore, the widespread application of sensor based SHM system to the nation's infrastructure requires the establishment of standardized systems that are adaptable and provide some level of guaranteed monitoring performance regardless of the behavior of the structure.

1.3 Motivation

As of 2011, 24% of the 600,000 plus bridges in the United States are labeled as structurally deficient or functionally obsolete based on the reporting of the Federal Highway Administration (FHWA). With the limited resources allocated to the rehabilitation of the nations crumbling infrastructure, it is imperative that the rehabilitation measures taken not only fix the observed problems, but also take advantage of the current technologies to increase the efficiency in the detection and prioritization of future deficiencies that will undoubtedly occur. The implementation of sensor systems has the potential to aid in the maximization of future rehabilitation measures and in the prioritization of these limited resources.

1.4 Objectives

In order to promote the widespread application of sensor based SHM systems to the nations crumbling infrastructure, complete and standardized SHM systems need to be developed that are adaptable to a wide range of applications, have the ability to immediately monitor the structure's performance to some degree, and be incorporated into the rehabilitation of the structure. It is the objective of this thesis to demonstrate that the combination of FRP laminates and FBG sensors, coupled with the appropriate data management, post-processing, and analysis procedures can produce such a standardized SHM system.

1.5 Thesis Outline

This thesis begins with a general discussion on SHM, the challenges facing its widespread application, and the need to create standardized adaptable SHM systems—all addressed in Chapter 1. Chapter 2 presents a literature review on the application of FBG sensors to civil

infrastructures, the role that FRPs have played in the development of SHM as well as a brief discussion on the development of damage detection algorithms. A background on some of the properties and failure modes of FBGs and FRPs is presented in Chapter 3, followed by the proposed SHM data management, post-processing, and analysis procedures in Chapter 4. Finally, Chapter 5 presents a case study on the application of the algorithms to the data obtained from the instrumentation of the Salt Lake Boulevard Bridge located in Honolulu, Hawai‘i. Chapter 6 concludes this work.

CHAPTER 2. LITERATURE REVIEW

In this chapter, a review on the application of FBG sensors to civil infrastructures is presented in section 2.1. Section 2.2 then presents the role that FRPs have played in the advancement of SHM, followed by a brief discussion on the development of damage detection algorithms in section 2.3. This chapter is then wrapped up with a final discussion in section 2.4.

2.1 FBG Sensor Applications to Civil Infrastructures

The application of FBG sensors to civil infrastructure projects for the purpose of SHM has been occurring for approximately two decades. Through these applications, the versatility, durability, longevity, and the real-time monitoring capability of FBG strain sensors has been established.

FBG sensors have been successfully applied in the field to a number of materials, such as aluminum and concrete [16]; steel strand, carbon fiber composite cables, and leadline rod prestressing tendons [17]; and most importantly for this work, FRP laminates [4, 18]. FBG sensors have been imbedded into the structures they are monitoring, either directly [19], or as part of a transducer [6]. They have also been mounted to the surface of the structure [4], or in grooves cut into the surface [2]. This wide range of successful applications demonstrates the versatility of FBG sensors.

The durability and longevity can be best seen in the 1998 rehabilitation of the Ste-Émélie-de-l'Énergie bridge [4]. The beams of the Ste-Émélie-de-l'Énergie bridge were strengthened with FRP laminates and instrumented with both the conventional resistive strain gauges as well as FBG and Fabry-Perot sensors. Collection of data was not continuous but in order to assess the long-term behavior of the FOSs, load tests were performed prior to the rehabilitation, immediately afterwards, one year later, and finally six years after the initial instrumentation in 2004. Over the course of these six years the system was exposed to a temperature variation of 54 ºC from -22 ºC to +32 ºC. The recorded measurements from the FOSs during load tests were validated by way of metal foil strain gauges, and after six years of operation, all of the FOSs were still in good working condition. In addition to the Ste-Émélie-de-l'Énergie bridge project, Kister et al. [20] reports the 100% survival rate over the three years of monitoring of the application of FBG sensors to Europe's first all-fiber reinforced bridge, the West Mill Bridge; and Schultz et al. [2] reports the successful two year monitoring of twenty-six FBG sensors applied to the Horsetail Falls Bridge in Oregon.

Finally, successful real-time monitoring and online presentation has been accomplished for both the instrumentation of six beams and six columns in a newly constructed building at the University of Colorado by Saouma et al. [16], and the FBG based transducer instrumentation of the Lezíria Bridge in Portugal [6].

2.2 FRP's Role in the Advancement of SHM

The use of FRP composites in both the construction and rehabilitation of civil structures has continued to increase in popularity for several decades. The amount of work published on this topic is both extensive and exhaustive as can be seen by Hollaway's 2010 review [21] on the present and future utilization of FRP composites, which references over 200 publications. In 2011, the National Cooperative Highway Research Program (NCHRP) published NCHRP Report 678 [10], which establishes the design methods and specifications for the design of FRP systems for strengthening concrete girders in shear. The intention of these specifications are for the incorporation into the AASHTO LRFD Bridge Design Specifications [22]. The advancements in the development and application of FRP composites is beyond the scope of this work, but it is important to note that their use is becoming more accepted and that design standards do exist.

What is important to this work is the role that FRP composites, and more specifically FRP laminates, have played in the advancement of sensor based SHM. Early laboratory testing continued to demonstrate the potential in FRP's ability to strengthen and rehabilitate reinforced concrete (RC), but their long-term performance in the field could not be addressed through laboratory testing. Consequently, the desire to understand the long-term performance created a tangible objective for the application of sensors to civil structures. The instrumentation of the Ste-Émélie-de-l'Énergie bridge [4] and the Horsetail Falls Bridge [2] discussed in the previous section, as well as the instrumentation of an I90 overpass in Illinois [3], are some examples where the application of a sensor based SHM system were deployed for the purpose of monitoring the long-term behavior of FRP laminates. Furthermore, the instrumentation of the Salt Lake Boulevard Bridge, which is the focus of the case study presented in Chapter 5, was developed for the same purpose.

The second role that FRP laminates play in the advancement of sensor based SHM system is as a packaging system. Bare fiber FBG sensors are extremely fragile and need to be packaged to improve their robustness and ensure they are not damaged during the installation process. Kister et al. [20] performed pullout tests on FOSs bonded on bridge coupons using cyanoacrylate glue and epoxy-based adhesives under both wet and dry conditions to aid in the instrumentation of the West Mill Bridge. These pullout tests highlighted the stability of the

adhesives and the 100% survival rate of the sensors installed on the West Mill Bridge demonstrates the robustness of the adhesive FOS system. Although FRP laminates were not part of the investigation performed by Kister et al., the application of FBG's to FRP laminates is carried out through the application of adhesives, or with the thermosetting polymer resins of the FRP. The highlighted stability can therefore be transferred to these systems. Torres et al. [5] investigate an FRP based packaging system, through a finite element based numerical study, for the surface mounting of FBG sensors. This system consists of FBG sensors that are protected by layers of glass FRP with the FBG placed on one of the packaging surfaces so that the sensor is as close as possible to the monitoring surface. The results of the numerical study demonstrates that the thickness and Poisson's ratio of the adhesive used to attach the package hardly affects the recorded data, but the presence of a packaging layer between the sensor and mounting surface can introduce errors as much as 15%.

2.3 SHM Damage Detection

Recent works focusing on damage detection techniques have begun to emerge. These damage detection algorithms tend to be highly complex and require either a numerical model of the system, or the training of the system. The recently developed algorithm by Hickmann et al. [23] which integrates a decentralized computing architecture with the Damage Localization Assurance Criterion (DLAC) algorithm in order to obtain a *holistic* approach to SHM, and also the FBG based *generic algorithm-support vector regression* algorithm developed by Zhang et al. [24] are two examples requiring numerical models. The three-way analysis method developed by Prada et al. [25] is a method which requires the training of the system. Although these systems have demonstrated their ability to detect and locate damage, they have emerged before the general acceptance and widespread application of SHM to civil structures has commenced. The result is that the increased time and resources, or in other words the increased cost, needed to implement these damage detection algorithms will hinder the promotion of SHM.

2.4 Discussion

The main areas of SHM research have been on data acquisition, feature extraction, and data reduction techniques [15, 26]. The management, post-processing, and analysis preparation of the obtained data, which are often the most tedious and time consuming aspects, generally hold little to no scientific value, and as a consequence they are combined with the analysis

procedure or omitted entirely from the publications. All of the mentioned works in this chapter fall into this category, but the widespread application of SHM to civil structures requires that these aspects be addressed.

CHAPTER 3. FBG AND FRP BACKGROUND

The focus of this chapter is to present a background on FBG and FRP laminates and to describe some of their associated properties and failure modes. Section 3.1 and 3.2 focus separately on FBG sensors and FRP laminates respectively, while section 3.3 addresses some features associated with the combination of the two.

3.1 FBG Sensors

FBG's are developed by exposing a short segment of an optical fiber to intense UV light. This exposure creates what are known as *Bragg gratings*, which are periodic variations in the refractive index at the core of the optical fiber [5, 9]. When light is transmitted through the modified optical fiber, the spacing of the *Bragg gratings*, coupled with the change in the refractive index, causes an amplified reflection of a narrowband wavelength, known as the *Bragg wavelength,* while the remainder of the transmitted light passes unaffected (see Figure 3.1).

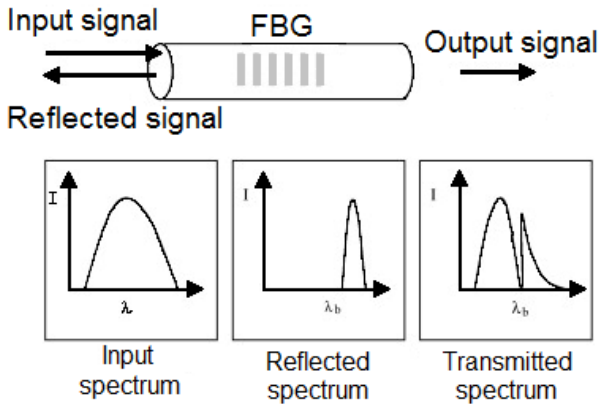

Figure 3.1. Transmission and reflection spectra from an FBG [9]**.**

The equation for the Bragg wavelength, λ_B, is

$$\lambda_B = 2n_{eff}\Lambda \tag{3.1}$$

where n_{eff} and Λ are the effective refractive index and the grating period of the FBG, respectively. The introduction of strains or temperature changes to the FBG causes the grating

period to change, resulting in a shift in λ_B. Ignoring higher order effects, the relationship between the longitudinal strain, ε, and temperature change, ΔT, can be expressed as;

$$\frac{\lambda-\lambda_B}{\lambda_B} = (1-\rho_e)\varepsilon + (\alpha+\xi)\Delta T \quad (3.2)$$

In (3.2), λ is the recorded wavelength, α is the thermal expansion coefficient, ξ is the thermo-optic coefficient, and ρ_e is the effective photo-elastic constant (equal to 0.2148 [27]).

One of the distinct advantages of FBGs is that the Bragg wavelength is a narrowband wavelength. This ability allows the sensors to be multiplexed, or multiple FBGs can be created on a single optical fiber [28]. When FBGs are multiplexed, the allowable range in the shift of the Bragg wavelength is then dependent upon the spacing between the individual Bragg wavelengths. If the Bragg wavelength's of any two gratings becomes too close, then the gratings will interfere and the data will be distorted.

It is also important to note that there exists the potential for the FBG to "drift". It has been stated that a clear definition of the sensor drift is needed [29], but cyclic loading tests have demonstrated that this drift is not extreme, and no trend line could be connected to this variation [30].

3.2 FRP Laminates

FRP laminates consist of high-strength and stiffness fibers protected by a high-performance thermosetting polymer [21]. The mechanical characteristics are entirely derived from the fibers. The typical fibers used are glass, carbon, or aramid, and their typical tensile mechanical properties are listed in Table 3.1. Although all the details of these mechanical properties will not be discussed, it is important to note the high ultimate strain values associated with these different fibers. The primary role of the polymer is to bind and hold the fibers in their required position, but the polymer also provides environmental and damage protection as well as adding to the overall toughness of the composite [21]. Polyester, vinyl-ester, and epoxy are the typical thermosetting polymers used for civil engineering applications.

FRP laminates' behavior in tension is linear elastic until sudden failure. In compression, the behavior is not well understood. The reason for this lack of understanding is due to the early onset of buckling due to the high aspect ratios of the laminates. The common failure modes of FRP laminates are axial tension rupture, transverse tension rupture, shear rupture, composite buckling, plastic microbuckling, and fiber buckling [31].

Normally the application of FRP laminates for rehabilitation and/or strengthening is done such that the applied loads are picked up axially along the fiber length. The result is that transverse tension rupture, shear rupture, and plastic microbuckling (which requires in-plane bending) do not control. Furthermore, the strength of the commonly used thermosetting polymers is sufficient to ensure that the local fiber buckling does not control. The primary failure modes for typical application scenarios can therefore be reduced to axial tension rupture and composite buckling.

In addition to the failure modes associated with the FRP laminates' themselves, a system failure mode of delamination or peel arises with the bonding of the laminates to concrete. This failure mode can arise from a failure in the adhesive itself, continual peel from the movement of preexisting cracks, peel from the attempted composite buckling of the laminate from compressive loading, or tensile/shear failure of the surface layer of concrete. The bond between the laminates is critical for the transfer of stresses. Initial localized delamination, which exists at the location of preexisting cracks in the concrete, is not an issue, but if the delamination propagates from peel the ability to transfer stress is lost. If stress cannot be transferred then the system has failed.

3.3 Combining FBG and FRP

The properties of FBG sensors and FRP laminates have been individually discussed in the previous sections, but it is also important to consider them in combination. First, when the FBGs are packaged in the FRP, the heat generated during the hardening of the thermosetting polymer will produce a small shift in the Bragg wavelength [5]. Second, the external application of FBGs onto the surface will exhibit some degree of pre-tensioning arising from such possibilities as excess hanging fiber, assuring the fiber is flush with the mounting surface, or from the hardening of the adhesive, which will also produce a small shift in the Bragg wavelength. Finally, the additional failure mode of debonding between the FBG and the FRP is introduced. Although this failure mode does not affect the structural integrity of the system, it does affect the integrity of the SHM system.

Table 3.1. Typical tensile mechanical properties of glass, carbon, and aramid fibers [21]**.**

Material	Fiber	Elastic modulus $x10^3$ ksi (GPa)	Tensile strength ksi (MPa)	Ultimate strain %
Glass fiber	E	10 (69)	350 (2400)	3.6
	A	10 (69)	540 (3700)	5.4
	S-2	12 (86)	500 (3450)	4
Carbon fiber				
Pan based fibers				
Hysol Grafil Apollo	HM[a]	44 (300)	750 (5200)	1.73
	UHM[b]	65 (450)	510 (3500)	0.78
	HS[c]	38 (260)	728 (5020)	1.93
BASF Celion	G-40-700	44 (300)	719 (4960)	1.66
	Gy 80	83.0 (572)	270. (1860)	0.33
Torayca	T300	33.9 (234)	512 (3530)	1.51
Pitch based fibers				
Hysol union carbide	T-300	33.00 (227.5)	400.0 (2758)	1.76
	T-500	35.00 (241.3)	500.02 (3447.5)	1.79
	T-600	35.00 (241.3)	600.0 (4137)	1.8
	T-700	36.00 (248.2)	660.02 (4550.7)	1.81
Aramid fiber	49	18.1 (125)	400. (2760)	2.2
	29	12 (83)	399 (2750)	3.3

a High-modulus (American definition is known as intermediate modulus).

b Ultra-high-modulus (American definition is known as intermediate modulus).

c High-strength

CHAPTER 4. PROCEDURES

It is stated in Chapter 1 that the objective of this thesis is to create a standardized SHM system based on the combination of FRP laminates and FBG strain sensors. In Chapter 2, the ability for long-term monitoring is demonstrated, but it is also expressed that there exists a lack of attention on the management, post-processing, and analysis preparation of the data. Therefore, the intent of this chapter is to develop a set of simplified procedures and algorithms that address the issues of data management, post-processing, and analysis such that the implementation of a FBG/FRP based SHM system can quickly begin to monitor the performance of the structure.

4.1 Objectives and Assumptions

Before the SHM algorithms are presented it is important to understand the objectives and assumptions behind their development.

4.1.1 Objectives

The primary objective is not to obtain precise measurements, but to monitor the behavior of the structure and ensure that the system is working properly. The owner of the structure is usually only going to be concerned about the detection of suspect behaviors and excessively large values, at which point a crew can be sent to examine the structure and/or a deeper examination of the data can be authorized.

The second objective is to simplify the processing of the data to serve two functions. The first function is that the processing will be easier to understand. In the US, it is often the elected officials, such as a city mayor or state governor, who have the ability to initiate bonds and/or allocate the funding required for the widespread implementation of SHM systems. These individuals, more often than not, are not well versed in engineering. Therefore, the easier it is to understand the system, the better the chances are in convincing the decision makers to implement the system. The second function of simplifying the processing of the data is to reduce the amount of training required for the personnel who will be responsible for the monitoring, which will ultimately reduce the overall cost of the system.

The final objective of the algorithms is to establish a database that is easy to navigate. The implementation of a long-term SHM system will undoubtedly produce massive amounts of data, which for the foreseeable future will require some level of human inspection. It is therefore imperative that the data is easily and intuitively navigable.

4.1.2 Assumptions

The assumptions used in the development of the algorithms are:

1. The short-term (ST) and long-term (LT) effects on the structure are independent for the purposes of data processing.
2. The fundamental Bragg wavelength for the LT effects is a fixed value established from the first recorded dataset.
3. The fundamental Bragg wavelength for the ST effects is a floating value.

There are two key reasons for the establishment of these assumptions. The first reason is to create the ability to calculate a ST strain record, ε_L, that captures the dynamic loading features of the structure without requiring the application of compensation techniques from the LT effects. The second reason is to establish a LT strain record, ε_G, that incorporates all of the long term effects, whether it is an actual strain or a fictitious strain caused by temperature changes, without the ST dynamic effects so that LT patterns can more easily emerge.

4.2 Procedures

The procedures developed in this section consist of a combination of automated and manual components. Due to the mass amounts of data that will be produced with any LT SHM system, it is absolutely necessary that the data management (section 4.2.1) and post-processing (section 4.2.2) procedures be automated. The manual components are the examinations of the behavior of the data. Although the ideal situation would be to have all of the procedures automated, there does exist a level of judgment in examining the behavior of the system that may be difficult to automate.

In the following procedures and algorithms, the term ***local*** is used in regards to aspects associated with individual datasets, and the term ***global*** is used in regards to aspects associated with all of the datasets. Furthermore, all of the data files are saved as text files in a delimited (either tab or comma) format. If the original files are not in this format, it is recommended that they be converted before commencing with the following procedures.

4.2.1 Data Management

The start of the data management begins with the creation of three folders labeled input, global, and local. The input folder consists of all the unprocessed data. The global folder will house the global files, and the local folder will be where all of the local folders and files are stored.

If the data is collected continuously, then cut it into segments such that there is no change in temperature. Take care on where the data is cut so no ST loading events are divided. This division of the data will also be performed for systems that undergo long term periodic sampling. The data is then checked for time steps larger than the sampling rate. If this occurs, split the dataset.

Next, take the first time value, which is guaranteed to be unique for every dataset, and establish it as the timestamp for that dataset. Use this timestamp in the naming of all the local files and folders, as well as for the cataloging of global values and statistical calculations.

Save the original dataset in the newly created folder under a name such as “project name_timestamp_original.txt”. It is recommended to use a human readable format for the timestamp used in the file and folder naming so it is easier to navigate manually.

The final step before commencing with the post-processing is to remove any unnecessary information in the datasets that may have been carried over from the interrogator, and to rearrange the data columns, with time being the first column, into an order that is more intuitive to the project. Also, localize the time so that each file starts with an initial time step of zero. If it is ever necessary to know the exact time a certain event occurred, simply add the local time to the timestamp. Save this new file as “project name_timestamp_wave.txt” in the appropriate timestamp folder.

4.2.2 Post-Processing

The first step in the post-processing of the data is to establish the null wavelength. The Null Wavelength Algorithm (see 4.2.2.1) provides an automated method to establish a unique null wavelength calculator (NWC) for the system. For the best results, it is recommended that two or three datasets that exhibit typical ST variations be used in the establishment of the NWC, but this is not necessary as the parameters can be updated and the datasets recalculated at any time.

After the null wavelength calculator is established, use it to calculate the null wavelength and standard deviation of all of the sensors in the data set. Save these wavelength and standard deviation values in the “project name_null_wave.txt” and “project name_null_stdev.txt” located in the global folder respectively. Make sure the values are cataloged with the timestamp of their dataset.

The next step is to calculate the local strains. Removing the temperature from (3.2), rearranging the terms, and inputing ρ_e gives:

$$\varepsilon = \frac{\lambda - \lambda_B}{0.7852\lambda_B} \quad (4.1)$$

The temperature can be removed since the local files are established in a manner that guarantees the temperature is constant. Use (4.1) to calculate the local strains by setting λ_B equal to the calculated null wavelength. Save the calculated strains as “project name_timestamp_strain.txt” in the appropriate local timestamp folder. Also determine the maximum and minimum local strain values. Save these values in the “project name_local_max.txt” and “project name_local_min.txt” files in the global folder, again making sure the records are cataloged with their timestamp.

The final step in the post-processing procedure is to calculate the “fictitious” global strain using (4.1). The term fictitious is used to express the fact that the calculated global strains ignore the effects of temperature. This time, set λ equal to the null wavelength of the dataset currently being processed and set λ_B equal to the first recorded null wavelength. Save these global strain values in the “project name_global_strain.txt” file in the global folder, as always making sure the records are cataloged with their timestamp.

Once the data management and post-processing is established, the database’s file tree should look similar to Figure 4.1.

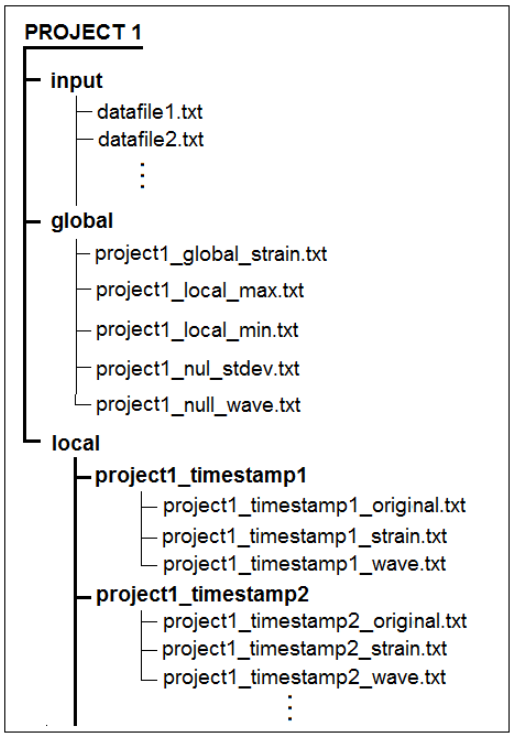

Figure 4.1. File tree which results from the data management and post-processing procedures.

4.2.2.1 Null Wavelength Algorithm

The algorithm to determine the null wavelength, i.e., the wavelength to define zero strain in a given dataset, assumes that a section of the dataset corresponds to zero strain during which no 'event' is occurring. Therefore, the first step to determine the null wavelength for a dataset is to identify the data points that are not associated with an event. An event is characterized as any progressive change in the recorded data values. To do this, take the difference, B_j, of each two adjacent data points of dataset $\boldsymbol{A}$:

$$B_j = A_{j+1} - A_j\Big|_{j=1}^{j=N-1} \tag{4.2}$$

where N is the number of data points in the set. Then determine the absolute value of the maximum difference, c, from all of the calculated differences in the set $\boldsymbol{B}$:

$$c = \max\left(\left|B_j\right|\Big|_{j=1}^{j=N-1}\right) \tag{4.3}$$

The value c will become the threshold value to determine whether a data point is associated with an event.

Next, pick an integer value, n, which will be the range that is examined to determine if a data point is associated with an event. It is recommended to start with an integer n around one-tenth of N. The algorithm assumes that there is a section of the dataset of n values in which no event occurs.

Based on the chosen n determine F_j for every data point in the set up to $N - n$:

$$F_j = \begin{cases} A_j & for \quad |d_j - e_j| \leq \beta c \\ NAN & for \quad |d_j - e_j| > \beta c \end{cases}\Bigg|_{j=1}^{j=N-n} \tag{4.4}$$

in which β is the noise amplification factor initially taken as 1.0 and NAN means "not a number" and is used for exclusion purposes. The values d_j and e_j are the maximum and minimum recorded values between A_j and A_{j+n-1} respectively.

Eq. (4.4) states that if the absolute value of the difference between the maximum (d_j) and minimum (e_j) recorded values over n data points from data point j is less than or equal to the allowed variation βc, then the data point in question is not part of an event and can be used in the calculation of the null value. If the opposite is true then the data point is excluded from the null wavelength calculation.

Finally, plot the modified dataset **F** over the original dataset **A** to examine the values that have been selected to determine the null. If too few data points have been selected, reduce n and repeat. If some of the values associated with an event are selected, increase n and repeat. If no data points are selected, or decreasing n does not significantly change the number of selected data points, increase the noise amplification factor β. Figure 4.2 shows the schematic procedure for the development of the automated null wavelength calculator. Eventually (4.4) will be able to select data values that are not associated with an event. Figure 4.3 shows three example plots showing the selected values (light gray) of the dataset (dark gray) for the successful implementation of the automated null wavelength selection.

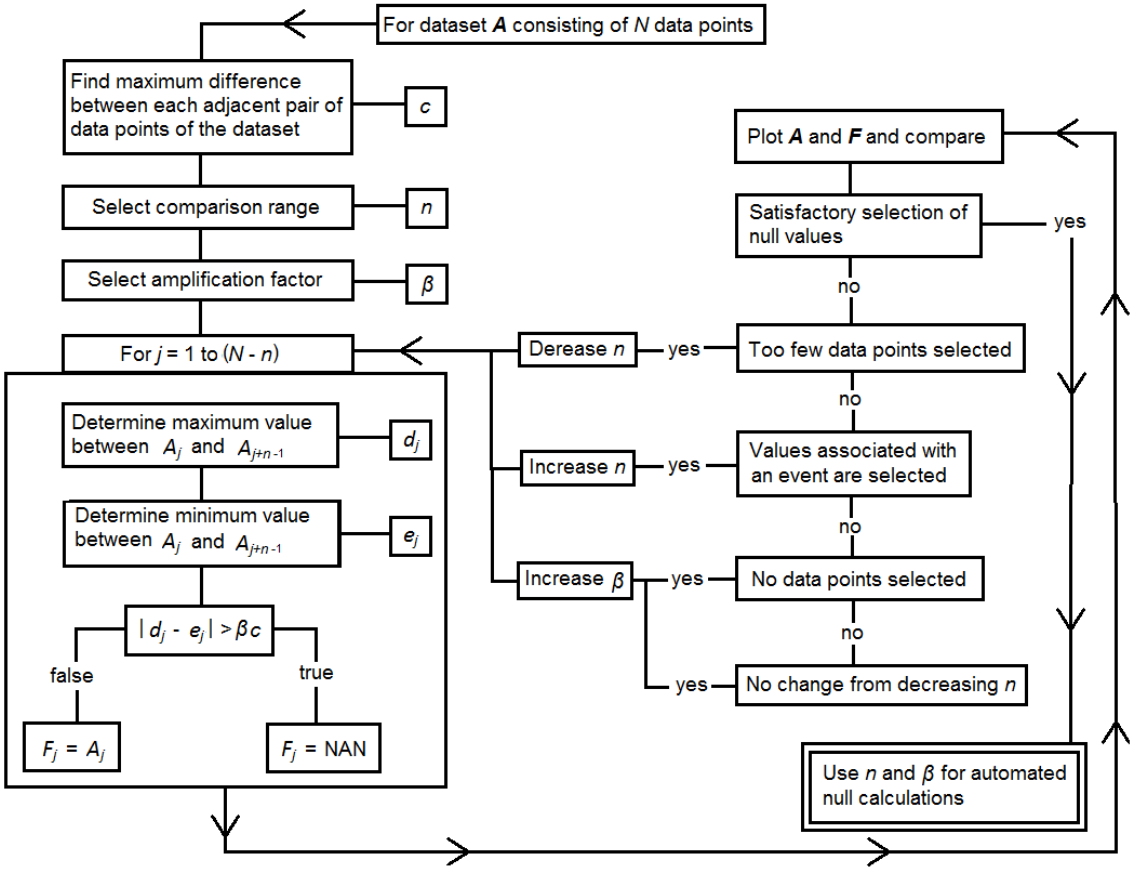

Figure 4.2. Schematic procedure for the development of the null wavelength calculator.

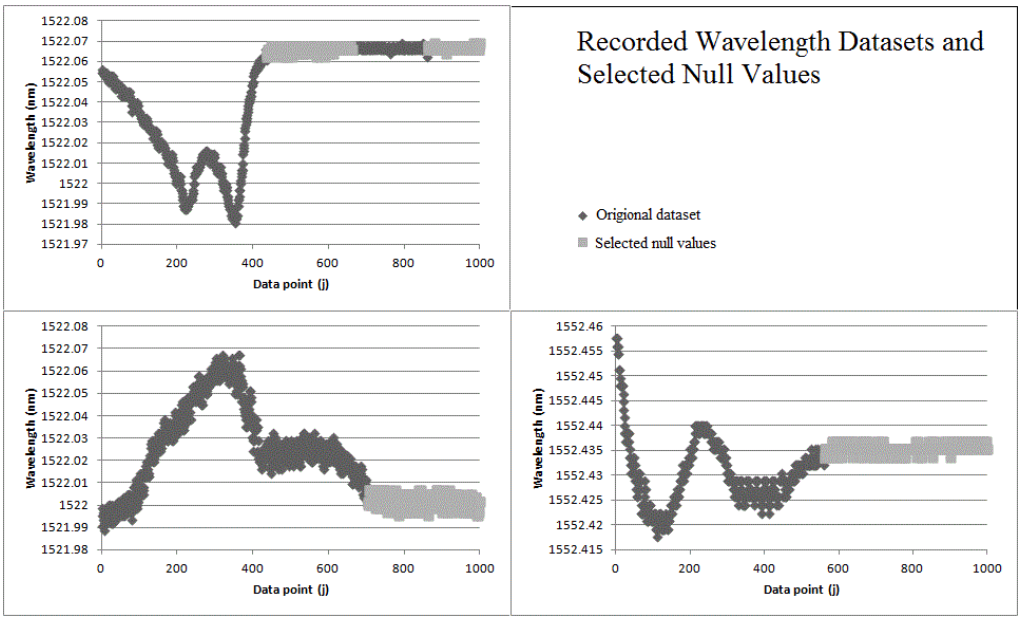

Figure 4.3. Three graphical examples of the selected data points (light gray) from the original datasets (dark gray) for calculating the null wavelengths.

4.2.3 FBG System Analysis

Before any performance or behavior analysis can be performed, the data obtained from the FBG system must be validated. This validation is obtained through an anomaly assessment, simple error analysis, and monitoring for FBG debonding.

4.2.3.1 Anomaly Assessment

The first stage in the FBG system analysis is to check all of the anomaly datasets that exist. At this point, the need to establish the proper data management and project database cannot be overstated. Over time, the number of data files will become incredibly large and can easily be in the tens of thousands for a single year. The ability to easily and efficiently navigate through the database is essential for the anomaly assessment as well as other aspects of the analysis.

The first anomaly check is for datasets that contain sensor data where the null wavelength was not established. This can be easily done through the null wavelength file. If a large number of these files exist, than the null wavelength calculator needs to be adjusted (see 4.2.2.1). Some of the other possible reasons are:

1. No null value exists for the dataset, i.e. the entire dataset is a dynamic event. If this is the case, a null wavelength can be established by interpolating between the adjacent files.
2. The data is unusually noisy and requires an increase in the noise amplification factor of the NWC to calculate the null wavelength.
3. There are not enough data points in the set for the null wavelength calculator. This can occur when a dataset is split due to a break in time. Usually this dataset can be discarded, but if there is a good reason to keep it then either of the previous solutions can be used to establish the null.

The second anomaly check is for datasets that contain sensor data where the null wavelength error is abnormally high. This occurs if the structure is loaded during the recording of the dataset and that load is sustained at a relatively constant value for a long enough period of time that the range window of the calculator does not detect any variation. For bridges, this loading could occur from stationary traffic. Consequently, the values associated with the sustained loading will be reported as null values causing a significant rise in the standard deviation. If this occurs, than a quick inspection of the local strain data associated with the high error will reveal if any corrections are necessary.

4.2.3.2 Error Analysis

The error analysis is performed by first comparing the standard deviations of the null wavelength calculations for each sensor against the precision of the sensors themselves. The ability to compare the standard deviations and precisions comes from the fact that: (1) the precision, or measurement error, of any measuring device is equal to the standard deviation of the Gaussian distribution that arises if the same measurement is repeated a large number of times; and (2) the error of an average calculated from N values with the same error will be equal to that original error divided by the square root of N.

Although the error of the recorded wavelengths is not known due to the inability to control the environment in which the sensors exist, it is reasonable to assume that the increase in error will to some degree be negated by the reduction associated with the average calculation of the null wavelength. Therefore, the standard deviation of the null wavelength calculation should be in the same order of magnitude as the precision of the sensors. Checking this provides a first-order assessment on whether or not the sensors and/or null wavelength calculator are working properly.

A second-order verification can also be performed by monitoring the behavior of the null wavelength errors over time. Fluctuations in these errors are bound to exist, but a continual increase or permanent jump are clear indicators that something is wrong with the system.

4.2.3.3 FBG Debonding

The final check in the FBG analysis procedure is for the localized debonding of the FBG sensors from either the thermosetting polymer if the sensors are imbedded in the FRP laminates, or from the adhesive used for external applications. If this occurs, then the ability to transfer the strain from the laminates to the sensors is lost. Consequently, the calculated local strain values for the sensors that have debonded will be greatly reduced. Monitoring for this failure is simply achieved by examining the local maximum and minimum files. The observation of a continuous and permanent reduction in the local maxima is a good indicator that the sensor has debonded.

Between the assessment of the anomalies present in the datasets, the error analyses, and the monitoring for possible FBG debonding, the integrity of the FBG sensors is justified. The following FRP limit analysis can then be deemed as an accurate assessment. If at any time the verification cannot be established or an anomaly cannot be classified, then an immediate investigation should commence.

4.2.4 FRP Limit Analysis

As is stated in Chapter 3, the primary limit states of concern for the typical application of FRP laminates applied to concrete are peel or delamination, composite buckling, adhesive failure, and axial tension rupture. The following procedures address how to analyze and detect each of these limit states.

4.2.4.1 Delamination

Experimental testing has produced the observation that the strain readings of FBG sensors, which are attached to portions of a FRP laminate that is debonded from the concrete, are more sensitive and produce larger maximum values than their counterparts located on bonded sections of the FRP laminate [12]. Therefore, the first method to monitor for delamination is to monitor the local maximum and minimum files for a continual increase in the ultimate values.

The second method for monitoring for delamination is to set up control sensors. This method is only applicable to two cases of SHM applications. The first case is when the sensors are applied to the surface of the FRP laminates after they have been installed, and there exists cracks in the concrete that extend through the portion of the concrete that the laminate is applied to. The second case is when a section of the concrete is prepared in a manner that the

laminate cannot bond to it. This case works when the sensors are prepackaged. One of the benefits of establishing control sensors, in addition to the ease of monitoring for peel, is that the heightened sensitivity allows for the monitoring of a wider range of loading conditions (see Chapter 5). Nonetheless, if control sensors exist then peel can be easily monitored by comparing the local strains of the adjacent sensors to the control sensor. If the adjacent sensors begin to record values similar to the control sensors then it can be assumed the peel has reached that sensor.

4.2.4.2 Composite Buckling

For composite buckling to occur, the laminate must be experiencing compressive strains and delamination must exist. If delamination does not exist, than the laminate is restrained from this limit state. If the conditions do exist for the possibility of buckling, then the method of monitoring depends upon the thru-thickness location of the sensors. Figure 4.4 shows a three-step diagram of a FRP laminate subjected to an increasing compressive load and the stress (and therefore strain) distribution. Stage 1 shows the laminate before the onset of buckling with a uniform compressive stress distribution through the thickness. As the laminate begins to buckle (stage 2), the compressive stresses at A will begin to reverse, while the stresses at B will continue to become more compressive. If the load continues to increase, the stresses at A will become tensile while the stresses at B will become even more compressive as seen in stage 3.

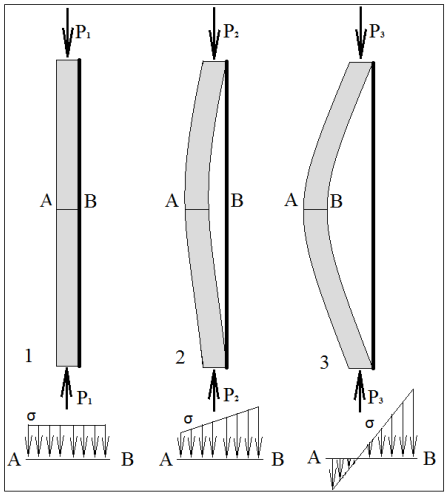

Figure 4.4. Diagrams and stress distributions across centerline AB of a FRP laminate before buckling (1), during mild buckling (2), and during severe buckling (3).

Regardless of the sensor's location, buckling is monitored by first examining the local minimums file to determine the datasets that experience significant compressive strains. Once the datasets are determined, the local strain file is examined. If the sensors are located on the surface, then the file is examined for a spike or double wall; if the load is sustained, in the tensile direction. If the sensors are applied to the inside face of the laminates, then the file is examined for a spike in the compressive direction. If the sensors are imbedded in the center of the laminate, then the reaction will be similar to the surface mounted condition but less pronounced. It is important to note again that buckling will only occur after a significant portion of the laminate has delaminated, or an extremely large loading event occurs. Either way the sensor data will be thoroughly examined.

4.2.4.3 Adhesive Failure

If a FRP laminate fails due to an adhesive failure, there will be an abrupt and significant change to all of the data associated with the sensors installed on that laminate. The fact that the data is being monitored is enough to ensure that the onset of this limit state will be noticed. Therefore, there are no specific procedures required to monitor for adhesive failure.

4.2.4.4 Axial Tension Rupture

Axial tension rupture is by far the most challenging limit state to accurately monitor. The primary reason for this is that the "actual" strains are not known. Obtaining a more accurate representation of the strains requires the compensation of temperature effects and a high level of care taken in the installation of the sensors. This will result in an increase in the cost of the system, which needs to be minimized until the widespread application of SHM systems is generally accepted. Therefore, the following method is developed through the use of the local and "fictitious" global strains coupled with a healthy dose "fuzzy" logic and conservative thresholds.

First, obtain the ultimate tensile strain of the FRP laminate that is given by the manufacturer. Multiply the ultimate strain by 0.50 and 0.75 and label these values as threshold one, T1, and threshold two, T2, respectively. The monitoring for axial tension rupture consists of comparing the absolute tensile strain, ε_{abs}, to the threshold values.

There are three methods to determine ε_{abs} (4.2.4.4.1-3). Each method increases in accuracy but at the cost of an increase in labor time. All systems will begin using Method 1 to obtain ε_{abs} until T1 is exceeded, at which point Method 2 will be used to determine ε_{abs}. Once ε_{abs} obtained by Method 2 exceeds T1, Method 3 will be used. After Method 3 is being used, ε_{abs} will be compared with T2. If T2 is ever exceeded a warning needs to be sent to the owner indicating that the FRP laminates are approaching their maximum capacity.

4.2.4.4.1 *Absolute Strain - Method 1*

Take the maximum recorded global tensile strain, ε_{GM}, and add it to the maximum recorded local tensile strain, ε_{LM}, to obtain the absolute tensile strain ε_{abs}.

4.2.4.4.2 *Absolute Strain - Method 2*

Determine a rough estimate in the change in temperature between the initial installation date and the date of the maximum global strain. Use this value in (3.2) to obtain a value for $\frac{\Delta\lambda}{\lambda_B}$ by setting the strain equal to zero, i.e.:

$$\frac{\lambda-\lambda_B}{\lambda_B} = (\alpha + \xi)\Delta T \tag{4.5}$$

Then apply this result of (4.5) to (4.1) in order to acquire an equivalent temperature strain, ε_T. Subtract ε_T from the sum of ε_{GM} and ε_{LM} to obtain ε_{abs}.

4.2.4.4.3 *Absolute Strain - Method 3*

Obtain temperature data and following the same procedure in Method 2, calculate the equivalent temperature strain for every dataset, ε_{Ti}. Save these strain values in a new file in the global folder.

Add the global strain of each dataset, ε_{GMi}, to its maximum local strain, ε_{LMi}, and subtract ε_{Ti} to obtain the dataset's absolute value ε_{absi}. Save these strains in a new file in the global folder. Then ε_{abs} is taken as the maximum of all the ε_{absi}.

The reasoning behind the development of these different methods is that there is no justification or advantage in performing a thorough assessment of the tension rupture limit state when the recorded data, in its entirety, is nowhere near the required values. As these values begin to increase, a more thorough investigation is warranted.

4.3 Behavioral Analysis

All of the procedures in section 4.2 are independent of the structure. The behavioral analysis though does not fall into this category. Each structure is unique and will behave in a unique way. Therefore, no general behavioral procedures are presented in this work. It is worth noting though that in performing the post-processing, FBG, and FRP analyses, the behavior of the system to some degree will undoubtedly reveal itself. Furthermore, the establishment of the local and global strains allows the ST and LT trends to be efficiently and independently analyzed.

4.4 Procedure Summary

The following summarizes the procedures developed in section 4.2.

1. Data Management
    a. Establish database file tree. (4.2.1)
    b. Separate original data to establish datasets with no temperature variation (if necessary). (4.2.1)
    c. Establish timestamp. (4.2.1)
    d. Remove unnecessary information and rearrange the remaining data to a more intuitive order. (4.2.1)
2. Post-Processing
    a. Develop null wavelength calculator. (4.2.2.1)
    b. Calculate null wavelengths and their standard deviations. (4.2.3)
    c. Calculate local strains. (4.2.3)
    d. Determine maximum and minimum local strains. (4.2.3)
    e. Calculate global strains. (4.2.3)
3. FBG System Analysis
    a. Determine and correct anomaly datasets. (4.2.3.1)
    b. Check null wavelength errors for large increases or sustained jumps. (4.2.3.2)
    c. Compare null wavelength errors to sensor precision. (4.2.3.2)
    d. Check for FBG debonding. (4.2.3.3)
4. FRP Limit Analysis
    a. Check for delamination. (4.2.4.1)
    b. Check for composite buckling (if applicable). (4.2.4.2)
    c. Check for adhesive failure. (4.2.4.3)
    d. Check for the onset of axial tension rupture. (4.2.4.4)

These procedures provide the ability to efficiently monitor FBG instrumented FRP laminates applied to concrete structures for the possible failures of the sensor system and/or FRP laminates, therefore providing an adaptable first-order damage detection system. Furthermore, the separation of the ST and LT strains creates the ability to independently asses the ST and LT behaviors of the structure.

CHAPTER 5. CASE STUDY

5.1 Project Description and Background

The Salt Lake Boulevard Bridge (SLBB) is a three-span, continuous, prestressed concrete girder bridge, spanning a total length of 150 ft. Originally built in 1968, and then widened in 1988, the SLBB is now 100 ft in width and supports six lanes of traffic and a median. The primary structural system consists of AASHTO Type-II beams and two sets of pier capped concrete piles for mid-span supports (see Figure 5.1).

Figure 5.1. Downstream elevation of the Salt Lake Boulevard Bridge [32]**.**

5.1.1 Deficiency Identification

The calculations of the load ratings for the SLBB in 2001 demonstrated that the bridge's shear capacity on the original girders needed to be increased. This was then confirmed by the observation of hairline diagonal shear cracks in several girders (see Figure 5.2b) [33]. Therefore, the City and County of Honolulu approved the strengthening of the bridge.

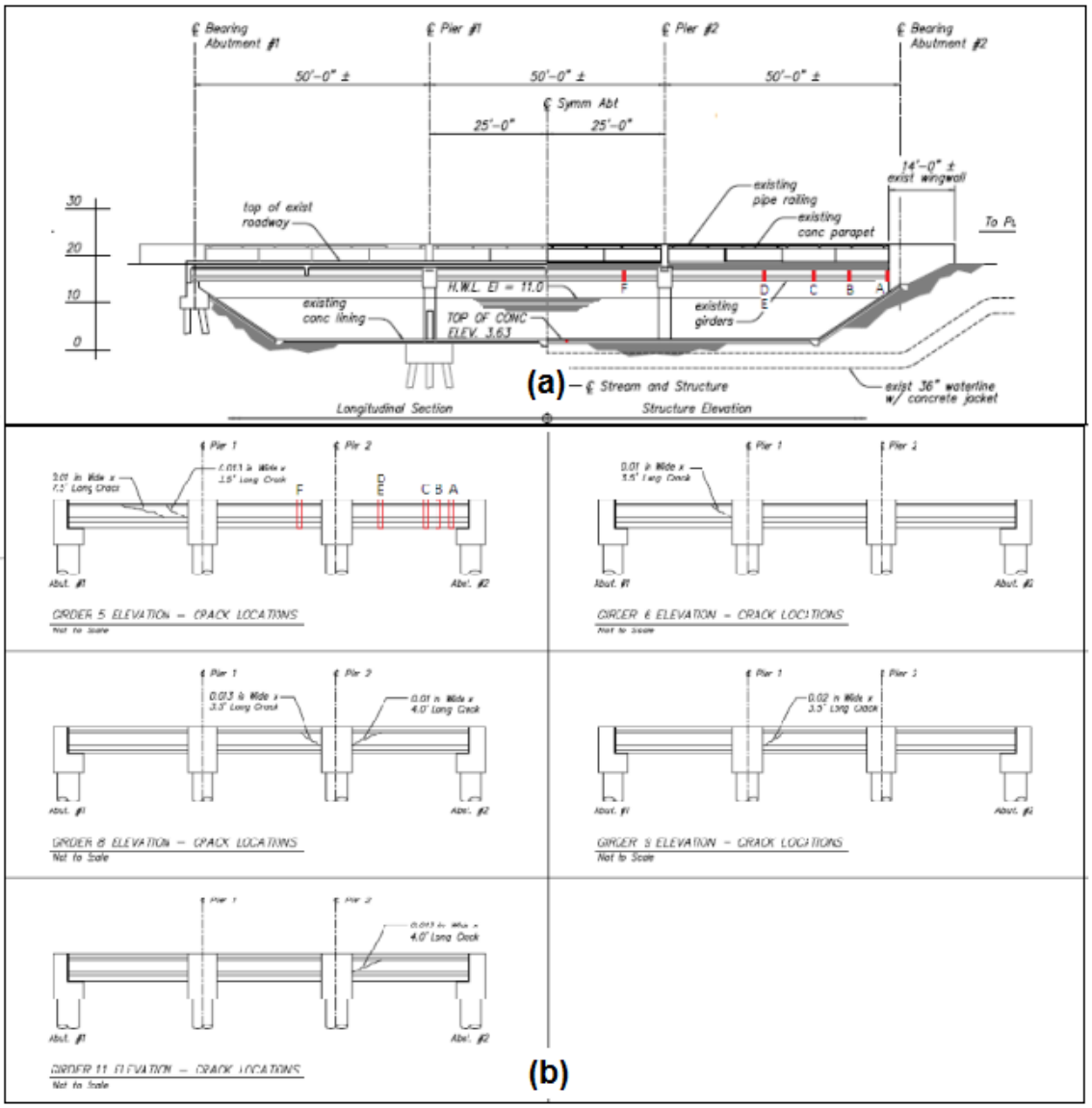

Figure 5.2. The location of the instrumented CFRP stirrups on the (a) half longitudinal section and elevation drawing, as well as in the (b) girder crack location drawings. Note that the cracks shown in (b) were prior to construction and additional cracks were observed.

5.1.2 Applied Rehabilitation

The rehabilitation of the deficient girders consisted of traditional steel rod hangers (SRHs) and wet-layup Carbon Fiber Reinforced Polymer (CFRP). The layout of the two schemes started with the application of the first 11 CFRPs, beginning 3 ft in from the centerline of the abutment and girder and extending 15 ft. After the first set of CFRPs, no strengthening was applied for a 9 ft gap across the mid span. Then an additional 6 ft of CFRPs were applied. The first set of SRHs started 1.5 ft from the second set of CFRPs and consisted of 9 SRHs which ended 3.5 ft from the centerline of the first pier. On the adjacent side of the pier, 4 SRHs were placed over a span of 4.5 ft which started 3.5 ft from the pier's centerline, followed with a 1.5 ft gap and then an additional 6 CFRPs. Finally, an 8 ft gap of no strengthening brought the layout to the centerline of the bridge, and the scheme was symmetrically repeated. Each set of both the CFRPs and SHRs were placed 18 inches apart on center. Figure 5.3 shows the schematic for the CFRP and SHR distribution over a typical girder.

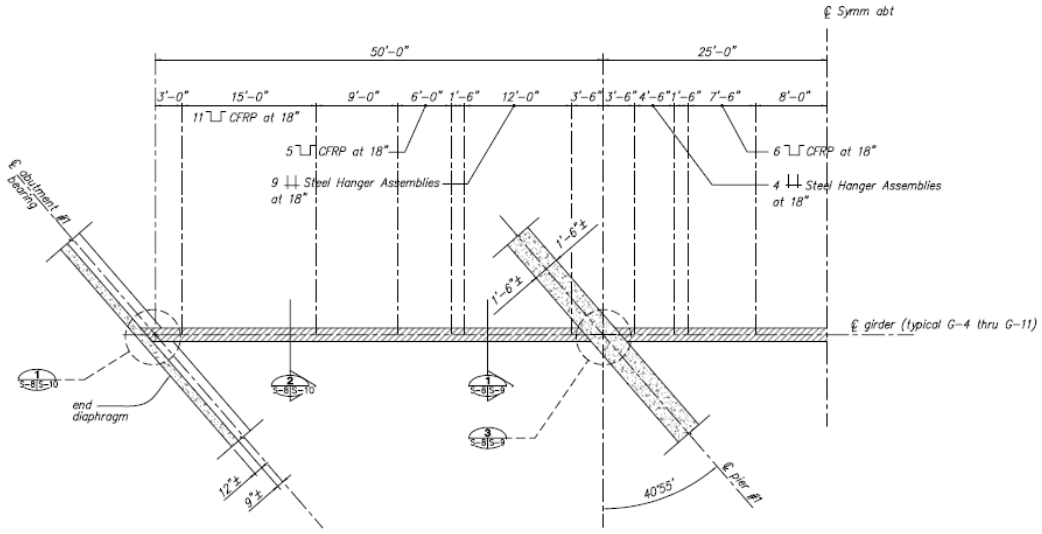

Figure 5.3. Schematic of the CFRP and SHR distribution on a typical girder.

Before the application of CFRP laminates, the webs of the girders where the CFRP's were to be applied were filled with concrete to create a smooth rectangular surface (see Figure 5.4a). The CFRPs were 12 inches in width and had a minimum design ultimate tensile strain of 0.0126. After the concrete infill cured, the CFRPs were applied, painted, and anchored with steel angles and three epoxy set anchor bolts. The final installation can be seen in Figure 5.4b. The construction finished in late 2008.

Figure 5.4. (a) Concrete infill of the AASHTO Type-II girders for the CFRP application, and (b) the completed CFRP stirrups[32]**.**

5.1.3 Sensor Instrumentation and Labeling

The sensor instrumentation of the SLBB consisted of 30 BRΛGG Photonics, Inc. FBG strain sensors combined with a MicronOptics, Inc. si425 Interrogator and a remote Internet connection. The sensors were placed on five CFRP stirrups located on girder 5 which showed the most severe cracking (see Figure 5.5 for girder location). The CFRP stirrups that were instrumented can be seen in Figure 5.2, and are labeled A through F with A being the closest to the abutment and the remainder moving successively towards the center of the bridge. The labels D and E represent the two sides of the same stirrup. The reason for the double label being that only the downstream face of stirrups A, B, C and F are instrumented, while stirrup D/E is instrumented on both the downstream face D, and the upstream face E.

Each stirrup face was instrumented with five sensors. The layout consisted of four edge sensors placed one inch in from the edge of the CFRP stirrups on the side nearest to the closest support. The fifth sensor was inset four inches from the same edge and vertically parallel to one of the edge sensors. The original plan was to have the inset sensor be vertically parallel to the uppermost edge sensor. After the installation of the first set of sensors at A, a shrinkage crack was observed at the base of the concrete infill six inches from the bottom of the girder. Therefore the inset sensor on the remaining stirrup faces was placed on this crack, in addition to the edge sensor already planned to be installed at the crack location.

The layout of each stirrup can be seen in Figure 5.6. Note that the sensors for D/E are in the same locations on their respective faces. The labeling of each sensor is done in the following format: “stirrup face letter”-”number of inches from the bottom of the girder”-”number of inches

from the nearest edge". Therefore, the sensor located on stirrup face A, 6 inches from the bottom of the girder, and 1 inch in from the edge is labeled A-6-1, and so on. This labeling format will be used for the remainder of this work when discussing a particular sensor.

5.1.4 Project Objectives

The primary objectives of this project were to:

1. Instrument the CFRP to measure its effectiveness under dynamic traffic loads.
2. Study the effect of the existing cracks in the concrete on the bond between the CFRP and concrete.
3. Determine if long-term dynamic loading will cause delamination.
4. Determine the extent and effect it has on the effectiveness of the CFRP system, if delamination occurs.

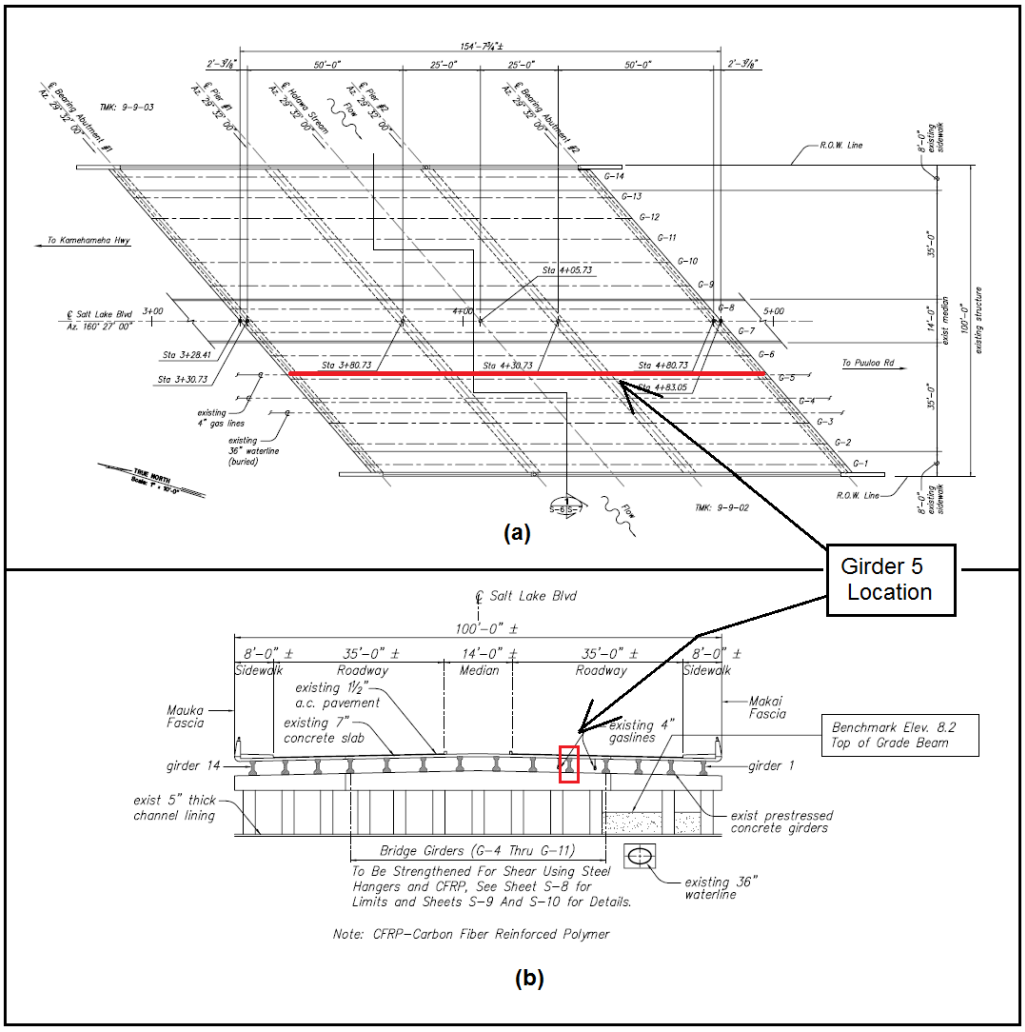

Figure 5.5. The location of the girder instrumented with FBG sensors in (a) the plan view and (b) the cross section of the construction drawings.

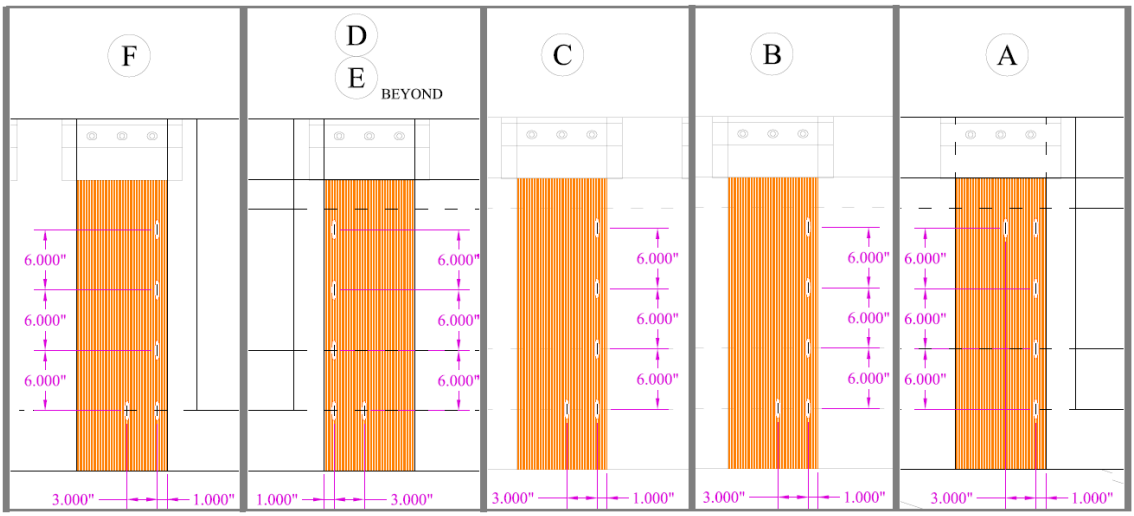

Figure 5.6. The FBG sensor layouts for each of the stirrups instrumented.

5.2 Data Collection

The SHM system applied to the SLBB became operational in the beginning of October 2009. At this time, data began to be remotely collected for the sensors at A, B, C, and F. The sensors at D and E did not come online until September 2010. The data presented in this work was recorded between October 2nd, 2009 and July 2nd, 2011. Due to the poor reliability of the router supplied by the Internet provider, there are three significant time gaps over the course of the record. These gaps are between December 12th, 2009 to January 5th, 2010, July 20th, 2010 to September 30th, 2010, and October 30th, 2010 to March 25th, 2011.

The majority of the remotely recorded data was recorded in four second intervals at 250Hz, with one interval transmitted per hour. The data was transmitted from the site to a server located at the University of Hawai‘i at Mānoa. The four seconds per hour limit was the result of the allowable internet speed and the size of the interrogator’s buffer. An attempt was made to increase the duration in September 2010, but this was abandoned after observing a significant increase in the number of files where the buffer was rewritten before the dataset finished transmitting.

Data was recorded during a site visit on September 30th, 2010. In addition to restarting the router, the reason for the visit was to couple the observed traffic loading with the recorded data response to establish a set of control characteristics. During this visit, data was successfully recorded for an isolated large vehicle crossing the bridge in all six lanes independently.

5.2.1 Data Format

Two distinct data formats exist for this project. The differences in the data format depend upon whether the data was recorded remotely or on site. The reason for this was that the data recorded on site was obtained through the use of the software provided with the interrogator, whereas the remotely recorded data was transmitted in its original binary format and then converted to a delimited file through the provided algorithms in the interrogator's manual. The software removed some of the information associated with the binary output of the interrogator. For this project, the relevance was that for remotely recorded files, the sensor data began on column 13, whereas for the files recorded onsite, the sensor data began on column 6. For both types of original files, the time was recorded in column 1. Although no other data besides the time and sensor values were kept, it is important to note that four of the columns (which were removed during the processing) listed the number of sensors on each channel. These values were used in determining the sensor column format of each recorded dataset.

Finally, a column's association to a particular sensor depended upon which channels were operational when the data was recorded. For the SLBB project, sensors located at A and F (see Figures 5.2 and 5.6) were connected to channel 1, D and E to channel 2, and B and C to channel 3. Channel 4 was not used. The sensors were recorded in ascending order from channel 1 to channel 3. If a channel was non-operational when the data set was recorded, then any following channels were moved up in column location such that there were no column gaps in the recorded data set. The sensor column orientations for each channel are listed in Table 5.1.

Table 5.1. Sensor column orientations for the original datasets.

Channel	Columns 1 - 5				
1	F-24-1	A-6-1	F-18-1	A-12-1	F-12-1
2	D-6-4	E-24-1	D-6-1	E-18-1	D-12-1
3	B-24-1	C-6-4	B-18-1	C-6-1	B-12-1
	Columns 6 - 10				
1	A-18-1	F-6-1	A-24-1	F-6-4	A-24-4
2	E-12-1	D-18-1	E-6-1	D-24-1	E-6-4
3	C-12-1	B-6-1	C-18-1	B-6-4	C-24-1

The format used for this project can be seen in Tables 5.2 and 5.3. It is important to note that the time column was either the timestamp if the data was a global file, or localized seconds for a local file.

Table 5.2. Column format for reordered datasets.

		Stirrup					
	Time	A	B	C	D	E	F
Column #'s	1	2--6	7--11	12--16	17--21	22--26	27--31

Table 5.3. Sensor column order for reordered datasets.

Stirrup	**Column ordering**				
A	A-6-1	A-12-1	A-18-1	A-24-1	A-24-4
B	B-6-4	B-6-1	B-12-1	B-18-1	B-24-1
C	C-6-4	C-6-1	C-12-1	C-18-1	C-24-1
D	D-6-4	D-6-1	D-12-1	D-18-1	D-42-1
E	E-6-4	E-6-1	E-12-1	E-18-1	E-24-1
F	F-6-4	F-6-1	F-12-1	F-18-1	F-24-1

5.3 Procedures

The following procedures were developed following the layout established in Chapter 4. The data management and post-processing were achieved through the execution of a MATLAB script developed for this project. Appendix A provides the details of the functions and operations of the MATLAB script. In addition, the duration of all the data files was on the order of seconds; therefore, there was no need to separate the files to remove possible temperature variations within the original datasets. Finally, since the data management and post-processing happen in the same MATLAB script, their procedural descriptions were combined.

5.3.1 Data Management and Post-Processing Procedure

First, the database's file tree was established. The data was then copied from the server to the input folder with the original files remaining on the server as backups. After the establishment of the database, the null wavelength calculator was established through the use of three datasets that exhibited prominent wavelength variations. The range, n, was established as 200 data points, and the amplification factor, β, was determined to be 1.0 (see 4.2.2.1).

After manually establishing the null wavelength calculator, every file in the input folder went through the following automated procedural steps:

1. The active sensors were determined and the time and sensor columns were rearranged into the format listed in Tables 5.2 and 5.3
2. The time steps were analyzed against the frequency of 10Hz to determine if there were any breaks in time. If a break in time was found then one of two possibilities occurred.
    a. If the break in time occurred at the beginning or the end of the file where there were less than 300 data points for one of the portions, that portion was removed.
    b. If the break in time occurred such that both portions had more than 300 data points, then the dataset was split and each section individually processed.
3. The timestamp was established.
4. The local folder was created. The project name used was “SLBB”
5. The original file was saved in the new timestamped folder.
6. The local time was calculated.
7. The reformatted wavelength format was established.
8. The null wavelengths and their standard deviations were calculated.
9. The local strains were calculated using the null wavelength, reformatted wavelength format, and (4.1).
10. The maximum and minimum local strains were determined.
11. The global strains for the dataset were calculated.
12. The reformatted wavelengths and local strains were saved in the timestamped folder with the local time as the first column.
13. The global files were opened and the chronological location of the new values was determined.
14. The new global variables were written into their respective files in the position determined in step 13, and the updated files were saved.

If the original file was split in step 2, than steps 3 through 14 were repeated for the second portion.

5.3.2 FBG System Analysis Procedure

The first stage of the FBG system analysis was to determine and correct the anomaly datasets associated with no null wavelength being calculated. This was done through the following automated steps:

1. The null wavelength file was opened and the row and column for every nonexistent value (minus the sensors at D and E before they were operational) was determined.
2. The timestamp for each row that contained a nonexistent value was determined.

3. For each timestamp:
    a. The local wavelength file with the same timestamp was opened.
    b. The null wavelength for the appropriate columns was recalculated with the amplification factor, β, increased by 0.2.
    c. If the null wavelength was still not obtained, β was increased by an additional 0.2.
    d. This recalculation process with the continual increase in the β was repeated until a null value was determined.
    e. The standard deviation was calculated.
4. The timestamp, column number, final amplification factor, null wavelength, and standard deviation for every originally nonexistent value were saved in a null update file.
5. The amplification factors were checked for excessively large values.
6. The null wavelength and standard deviation files were updated with the new values.
7. The appropriate local strains, maximums, minimums, and global strains were calculated and their files updated.

The final anomaly check was for abnormally high error values. This was achieved by plotting the null wavelength errors, and locating the values that stood out from the pack through a visual inspection. If any such values were observed then the timestamps of the values were determined and their respective local strain file was examined.

The second stage of the FBG system analysis was to compare the null wavelength errors to the original sensor precision. This was done by manually examining plots of the null wavelength errors.

The third and final stage was to check for FBG debonding. This was done by manually examining the plots of the local maximum and minimum files. The plots were examined for a sustained drop in the recorded values.

5.3.3 FRP Limit Analysis Procedure

Since at least one sensor on each instrumented CFRP stirrup face was installed over the preexisting shrinkage crack that developed at the bottom interface of the existing girder and the concrete infill, delamination was monitored by both methods described in section 4.2.4.1. Maxima plots were created which plot the current local maximum and minimum envelopes for each sensor at the time each dataset was recorded. These envelopes were examined for large increases over time, and the plots of the sensors not associated with the shrinkage crack were compared against the sensors placed over the shrinkage crack.

Composite buckling was checked for the sensors positioned over the shrinkage crack. This was done by examining the local strain file associated with the largest negative strains, as determined from the local minimum plots.

The possible onset of adhesive failure was inherently checked by all of the previous examinations.

The monitoring for the onset of axial tension rupture was performed exactly as described in section 4.2.4.4. The threshold values were obtained from the minimum ultimate tensile strain of the CFRP as specified in the design. The absolute strains were calculated for each sensor and normalized against the threshold value for comparison.

5.3.4 Behavioral Analysis Procedure

The local and global behaviors were independently analyzed. The local behavior of the SLBB was characterized through the observations of all of the sensors located six inches from the bottom and one inch from the nearest edge (i.e., sensors A-6-1 through F-6-1) for the recorded datasets corresponding to isolated large vehicles crossing the bridge that were obtained during the September 2010 site visit. In addition to the characterization, the velocities and accelerations of the vehicles were calculated if the response was well defined. The velocities were calculated by the following procedure:

1. The time for each defined peak in the data was recorded for each stirrup's 6-1 sensor.
2. The difference in time between each successive peak of each sensor pair was calculated.
3. The distance between each of the sensor pairs was divided by the calculated difference in time to obtain an average velocity of the peak.
4. If more than one peak in the data existed, then the average velocities of each peak and sensor pair were averaged.
5. If more than one velocity was calculated, then the velocities were plotted versus time where the time was the average between the two initial times.
6. A linear curve fit was then performed to obtain an approximate acceleration.

After examining the behavior of the isolated loading conditions, a dataset corresponding to multiple vehicle loads was examined to determine if it was possible to isolate each vehicle based on the control behaviors.

The global behavioral analysis was performed through the examination of every sensor's global strain plots.

5.4 Data

A total of 13,765 datasets spanning 21 months were recorded remotely. All of these datasets contain sensor recordings for the sensors located at A, B, C, and F, and the latter 7,651 containing recordings from all 30 sensors applied to the SLBB. The datasets were then processed into an additional 27,541 files creating a total of 41,309 files, 1,055,760 individual datasets, and 1,055,760,000 data points.

5.5 FBG and FRP Analysis and Results

The following analysis and results presented in this section are limited to the sensors on stirrup A. Appendices B through F provide supplemental sections for the FBG and FRP analysis and results for the sensors on stirrups B through F, respectively.

5.5.1 FBG System Analysis and Results

For stirrup A, 1,896 or 2.75% of the total sensor datasets did not have a null wavelength established from the automated post-processing. The individual sensor breakdown of these values, their respective percentages, as well as the range of increased amplification values can be seen in Table 5.4.

Table 5.4. Breakdown of the number and percentage of individual sensor datasets where a null wavelength value was not established for stirrup A, as well as the range of amplification factors required to processes the sets.

	No established null wavelength		Amplification range	
Sensor	Number of sets	%	β Min	β Max
A-6-1	1331	9.67	1.4	2.0
A-12-1	246	1.79	1.4	2.0
A-18-1	213	1.55	1.4	2.0
A-24-1	53	0.38	1.6	2.0
A-24-4	53	0.38	1.4	2.0

As can be seen from Table 5.4, the maximum amplification factor, β, required to establish a null wavelength was 2.0. This maximum amplification was deemed insufficient to warrant an investigation into the individual datasets.

The null wavelength error plots for the sensors at stirrup A are presented in Figure 5.7. From these plots it can be seen that only one abnormally high value existed from all five of the

sensors. This error value was 0.008 nm and was associated with sensor A-6-1 recorded on October 3rd, 2010 at 12:48 AM. An examination of the local strain plot revealed that a slow event occurred which caused the inclusion of several sections of data into the null wavelength calculation (see Figure 5.8). Nonetheless, because the variation of strain was so small (about 25 microstrain) over the entire file, and a wavelength error of 0.008 nm only produced a strain error of about 7 microstrain, it was deemed unnecessary to perform any corrective measures.

It can also be seen from Figure 5.7 that the null wavelength errors for sensors A-24-4, A-24-1, and A-18-1 never exceeded the recording precision of the sensors (0.002 nm). Sensor A-12-1's errors exceeded the sensors' precision only four times and by only 0.001 nm. For sensor A-6-1, the upper bound of the null wavelength error was typically 0.004 nm, though it did rise to 0.005 nm on a few occasions as well as to 0.008 nm once.

Figure 5.9 and Figure 5.10 show the plots of the local maximum and minimum strains plotted against the date they were recorded for the sensors on stirrup A. Through examining these plots it can be seen that maxima remained relatively constant for sensors A-24-4, A-24-1, A-18-1, and A-12-1. A-6-1 shows a larger variation in the recorded maxima, but this variation remains relatively constant as well. Therefore, FBG debonding has not occurred for any of the sensors on stirrup A.

Through the correction of the datasets with no null wavelength calculated from the initial post-processing and the assessment of abnormally high null wavelength values, the anomalies were corrected. Comparing the null wavelength errors against the precision of the sensors demonstrated that the null wavelength errors lie within a justifiable range. Checking for a decrease in maxima values demonstrated that the FBG sensors have not debonded. Therefore, it can be concluded that the FBG system on stirrup A was in good working order over the range of recorded data.

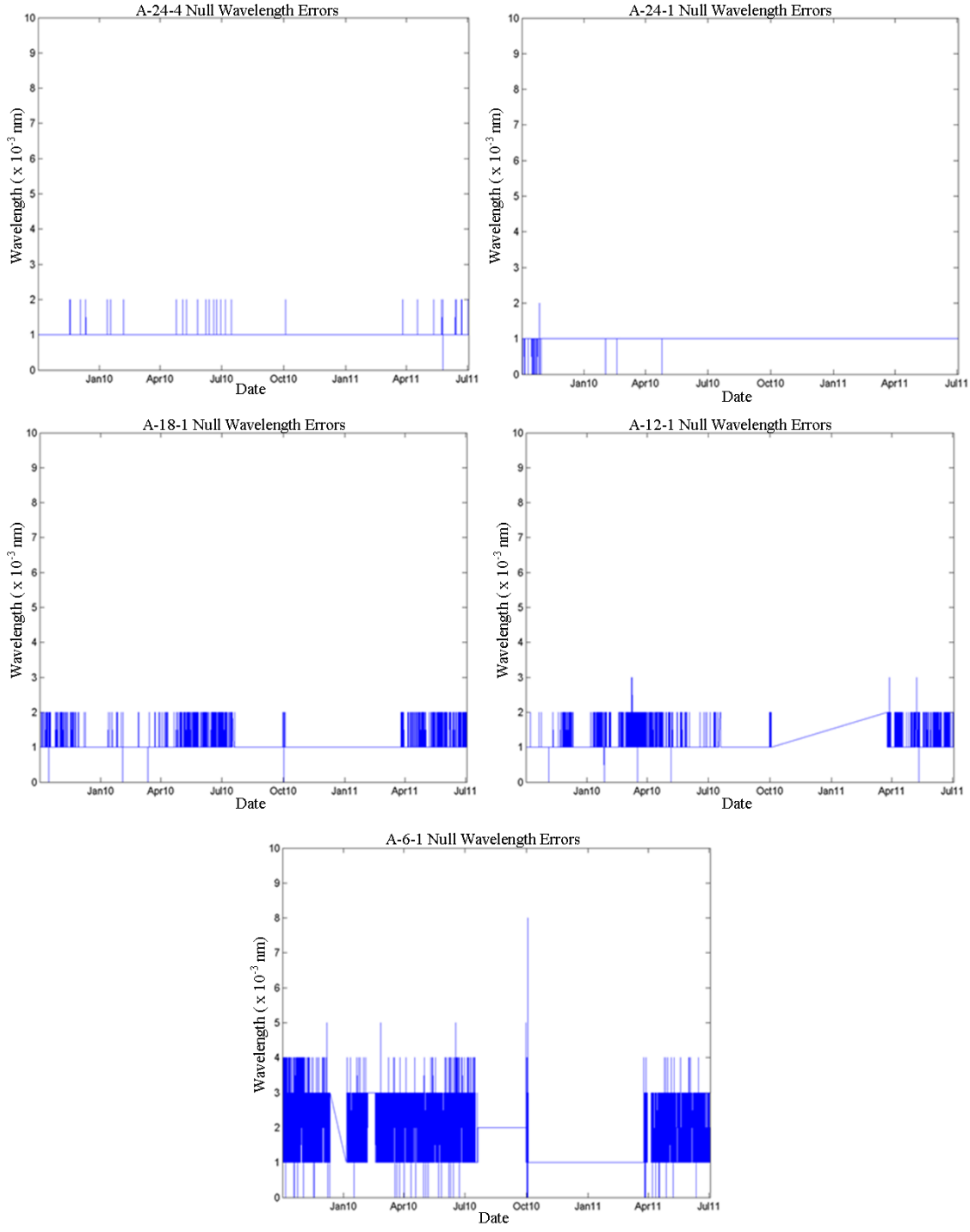

Figure 5.7. Null wavelength errors versus the dates they were recorded for sensors on stirrup A.

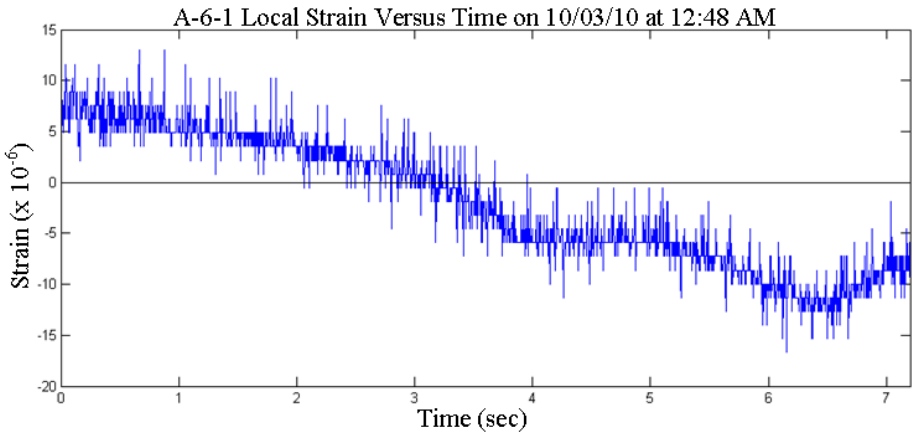

Figure 5.8. Local strain versus time for sensor A-6-1 for the file associated with the 0.008 nm null wavelength error.

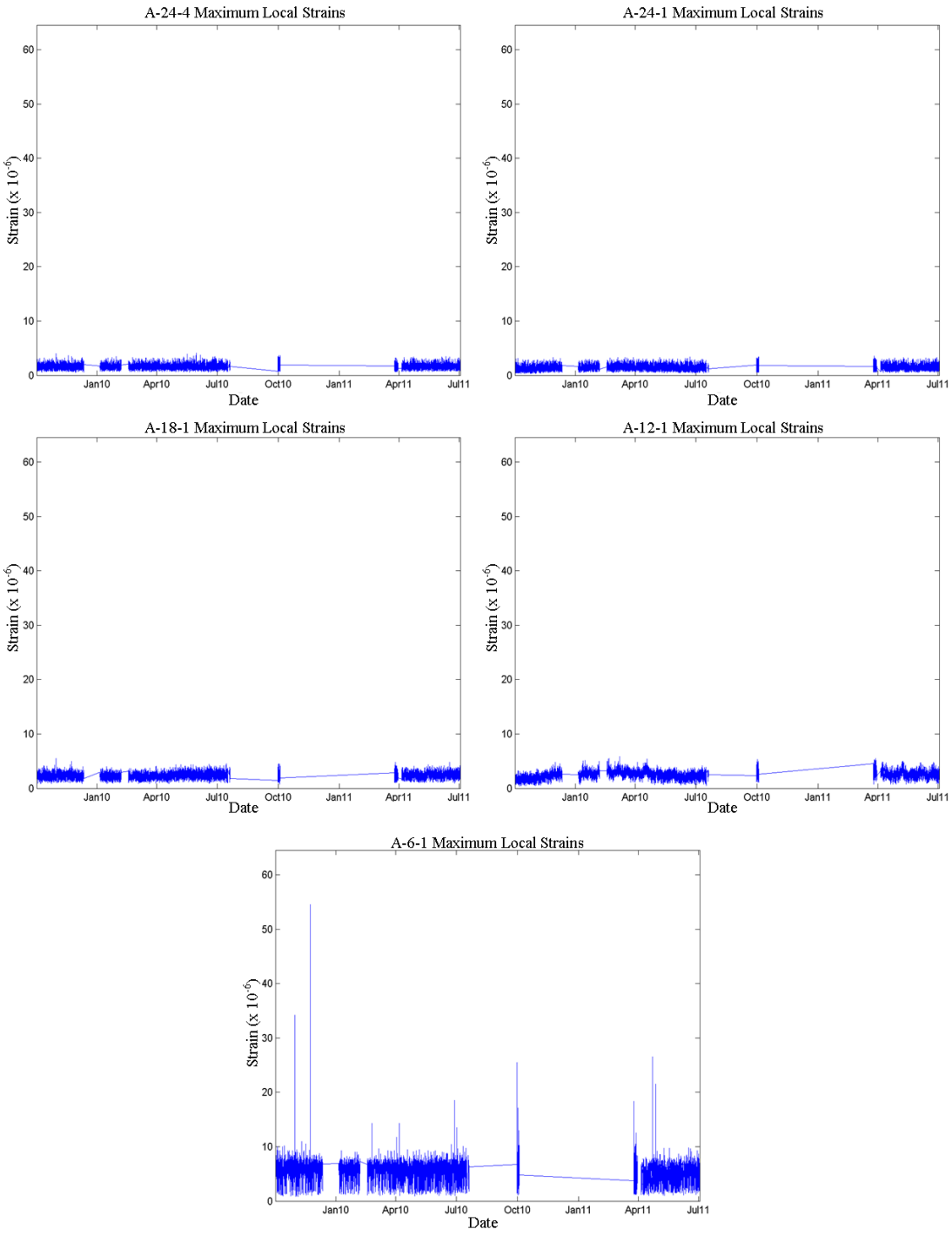

Figure 5.9. Maximum local strains versus the dates they were recorded for sensors at stirrup A.

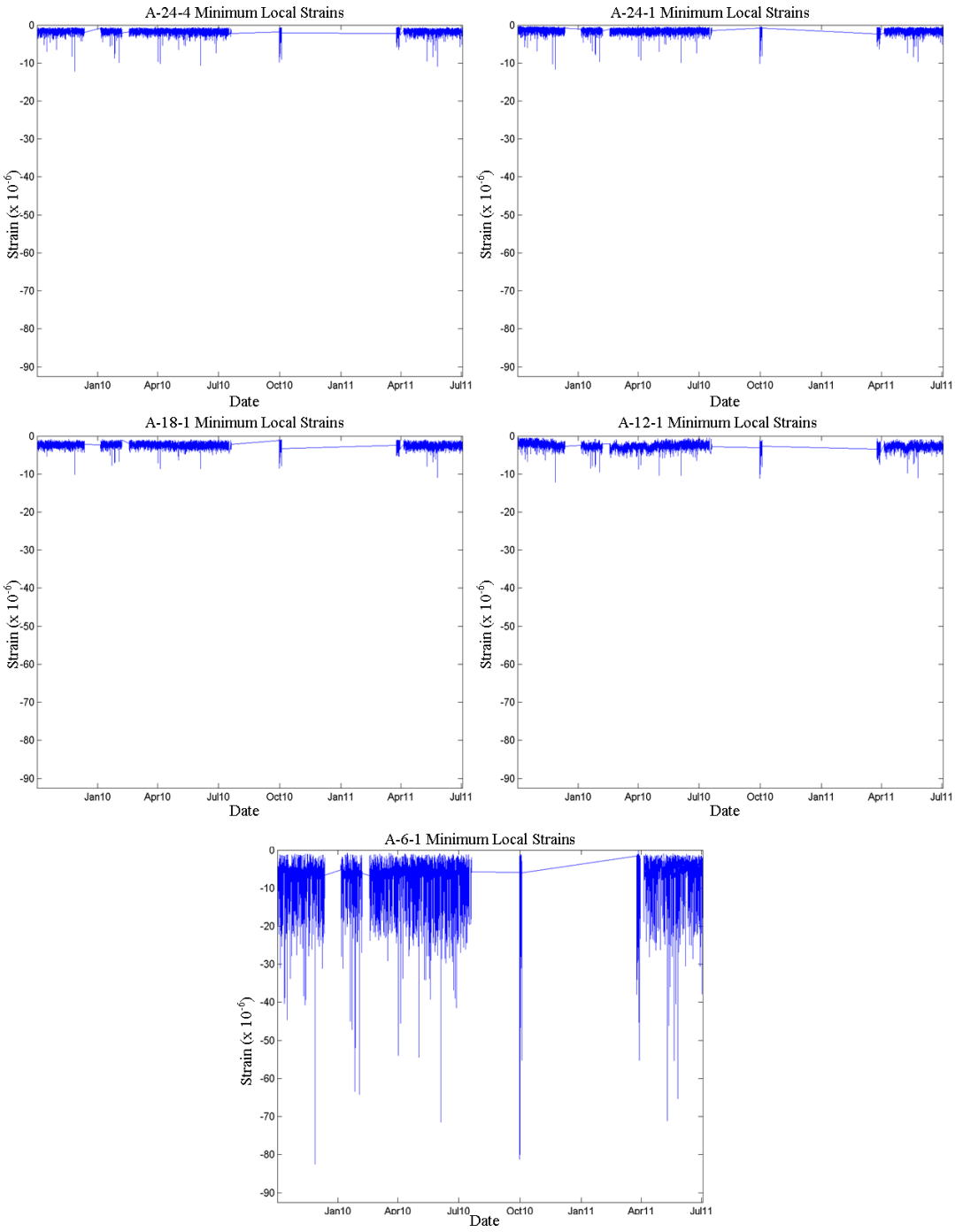

Figure 5.10. Minimum local strains versus the dates they were recorded for sensors at stirrup A.

5.5.2 FRP Limit Analysis

The envelope plots of the growth in the absolute local maximum and minimum strain values over the duration of data presented in this work for the sensors on stirrup A can be seen in Figure 5.11. Sensor A-6-1 was the sensor applied to the CFRP at the location of the shrinkage crack between the infill and bottom bulb of the girder. A quick observation of these graphs shows that by 2010 the maxima for all of the sensors minus sensor A-12-1 became constant. The absolute maximum of sensor A-12-1 did increase after the other sensors on stirrup A reached their maximums, but this increase was by only a few microstrain and can be considered as constant. Furthermore, by comparing sensors not placed over the shrinkage crack to sensor A-6-1, it can be seen that the maxima strains are only about 20% of A-6-1. Therefore, it can be concluded that debonding or peel has not occurred for stirrup A.

The absolute recorded minimum local strain for A-6-1 was -82.5 microstrain and was recorded on October 28th, 2009 (see Figure 5.10). Unfortunately, the event causing the negative strain occurred right at the end of the dataset and as such could not be checked for composite buckling. Therefore the second largest minimum file was used. This file was recorded on September 30th, 2010 at 1:20 PM and had a minimum strain value of -81.2 microstrain. It can be seen from the plot of this local strain file in Figure 5.12 that there was no indication of composite buckling as described in section 4.2.4.2. Because there was no indication of composite buckling with the second largest minimum strain record, and that no peel has occurred, it can be concluded that no composite buckling has occurred on stirrup A.

The continual activity of all the sensors on stirrup A as seen through the local maximum and minimum plots in Figures 5.9 and 5.10, respectively, confirms that adhesive failure has not occurred for stirrup A.

With the design-specified required minimum ultimate tensile strain of 0.0126, the first threshold value, T1, became 6,300 microstrain. Table 5.5 lists the maximum global strain ε_{GM}, the maximum local strain ε_{LM}, the absolute strain, ε_{abs}, obtained using method 1 (see 4.2.4.4.1), as well as the normalized percentage of the absolute strain against T1 for each sensor on stirrup A. From Table 5.5 it can be seen that the maximum absolute strain for all of the sensors on stirrup A only reaches 1.38% of T1. Therefore, the induced tensile strains on stirrup A are nowhere near the onset of tension rupture.

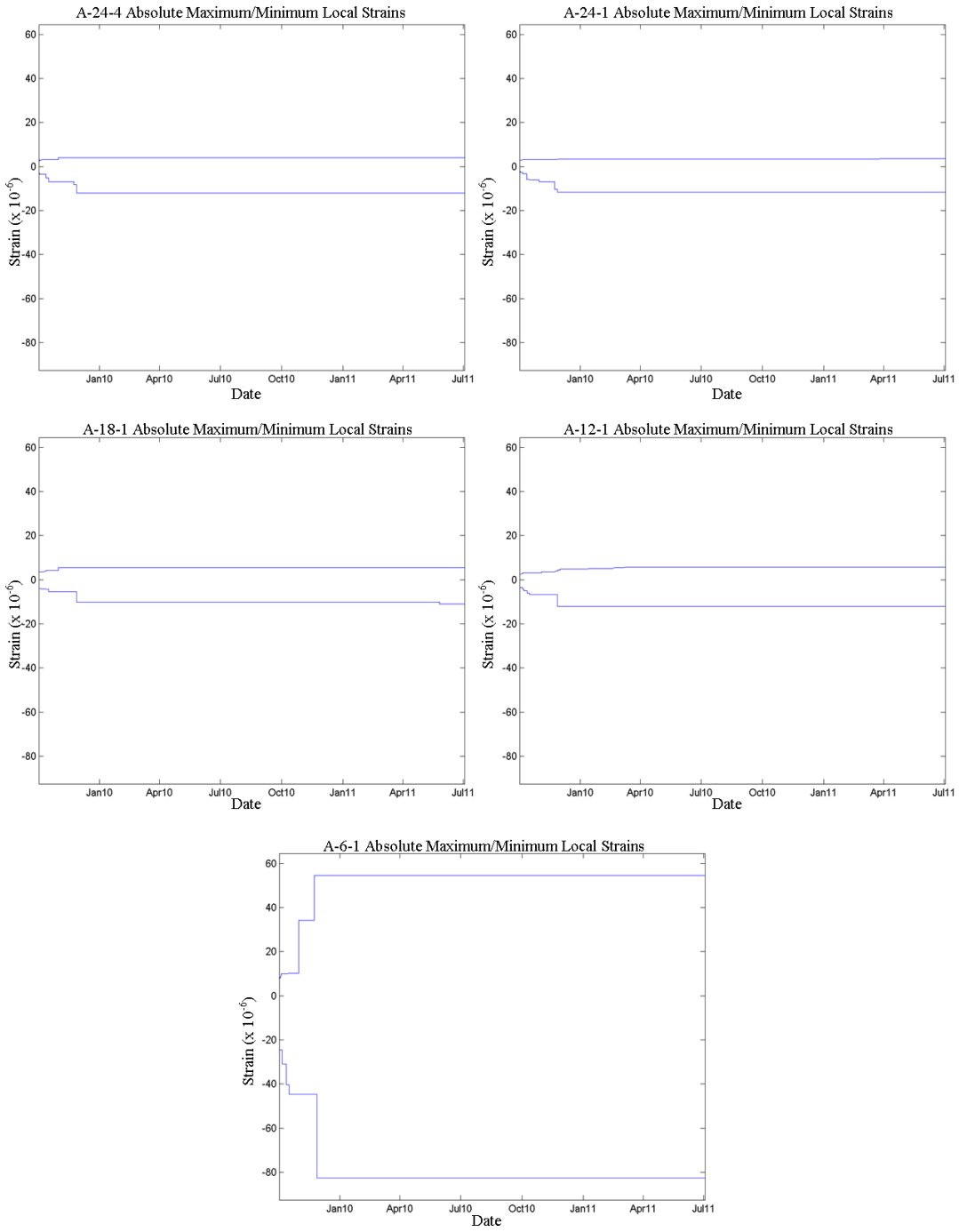

Figure 5.11. Absolute local maxima envelope versus recording date for sensors on stirrup A.

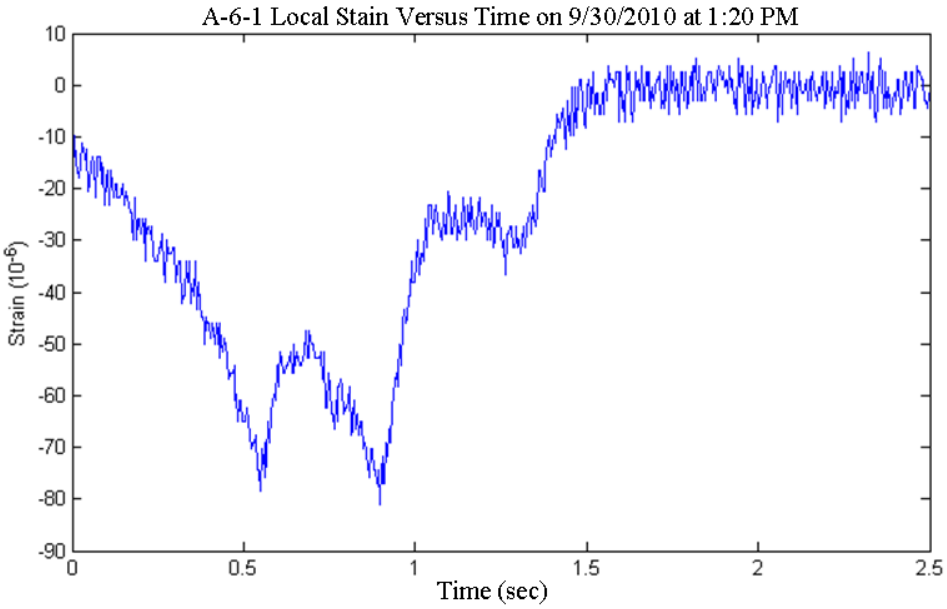

Figure 5.12. Plot of local strain versus time for sensor A-6-1 strain data recorded on September 30th, 2010 at 1:20 PM.

Table 5.5. The maximum global strains, maximum local strains, absolute strains, and the normalized percentage of the absolute strains against the threshold T1 for each sensor on stirrup A.

	T1 = 6300 x 10^{-6}			
	Maximum strains (10^{-6})			
Sensor	**Global (ε_{GM})**	**Local (ε_{LM})**	**Absolute (ε_{abs})**	**% of T1**
A-6-1	33	54	87	1.38
A-12-1	37	6	43	0.68
A-18-1	32	6	38	0.60
A-24-1	45	4	49	0.78
A-24-4	38	4	42	0.67

For the sensors on stirrup A, through both the individual assessment of each sensor as well as the comparison of the sensors not placed over the shrinkage crack against A-6-1, no debonding or peel has been observed. It has also been determined that the limit states of composite buckling and adhesive failure have not occurred. Finally, the absolute tensile strain values have not come remotely close the T1 threshold value. Therefore, it can be concluded that the CFRP stirrup A was in good working condition over the duration of the recorded data.

5.6 FBG and FRP System Analysis Summary

From section 5.5 and Appendices B through F, it can be summarized that no debonding or peel has been observed for any of the instrumented stirrups. It has also been determined for each stirrup that the limit states of composite buckling and adhesive failure have not occurred. Finally, the absolute tensile strain values, the maximum of which was observed for sensor D-6-4 at 2.38 % of the T1 threshold value, have not come close to approaching a value that requires further attention. Therefore, it can be concluded that all of the instrumented CFRP stirrups were in good working condition over the duration of the recorded data.

5.7 Behavioral Analysis and Results

The observations of the datasets associated with traffic loading in the lanes opposite the median from the instrumented girder only produced an increase in the recorded noise. No unique characteristics were observed and as such these datasets are omitted from the analysis. Therefore, the following local behavior analysis was limited to the loading of the three lanes on the same side of the median as the instrumented girder.

The direction of traffic for these lanes was the opposite of the sensor labeling (i.e., stirrup F is the first instrumented sensor to be crossed followed by stirrups D/E, C, B, and then A). The lanes were labeled left, right and middle. The left lane was the closest to the median, the right lane was the closest to the edge of the bridge, and the middle lane was in the middle. Following this designation, the sensors on stirrup E were on the left side of the girder and all of the other sensors were on the right side. Furthermore, the instrumented girder is positioned on the left side of the middle lane. Therefore, the centerline of a vehicle load would lie to the right of the girder for vehicles in the middle and right lanes, and to the left for vehicles in the left lane. The centerline to centerline distance between each of the instrumented stirrups can be seen in Table 5.6.

Table 5.6. Distances in feet between the instrumented stirrups.

Distance (ft)				
Stirrup	A	B	C	D/E
F	56.5	49	41.5	26.5
D/E	30	22.5	15	
C	15	7.5		
B	7.5			

5.7.1 Left Lane Loading Characteristics

The left lane loading characteristics were examined for the eighteen-wheel, six-axle semi seen in Figure 5.13. Figure 5.14 shows the strain versus time plots of the 6-1 sensors recorded while the semi crossed the bridge. Sensor C-6-1 was omitted from the plots because no significant response could be seen. The most distinguishing characteristics of this load case were; (1) the relatively high compressive strains of sensor E-6-1; (2) the tensile strains of sensor A-6-1; and (3) the oscillation of sensor F-6-1. Also note the three distinguished peaks seen in the response of E-6-1, D-6-1, and A-6-1. The peaks of D-6-1 and E-6-1 resembled the typical load distribution of a semi with the first peak being the smallest and the second two peaks having similar values. The peaks of A-6-1 successively decreased. Since the stirrup A was only three feet from the end of the bridge, the decrease reflected the fact that the axle loads of the semi were transferred to the roadway after crossing the stirrup.

Figure 5.13. Semi associated with the left lane vehicle loading dataset.

To calculate the velocities, the two most prominent peaks were used since the first peak could not be established for sensor F-6-1. The time that the two peaks were recorded for sensors F-6-1, D/E-6-1, and A-6-1 are listed in Table 5.7. The duration between each sensor pair for the two peaks, the average of these durations, and the calculated velocities using the distances from Table 5.6 are presented in Table 5.8.

Table 5.7. Recorded times of the two prominent peaks associated with the left lane loading.

	Time (sec)	
Sensor	**Peak 1**	**Peak 2**
F-6-1	4.92	5.79
D/E-6-1	5.46	6.18
A-6-1	5.99	6.73

Table 5.8. Time durations between stirrups and the calculated velocities for the left lane loading.

	Duration (sec)			
Stirrups	**Peak 1**	**Peak 2**	**Average**	**Velocity (mph)**
F to D/E	0.54	0.39	0.47	38.6
F to A	1.07	0.94	1.01	38.2
D/E to A	0.53	0.55	0.54	38.0

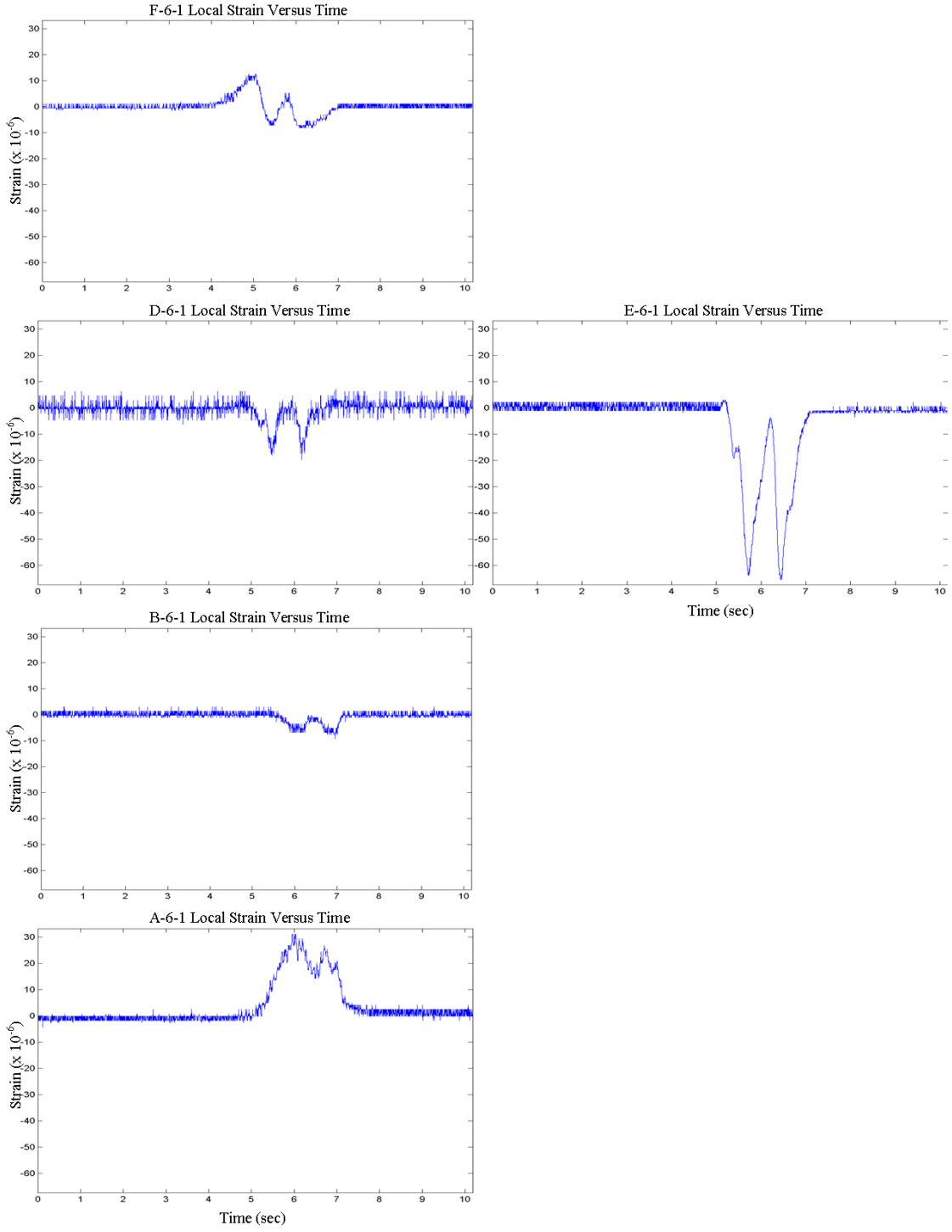

Figure 5.14. Local strain responses for the 6-1 sensors due to the semi loading in the left lane.

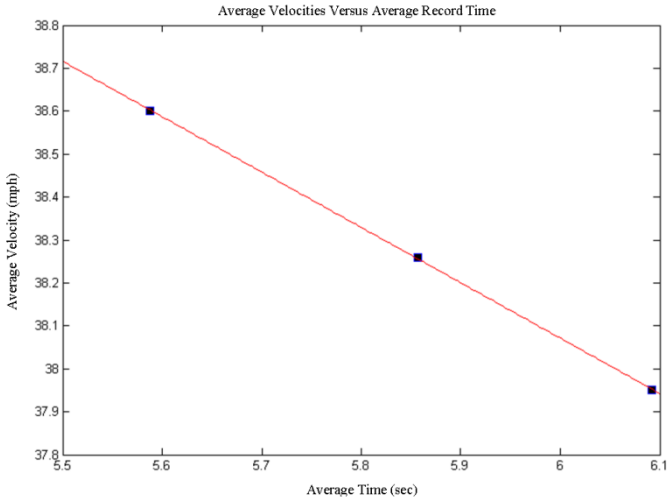

Figure 5.15. Average Velocities versus average times for the left lane loading with an applied linear fit.

The plot of the calculated velocities in miles per hour versus the averaged time in seconds between sensor pairs can be seen in Figure 5.11. Although only three points were established in Figure 5.15, a linear relationship between the velocities can be seen. Applying a linear fit produced an acceleration of -1.3 mph per second.

5.7.2 Middle Lane Loading Characteristics

The middle lane loading characteristics were examined for the eighteen-wheel, six-axle flatbed seen in Figure 5.16. Figure 5.17 shows the strain versus time plots of the 6-1 sensors recorded while the flatbed crossed the bridge. Sensor C-6-1 was again omitted from the plots because no significant response could be seen. The most distinguishing characteristics of this load case were: (1) the prominent compressive strains, most notable from sensor A-6-1, but also from sensors F-6-1 and D-6-1; (2) the mimicry of peak magnitudes of all the sensors minus E-6-1; and (3) the defined peaks of sensor B-6-1. The higher overall strain responses were consistent with the fact that the flatbed was driving over the instrumented girder causing the girder to carry a large portion of the load. Also, the mild response of sensor E-6-1 was consistent with the centerline of the flatbed being slightly to the right of the instrumented girder.

Figure 5.16. Flatbed associated with the middle lane loading.

All three peaks were used to calculate the velocities. The time that the peaks were recorded for sensors F-6-1, D-6-1, B-6-1 and A-6-1 are listed in Table 5.9. The duration between each sensor pair for the three peaks, the average of these durations and the calculated velocities using the distances from Table 5.6 are presented in Table 5.10.

Table 5.9. Recorded times of the three peaks associated with the middle lane loading.

	Time (sec)		
Sensor	**Peak 1**	**Peak 2**	**Peak 3**
F-6-1	4.90	5.20	5.52
D-6-1	5.60	5.96	6.36
B-6-1	6.15	6.51	6.90
A-6-1	6.32	6.66	7.05

Table 5.10. Time durations between stirrups and the calculated velocities for the middle lane loading.

	Duration (sec)				
Stirrups	**Peak 1**	**Peak 2**	**Peak 3**	**Average**	**Velocity (mph)**
F to D	0.70	0.77	0.83	0.77	23.6
F to B	1.25	1.31	1.37	1.31	25.5
F to A	1.42	1.46	1.52	1.47	26.2
D to B	0.55	0.55	0.54	0.54	28.2
D to A	0.72	0.70	0.69	0.70	29.1
B to A	0.17	0.15	0.15	0.16	32.1

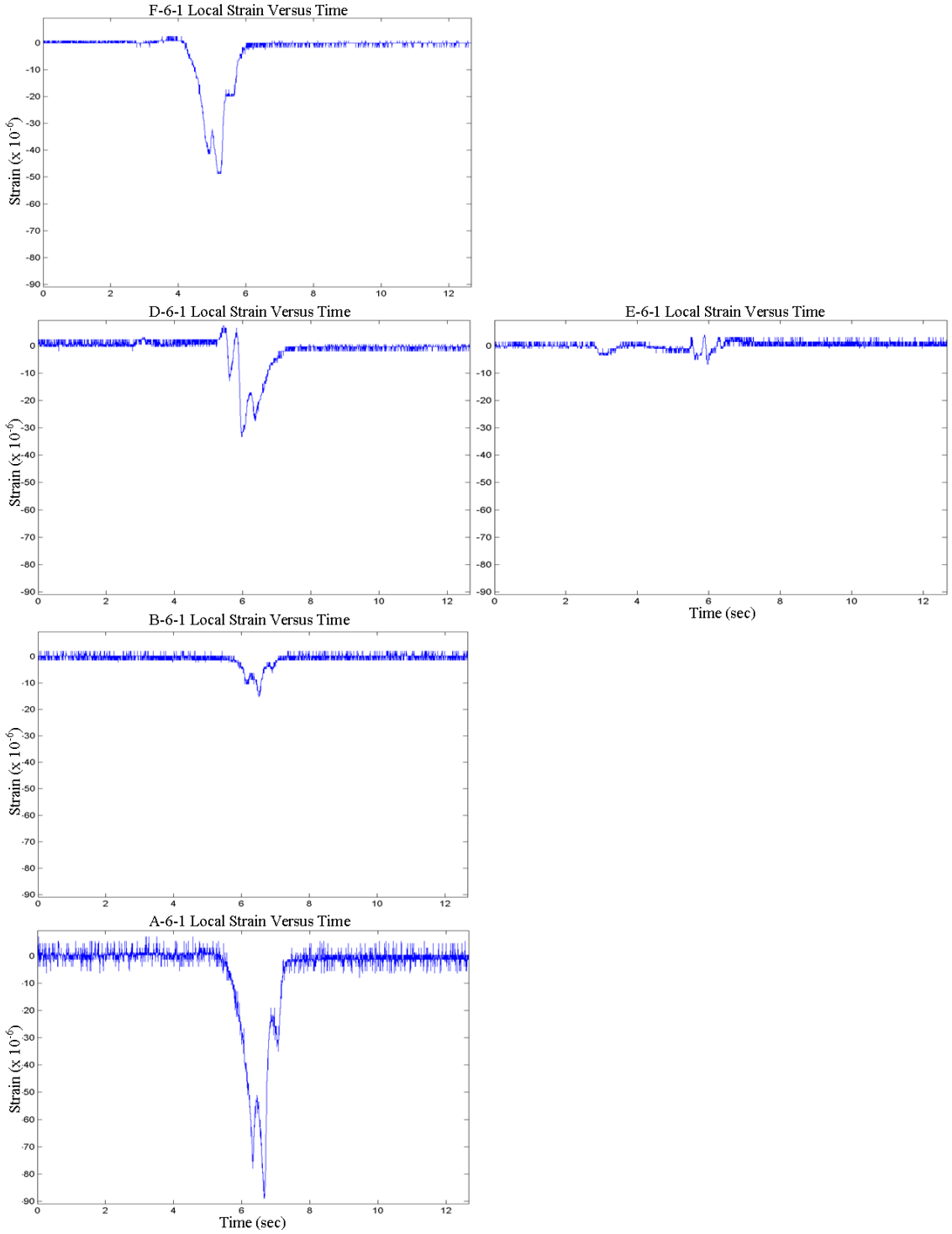

Figure 5.17. Local strain responses for the 6-1 sensors due to the semi loading in the middle lane.

Plotting the average velocities against the average times, and applying a linear curve fit produced an acceleration of 8.17 mph per second (see Figure 5.18).

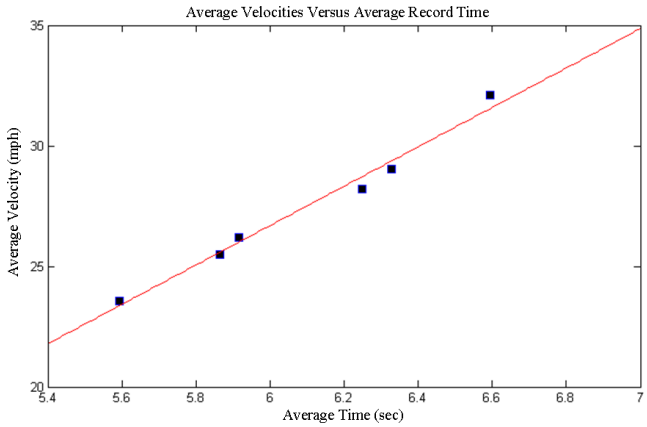

Figure 5.18. Average velocities versus average times for the middle lane loading with an applied linear fit.

5.7.3 Right Lane Loading Characteristics

The right lane loading characteristics were examined for the three-axle charter bus seen in Figure 5.19. Figure 5.20 shows the strain versus time plots of the 6-1 sensors recorded while the bus crossed the bridge. Sensor C-6-1 was again omitted from the plots because no significant response could be seen. Sensor B-6-1 also had no well defined response but is presented for consistency. The most distinguishing characteristics of this load case were the lack of any significant strains, and the existence of only a single peak. The lack of significant strain responses is consistent with the fact that the right lane was the furthest lane from the instrumented girder.

Furthermore, since only two peaks were defined enough to use in the velocity calculation, only a single average velocity was established. The velocity for the bus was calculated to be 27.75 mph.

Figure 5.19. Charter bus associated with the right lane loading.

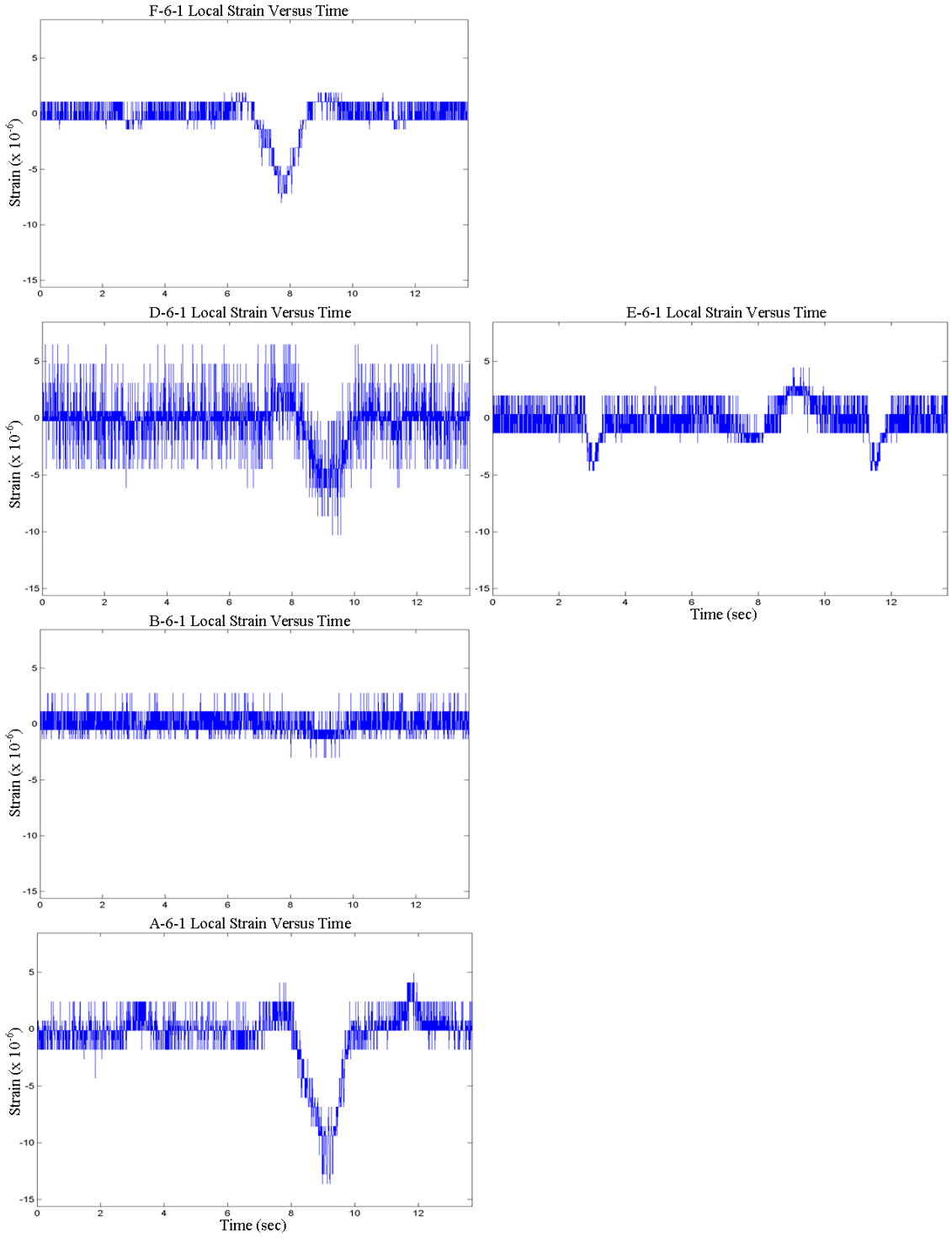

Figure 5.20. Local strain responses for the 6-1 sensors due to the bus loading in the right lane.

5.7.4 Combined Loading Characteristics

Between Figure 5.14, Figure 5.17, and Figure 5.20 a clear picture can be established between the individual loading conditions of the three lanes. Unfortunately, this ability was lost for loading conditions that incorporate multiple vehicles. Figure 5.21 shows the sensor strain responses for a loading case involving a two-axle refrigerated truck in the right lane being passed by two consecutive SUVs in the middle lane. All of the peaks in the strain records were similar in magnitude. There was no way to distinguish from the strain plots alone which peaks corresponded to each vehicle. The reason for this was that all of the sensors are placed on the same girder, resulting in a one dimensional representation of the two dimensional system.

5.7.5 A Note on the Compressive Responses

In the design of the CFRP strengthening, it was predicted that the strain response of the sensors would be primarily tensile in nature due to the shear loads. Instead the response was primarily compressive. The reason for this unpredicted behavior has not been thoroughly investigated due to the consistently small recorded strain values, but the following reason for this behavior has been proposed.

The cause of the compressive strains was most likely due to the shrinkage of the concrete infill. This shrinkage crack has caused the girder and the concrete infill to act as separate components of the same system. When the girder was loaded, the gap closed. The closure of this gap resulted in the compression of the CFRP stirrups, which resulted in the recorded compressive strains seen in the data files.

5.7.6 Global Behavior

The global strains of all of the sensors are presented in Appendix G. Although the diurnal and annual temperature effects can be seen in the cyclic variations, it has been observed that the global behavior was slightly erratic with no predictable trend. All of the sensors on stirrup A, minus sensor A-6-1, showed a consistent cyclic behavior with a slight compressive drift. Sensor A-6-1's cyclic behavior and drift were both doubled compared to the other sensors on stirrup A. For stirrup B, the cyclic behaviors were consistent, but the drift varies from compressive to tensile. The same can be seen for stirrup C. The sensors at D and E appeared to be relatively consistent with no apparent drift, but these sensors were not operational for the first year and as such the initial behavior is unknown. Finally, the drift and cyclic behaviors of the sensors on stirrup F varied in amplitude as well as in the drift.

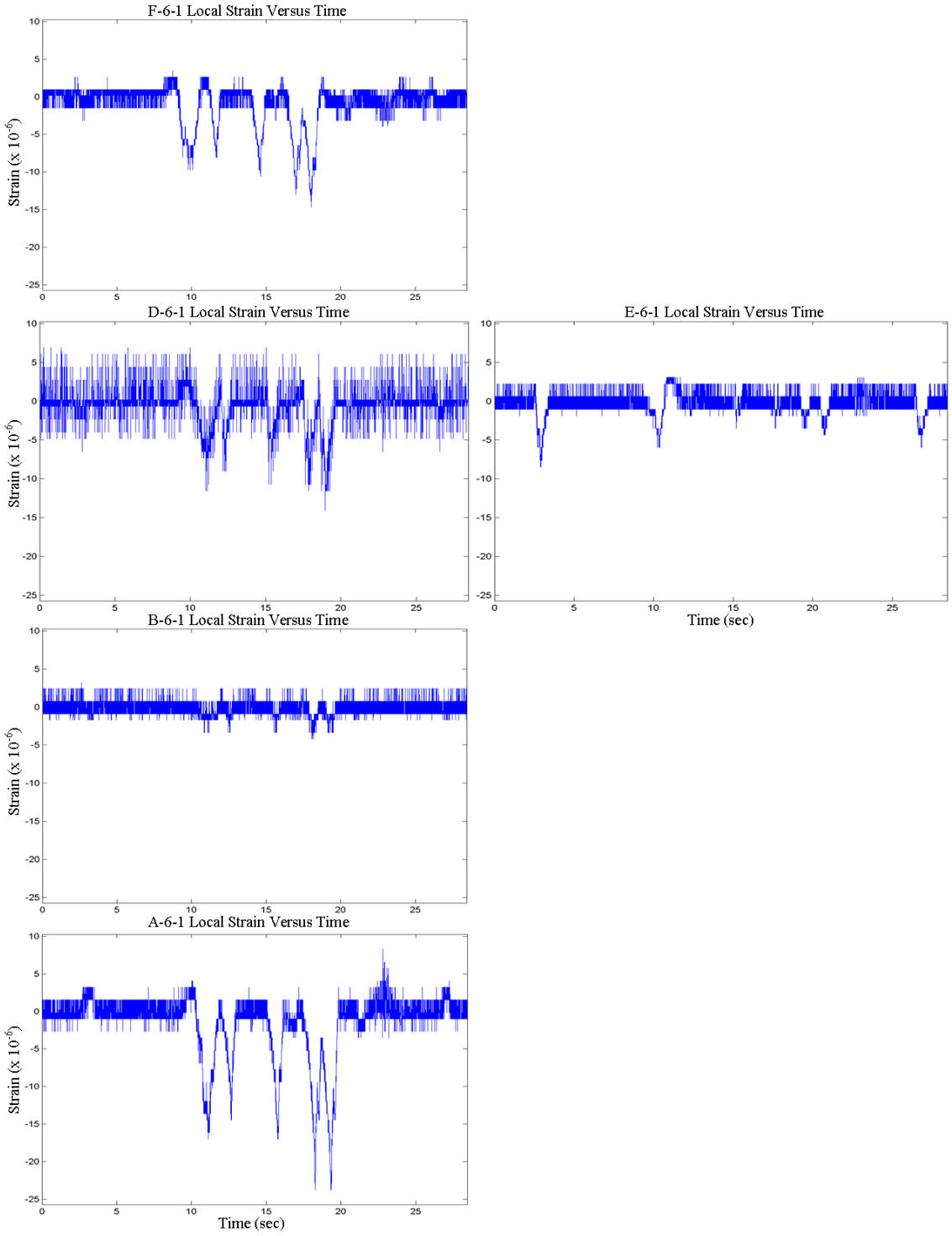

Figure 5.21. Local strain responses for the 6-1 sensors due to multiple loading.

5.8 Conclusion

The analysis of the data obtained from the FBG instrumentation of the CFRP shear strengthened SLBB demonstrated that the system was working effectively over the duration of the recorded data. The FBG system was determined to be working properly and producing reliable information for each instrumented stirrup. The possible limit states of the CFRP stirrups were individually examined and none of these limits were observed. Finally the local and global behaviors of the system were analyzed. From the local behavioral analysis it was shown that the potential to monitor the traffic loading (including the vehicle velocities) exists, but would require additional sensors placed across the width of the bridge in order to obtain a two dimensional representation required to separate the individual vehicles. The global behavior was both erratic and unpredictable, but the separation of the local strains removed the need to compensate for these behaviors. Furthermore, the overall magnitudes of the global stains were so small that it was unnecessary to perform a more stringent analysis.

Although the analysis demonstrated that the SLBB was in a good working condition over the course of the collected data, the system cannot be deemed as a successful long-term SHM system. The reason for this is the unreliability of the router obtained from the internet provider. The potential benefits of a SHM system are lost when someone has to be sent out every few months to reboot the system. Fortunately, the router is not critical to the instrumentation itself, only to the remote collection of the data and can easily be replaced.

CHAPTER 6. CONCLUSIONS

The application of sensor-based SHM systems to civil infrastructures has gained the attention of many researchers across the globe over the past two decades. The development of new FOS technologies and new FRP composite materials, as well as the continual advancements in data transmission and storage capabilities can be directly attributed to this attention. Although the application of sensor-based SHM systems is gaining the attention of many researchers, their widespread application is not yet a reality. The primary reason for the lack of widespread applications is that the establishment of standardized systems that are adaptable and provide some level of guaranteed monitoring performance regardless of the behavior of the structure has yet to be achieved.

With the continual rise in the number of structures in the United States that need to be rehabilitated, coupled with the limited resources allocated to their rehabilitation, the need for standardized SHM systems to aid in the maximization and prioritization of these limited resources is apparent. Therefore, it is the intention of this work to demonstrate that the combination of FRP laminates and FBG sensors, coupled with the generalized data management, post-processing, and analysis procedures developed in Chapter 4 can produce such a standardized and adaptable system. In addition to creating a standardized SHM system, the combination of FRP laminates and FBG sensors creates the ability to simultaneously rehabilitate and instrument RC structures which can reduce the overall installation costs.

In Chapter 5, a case study was presented which demonstrated the effectiveness of the developed procedures, and their ability to assess the performance of both the FRP laminates and the sensors themselves without requiring any complicated compensation techniques or the knowledge of the behavior of the structure. It was also seen that the system has the potential to monitor not only the performance of the structure, but also the short term dynamic loading conditions.

APPENDIX A. MATLAB SCRIPT DESCRIPTION

Appendix A provides the details of the functions, operations, and algorithms of the MATLAB script developed to manage and post-process the original datasets obtained from the SLBB project. Each function is written and saved as its own mini-script .m file. These functions are presented in the same format and order as they are called. The format for calling functions is:

[output variables] = function name(input variables).

The procedure is as follows:

- The paths to the input folder, local folder and global files are established.
- The number of files in the input folder is determined.

(The remainder of the script is performed for every file in the input folder.)

- The file is loaded.
- [S_mod, S_mod2, err2, err_mssg2] = rowinfo(S)
  - This function determines if there are any breaks in time in the dataset. Three categories are established to determine what to do in the event of a large break in time. If there is a break in time, and that break occurs before 300 data points or after 300 data points are left, then the smaller portion of the data is discarded. 300 data points is the threshold so that at least 100 data points can potentially be used for the null wavelength calculation. If the break in time occurs at any other point in the dataset, then the file is split and each portion of the original dataset is considered an independent dataset. The break in time is check is against 10 Hz.
  - Input variables:
    - S - The original dataset
  - Output variables:
    - S_mod - Either the original dataset, the undiscarded portion of the data, or the first portion of the split file
    - S_mod2 - The second portion of the data if split, remains blank if unused
    - srow - The modified number of rows
    - srow2 - The number of row of second portion
    - err2 - numeric value, 1 if the first portion is removed, 2 if the end portion is removed, 3 if the set is split
    - err_mssg2 - message describing the error

- [v_date, f_date, n_date, v_date2, f_date2, n_date2]=timestamp(err2, S_mod, S_mod2)
  - This function takes the first time value of the file, converts the time from Linux format to MATLAB's format, and sets it as the timestamp for the data. The timestamp is established in vector, numeric, and string formats. In the output variables, yyyy, mm, dd, HH, MM, and SS stand for the year, month, day, hour, minute, and seconds respectively. The number of letters denotes the number of digits used. If there exists more second digits than described here, then round down ALWAYS. The output variables that have a 2 at the end of their name are the same as the variables without the 2 but for the second portion of the data if it was split.
  - Input Variables:
    - err2 - the error value associated with the rowinfo function
    - S_mod – the original modified input file
    - S_mod2 - second portion of modified input file if the data was split
  - Output Variables:
    - v_date - the date vector from time conversion with the format [yyyy, mm, dd, HH, MM, SS]
    - f_date - the date sting to use for filename with the format "yyyymmddTHHMMSS"
    - n_date - the numeric timestamp in MATLAB's format
- [path, path_original, path_wave, path_strain, path_strainerror, path_log, anlys_rpt] = createpaths (f_date, spath)
  - This function takes the date string timestamp produced from the timestamp function and checks to see if a folder for the timestamp already exists. If the folder does not exist, it is created as well as the paths to each of the local files that will be created. If the folder exists an error value is returned to prompt the program to move to the next input file.
  - Input Variables:
    - f_date - timestamp date string
    - spath - the path to the location where each data folder will be created
  - Output Variables:
    - path - the location of the folder created for post processing files
    - path_original - the filename and path for the original dataset copy
    - path_wave - the filename and path for the reformatted wavelengths
    - path_strain - the filename and path for the local strains
    - path_log - the filename and path to the log file for this dataset
    - anyls_rpt - numeric value of 1 if the folder exists, and zero otherwise
- If the file was split then the createpaths.m function is repeated with a 2 attached to the end of each variable's name.

- The original datasets are copied to their new location.
- [sensor_title, event_time, all_wave, col_case, err1, err_mssg1] = channel2group(S_mod)
  - This function determines if the dataset was recorded remotely or on site, designates the appropriate column where the sensor data starts, determines what channels were operational, and then designates and rearranges the wavelength data into the predetermined format. It also calculates the event time that will be associated with the local processed files.
  - Input Variables:
    - S_mod - unprocessed data set
  - Output Variables:
    - sensor_title - a formatted list of each sensors name
    - event_time - time in seconds starting from zero for the first time value
    - all_wave - the reformatted local wavelengths
    - col_case - designation value for whether the data was remotely recorded or recorded on site
    - err1 - numeric value indicating whether a channel was non-operational during the recording of the dataset
    - err_mssg1 - string message indication which channel was non-operational
- [all_null, null_std, err_null, mssg_null] = nullwavecalc (all_wave, filter_value, amp_factor, sensor_title,f_date)
  - This function calculates the null wavelengths of the sensors following the algorithm described in section 4.2.2.1.
  - Input Variables:
    - all_wave - formatted wavelength sets
    - filter_value - designated range for the variation check
    - amp_factor - amplification factor for the variation check
    - sensor_title - formatted sensor title list
    - f_date - file format of the timestamp
  - Output Variables:
    - all_null - calculated null wavelength values
    - null_std - null wavelength standard deviations
    - err_null - numeric value indicating if a null wavelength could not be calculated
    - mssg_null - message reporting which sensor’s null could not be calculated

- [all_strain, strain_max, strain_min, strain_err] = null2strain(all_wave, all_null, null_std)
  - This function calculates the local strain values and their errors for each sensor set. It also determines the maximum and minimum strains for each set.
  - Input Variables:
    - all_wave – formatted wavelength sets
    - all_null– calculated null wavelength values
    - null_std– null wavelength standard deviations
    - sensor_title – formatted sensor title list
  - Output Variables:
    - all_strain – calculated local strain sets
    - strain_max – maximum strains
    - strain_min – minimum strains
    - strain_err – calculated local strain errors
- [global_strain, global_strain_err] = globalstrain(all_null, null_std, g_null_path)
  - This function calculates the global strain value for each sensor and their errors.
  - Input Variables:
    - all_null– calculated null wavelength values
    - null_std– null wavelength standard deviations
    - g_null_path – path to the null wavelength file
  - Output Variables:
    - global_strain – calculated global strain values
    - global_strain_err – calculated global strain errors
- All of the local files are written.
- [ ] = globalfileupdate(path, update, n_date)
  - This function is applied to each global variable. It loads the existing file, determines the row location in the set where the new variables are to be inputted, and then saves the updated file. There is no output variable associated with this function.
  - Input Variables:
    - path – the path to whichever file is being updated
    - update – the column vector of the new values to be inputted
    - n_date – numeric timestamp value to find the appropriate data location

- [ ] =f ilereport(path_log, err1, err_mssg1, col_case, err2 ,err_mssg2, err_null, mssg_null)
  - This function writes all of the errors and which type of file the original was into a log file to be stored in the local folder. There is no output variable associated with this function.
  - Input Variables:
    - path_log – path to the log file
    - err1 - numeric value indicating whether a channel was non-operational during the recording of the dataset
    - err_mssg1 - string message indication which channels were non-operational
    - col_case - designation value for whether the data was remotely recorded or recorded on site
    - err2 - numeric value, 1 if first portion of the original dataset was removed, 2 if end portion of the original dataset was removed, and 3 if the dataset was split
    - err_mssg2 - message describing the error associated with the possible removal or slitting of the original dataset
    - err_null - numeric value indicating if a null wavelength could not be calculated
    - mssg_null - message reporting which sensor's null could not be calculated
- If the original file was split then the functions channel2group.m through filereport.m are repeated for the second portion of the original dataset.

APPENDIX B. SECTION 5.5 SUPPLEMENT - STIRRUP B

B.1 FBG System Analysis and Results

For stirrup B, 1,831 or 2.67% of the total sensor datasets did not have a null wavelength established from the automated post-processing. The individual sensor breakdown of these values, their respective percentages, as well as the range of amplification values can be seen in Table B.1.

Table B. 1. Breakdown of the number and percentage of individual sensor datasets where a null wavelength value was not established for stirrup B, as well as the range of amplification factors required to processes the sets.

	No established null wavelength		Amplification range	
Sensor	Number of sets	%	β Min	β Max
B-6-4	49	0.36	1.6	2.0
B-6-1	154	1.12	1.4	2.0
B-12-1	343	2.49	1.4	2.0
B-18-1	837	6.08	1.4	1.8
B-24-1	448	3.25	1.4	2.0

As can be seen from Table B.1, the maximum amplification of the maximum variation between successive data points was 2.0. This maximum amplification was deemed insufficient to warrant an investigation into the individual datasets.

The null wavelength error plots for the sensors at stirrup B are presented in Figure B.1. From these plots it can be seen that two abnormally high value exist from all five of the sensors. These error values were 0.006 nm and 0.007 nm associated with sensor B-24-1 recorded on October 22nd, 2009 at 5:27 PM and sensor B-18-1 recorded on May 18th, 2010 at 9:54 AM respectively. Although the errors were higher than the norm, the values were still too small to warrant an investigation into the local strain files.

It can also be seen from Figure B.1 that the null wavelength errors for sensors B-6-1 and B-6-4 never exceeded the recording precision of the sensors (0.002 nm). Sensor B-12-1's errors only exceeded the sensors precision by 0.001 nm. For sensors B-18-1 and B-24-1 the upper bound of the null wavelength error was typically 0.004 nm.

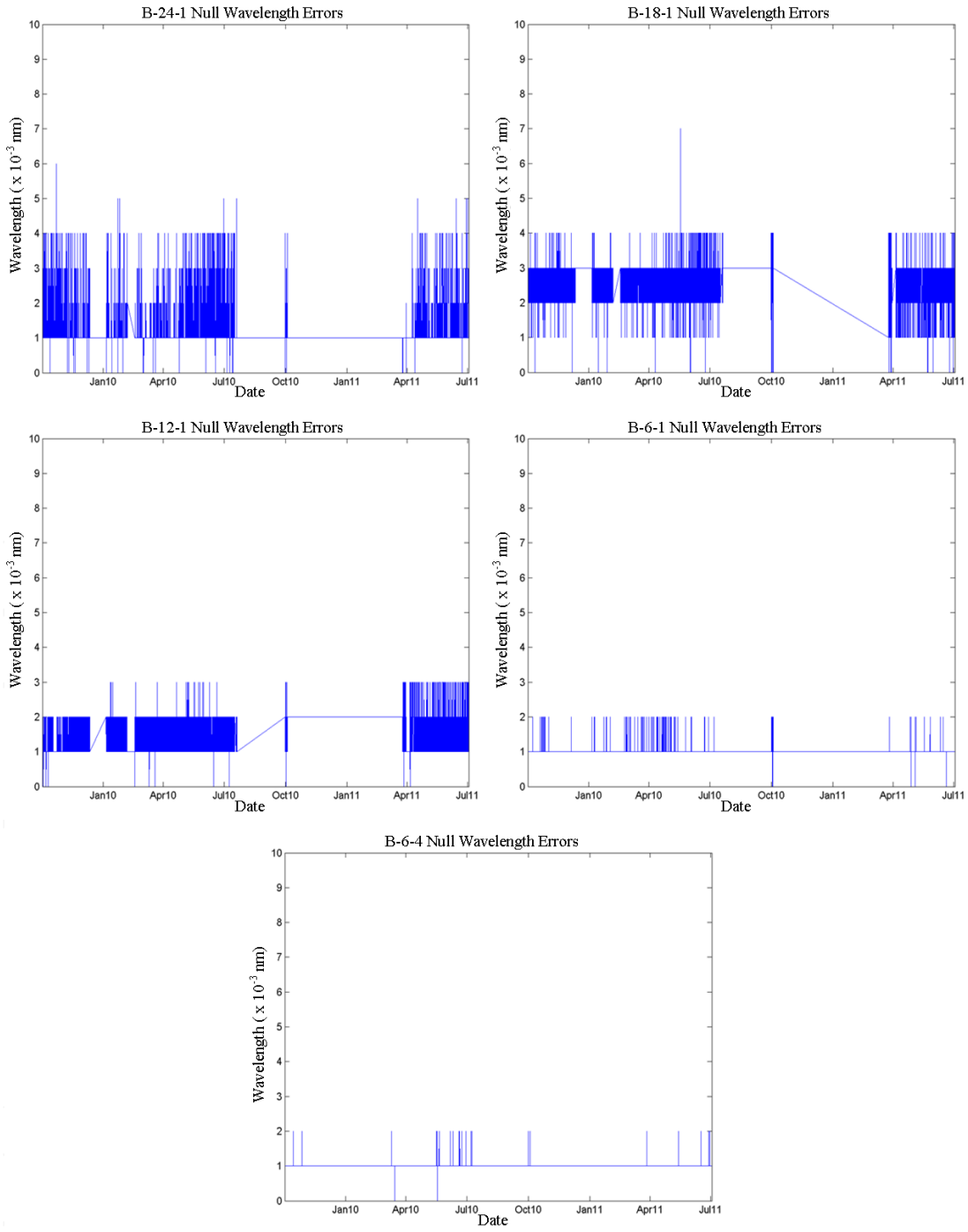

Figure B. 1. Null wavelength error versus the dates they were recorded for sensors on stirrup B.

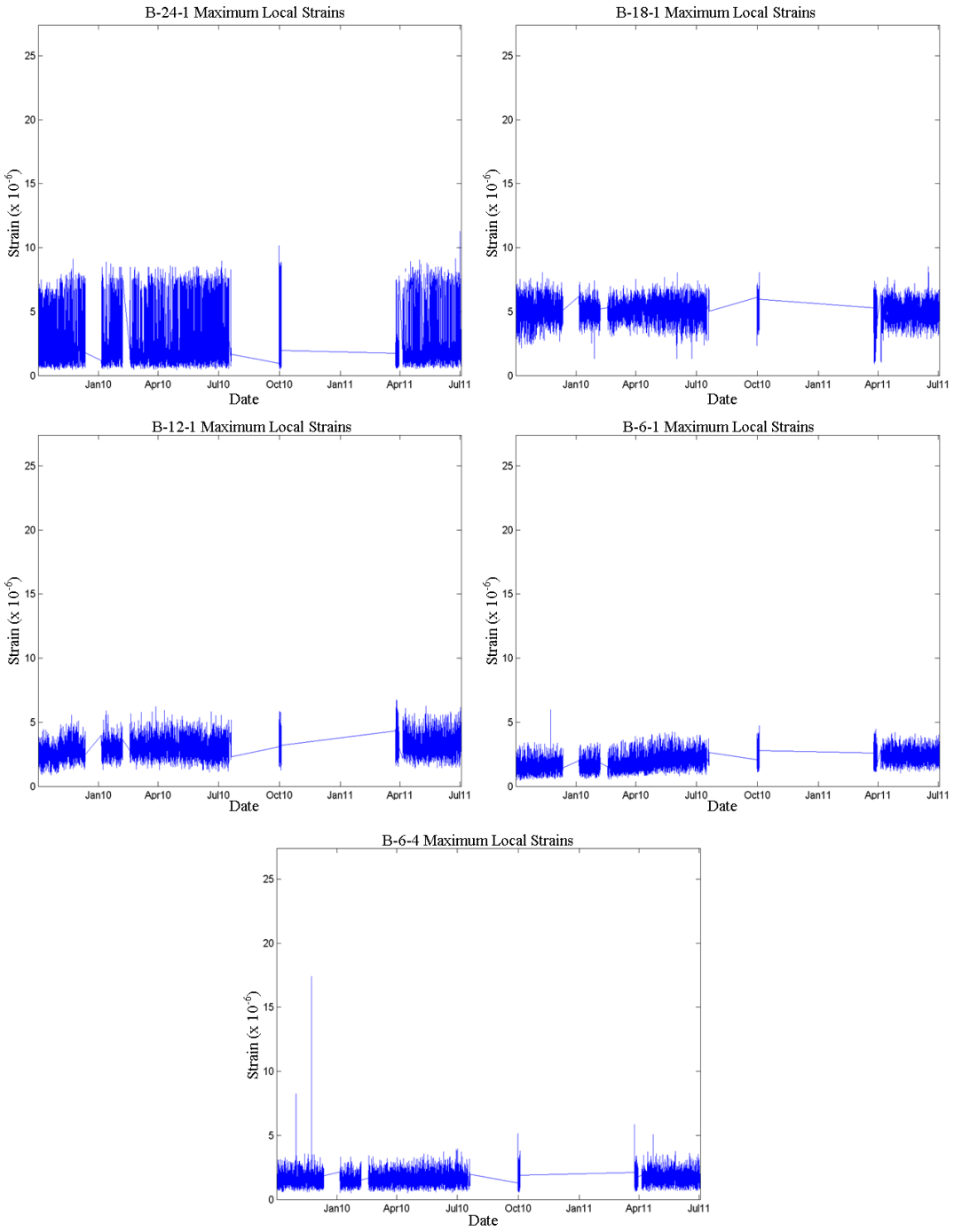

Figure B. 2. Maximum local strains versus the dates they were recorded for sensors at stirrup B.

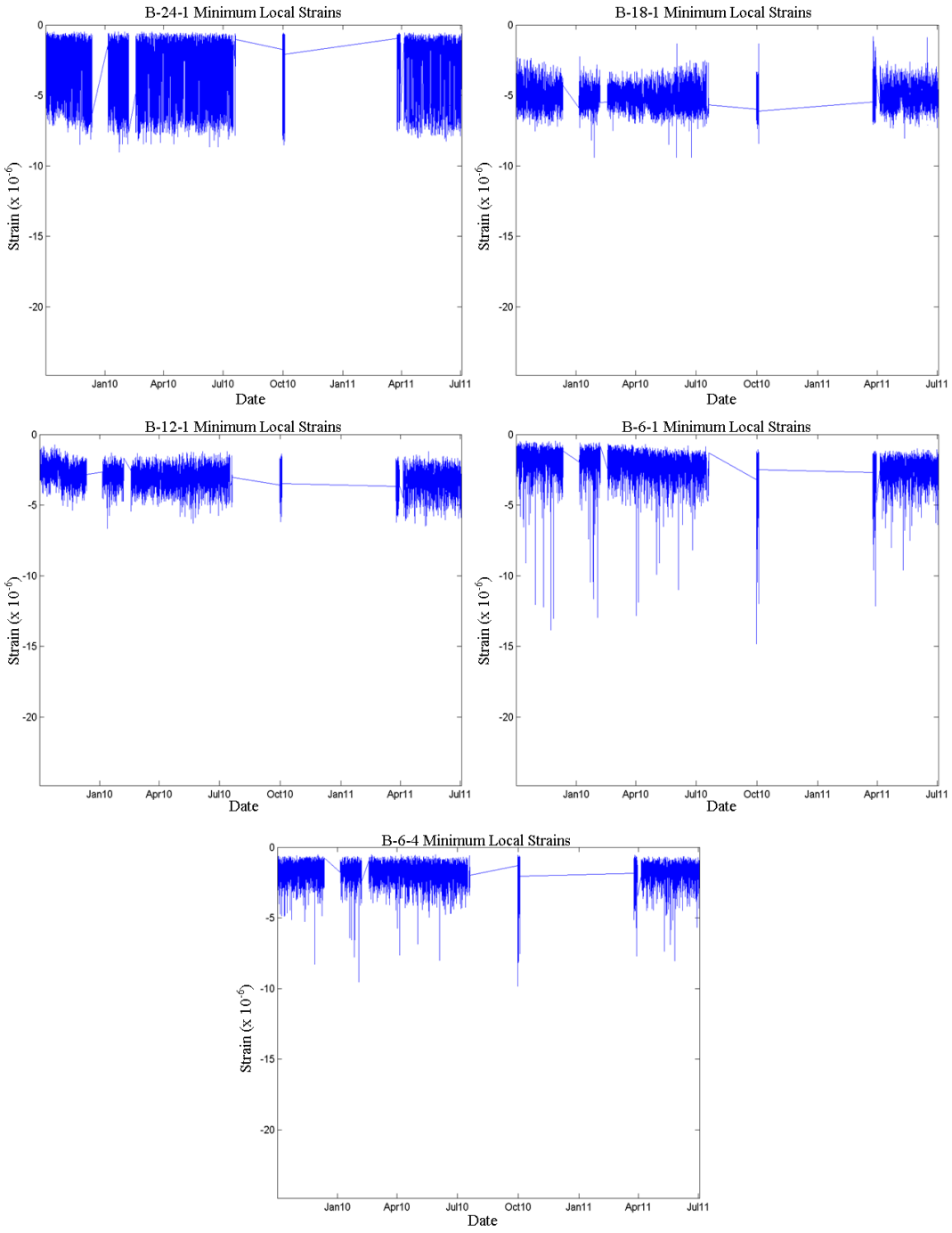

Figure B. 3. Minimum local strains versus the dates they were recorded for sensors at stirrup B.

Figure B.2 and Figure B.3 show the plots of the local maximum and minimum strains plotted against the date they were recorded for the sensors on stirrup B. Through examining these plots it can be seen that the maxima remained relatively constant for all of the sensors. Therefore, FBG debonding has not occurred for any of the sensors on stirrup B.

Through the correction of the datasets with no null wavelength calculated from the initial post-processing, and the assessment of abnormally high null wavelength values, the anomalies were corrected. Comparing the null wavelength errors against the precision of the sensors demonstrated that the null wavelength errors lie within a justifiable range. Checking for a decrease in maxima values demonstrated that the FBG sensors have not debonded. Therefore, it can be concluded that the FBG system on stirrup B was in good working order over the range of recorded data.

B.2 FRP Limit Analysis and Results

The envelope plots of the growth in the absolute local maximum and minimum strains values over the duration of data presented in this work for the sensors on stirrup B can be seen in Figure B.4. Sensors B-6-1 and B-6-4 were the sensors applied over the shrinkage crack between the infill and bottom bulb of the girder. A quick observation of these graphs shows that by 2010 the maxima for all of the sensors became relatively constant. A few increases in the absolute local minimum strain for all of the sensors not located over the shrinkage crack can be seen, but these increases were only a few microstain. Furthermore, with both the absolute local maximum and minimum strains for all of the sensors on stirrup B being less than twenty microstrain, the comparison of the sensors not applied over the shrinkage crack to sensors B-6-1 and B-6-4 was unnecessary. Therefore, it can be concluded that debonding or peel has not occurred for stirrup B.

The absolute minimum strains for B-6-1 and B-6-4 were significantly smaller in magnitude than the absolute minimum held by sensor A-6-1. Since sensor A-6-1 has not buckled, and it has been concluded that peel has not occurred for stirrup B, composite buckling was not considered to be a possible limit state for Stirrup B.

The continual activity of sensors B-6-1 and B-6-4 as seen through the local maximum and minimum plots in Figures B.3 and B.4, respectively, confirmed that adhesive failure has not occurred for stirrup B.

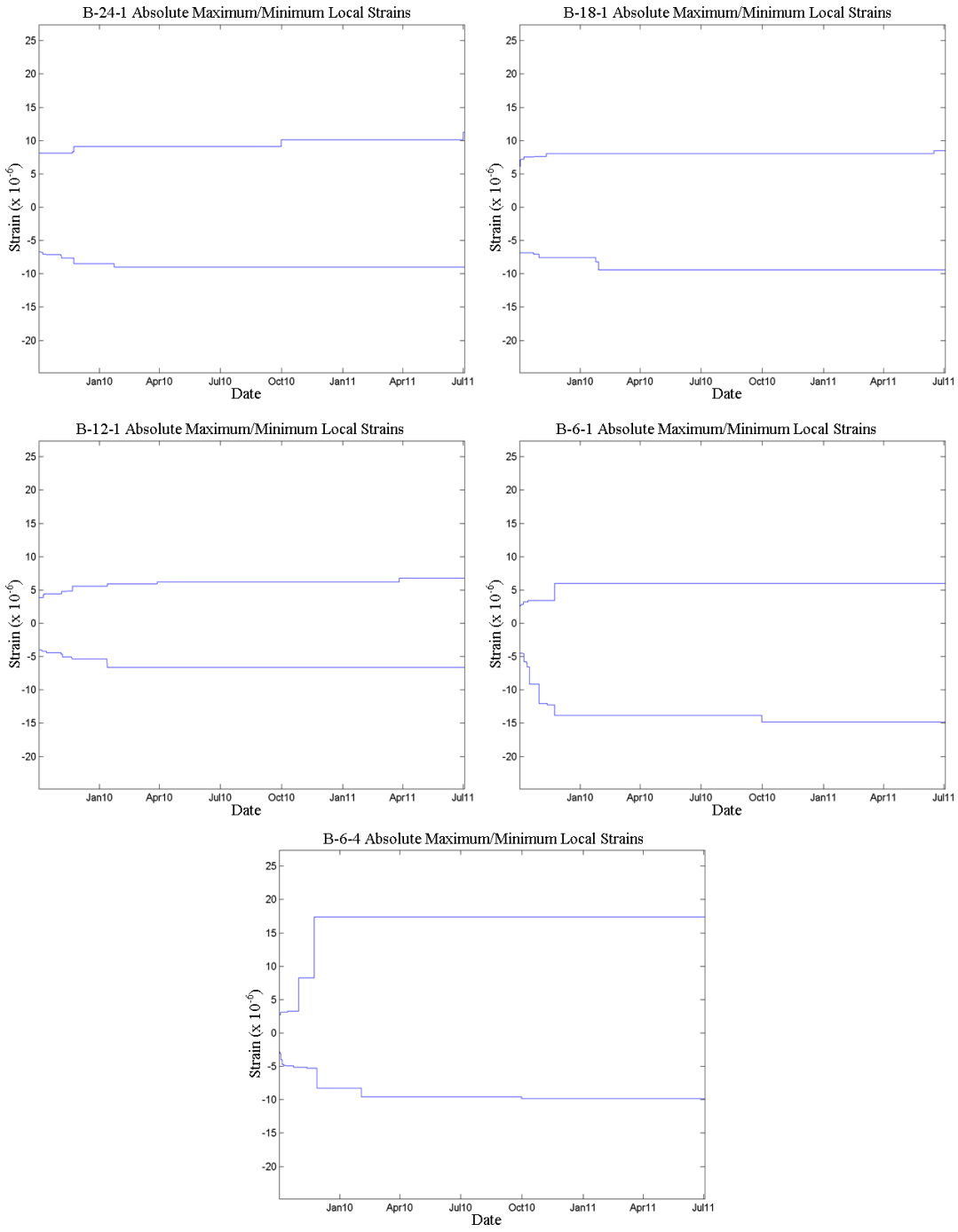

Figure B. 4. Absolute local maxima envelope versus recording date for sensors on stirrup B.

With the design-specified required minimum ultimate tensile strain of 0.0126, the first threshold value, T1, became 6,300 microstrain. Table B.2 lists the maximum global strain ε_{GM}, the maximum local strain ε_{LM}, the absolute strain, ε_{abs}, obtained using method 1 (see 4.2.4.4.1), as well as the normalized percentage of the absolute strain against T1 for each sensor on stirrup B. From Table B.2 it can be seen that the maximum absolute strain for all of the sensors on stirrup B only reaches 1.11% of T1. Therefore, the induced tensile strains on stirrup B were nowhere near the onset of tension rupture.

Table B. 2. The maximum global strains, maximum local strains, absolute strains, and the normalized percentage of the absolute strains against the threshold T1 for each sensor on stirrup B.

	T1 = 6300 x 10^{-6}			
	Maximum strains (10^{-6})			
Sensor	**Global (ε_{GM})**	**Local (ε_{LM})**	**Absolute (ε_{abs})**	**% of T1**
B-6-4	53	17	70	1.11
B-6-1	262	6	268	4.25
B-12-1	37	7	44	0.70
B-18-1	38	8	46	0.73
B-24-1	48	11	59	0.94

For the sensors on stirrup B, through both the individual assessment of each sensor as well as the comparison of the sensors not applied over the shrinkage crack to sensors B-6-1 and B-6-4, no debonding or peel has been observed. It has also been determined that the limit states of composite buckling and adhesive failure have not occurred. Finally, the absolute strain values did not come remotely close to the T1 threshold value. Therefore, it can be concluded that stirrup B was in good working condition over the duration of the recorded data.

APPENDIX C. SECTION 5.5 SUPPLEMENT - STIRRUP C

C.1 FBG System Analysis

For stirrup C, 846 or 1.23% of the total sensor datasets did not have a null wavelength established from the automated post-processing. The individual sensor breakdown of these values, their respective percentages, as well as the range of amplification values can be seen in Table C.1.

Table C. 1. Breakdown of the number and percentage of individual sensor datasets where a null wavelength value was not established for stirrup C, as well as the range of amplification factors required to processes the sets.

	No established null wavelength		Amplification range	
Sensor	Number of sets	%	β Min	β Max
C-6-4	366	2.66	1.4	2.0
C-6-1	370	2.69	1.4	2.0
C-12-1	27	0.20	1.6	2.2
C-18-1	33	0.24	1.6	2.0
C-24-1	50	0.36	1.6	2.4

As can be seen from Table C.1, the maximum amplification of the maximum variation between successive data points was 2.4. This maximum amplification was deemed insufficient to warrant an investigation into the individual datasets.

The null wavelength error plots for the sensors at stirrup C are presented in Figure C.1. From these plots it can be seen that no abnormally high value existed for all five of the sensors.

It can also be seen from Figure C.1 that the null wavelength errors for sensors C-24-1, C-18-1, and C-12-1 never exceeded the recording precision of the sensors (0.002 nm). Sensor C-6-1 had a typical upper bound error of 0.003 nm but occasionally rose to 0.004 nm, and once to 0.005 nm. Sensor C-6-4 also had a typical upper bound of 0.003 nm with the occasional error of 0.004 nm.

Figure C.2 and Figure C.3 show the plots of the local maximum and minimum strains plotted against the date they were recorded for the sensors on stirrup C. Through examining these plots it can be seen that maxima remained relatively constant or increased over time for all of the sensors. Therefore, FBG debonding has not occurred for any of the sensors on stirrup C.

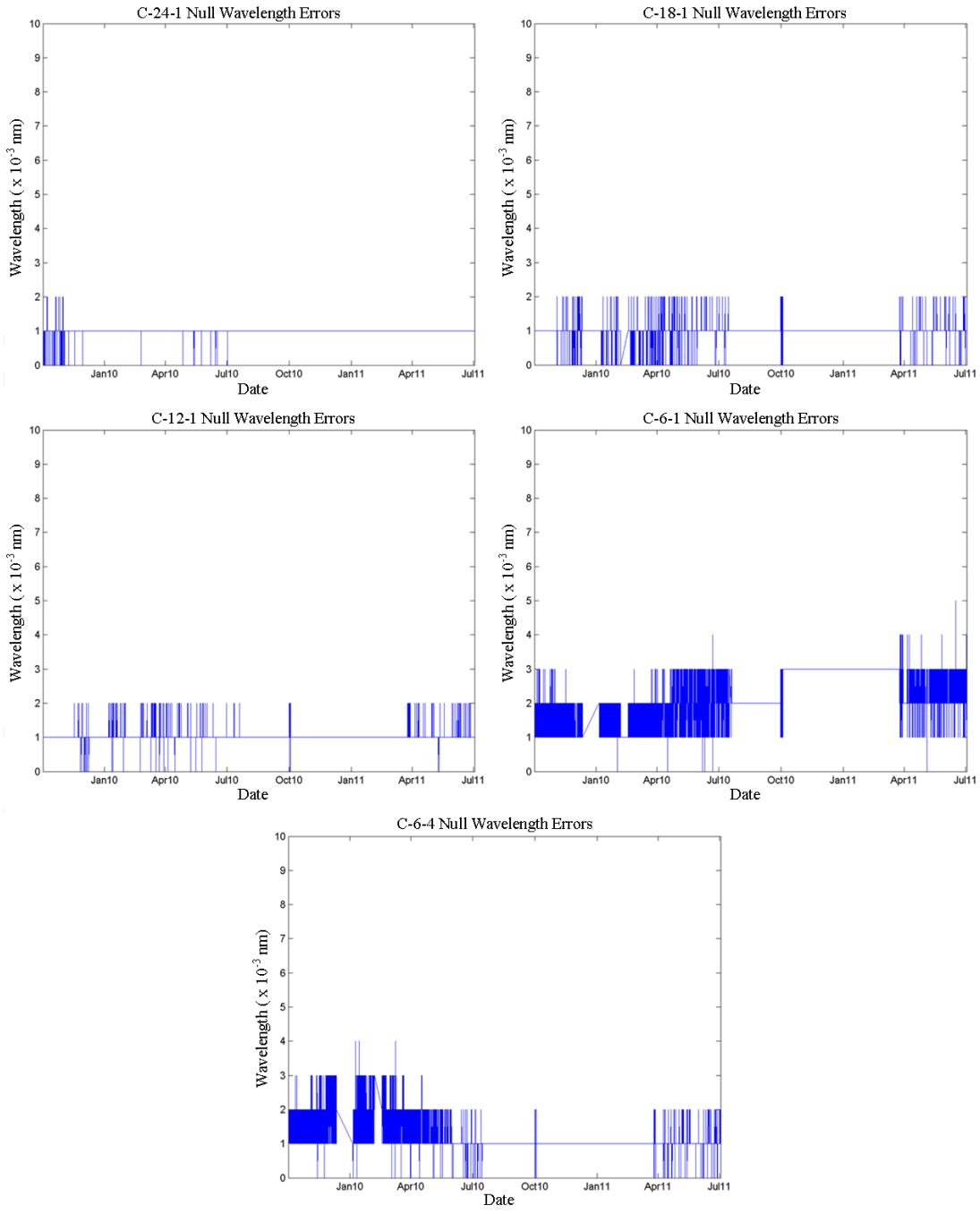

Figure C. 1. Null wavelength error versus the dates they were recorded for sensors on stirrup C.

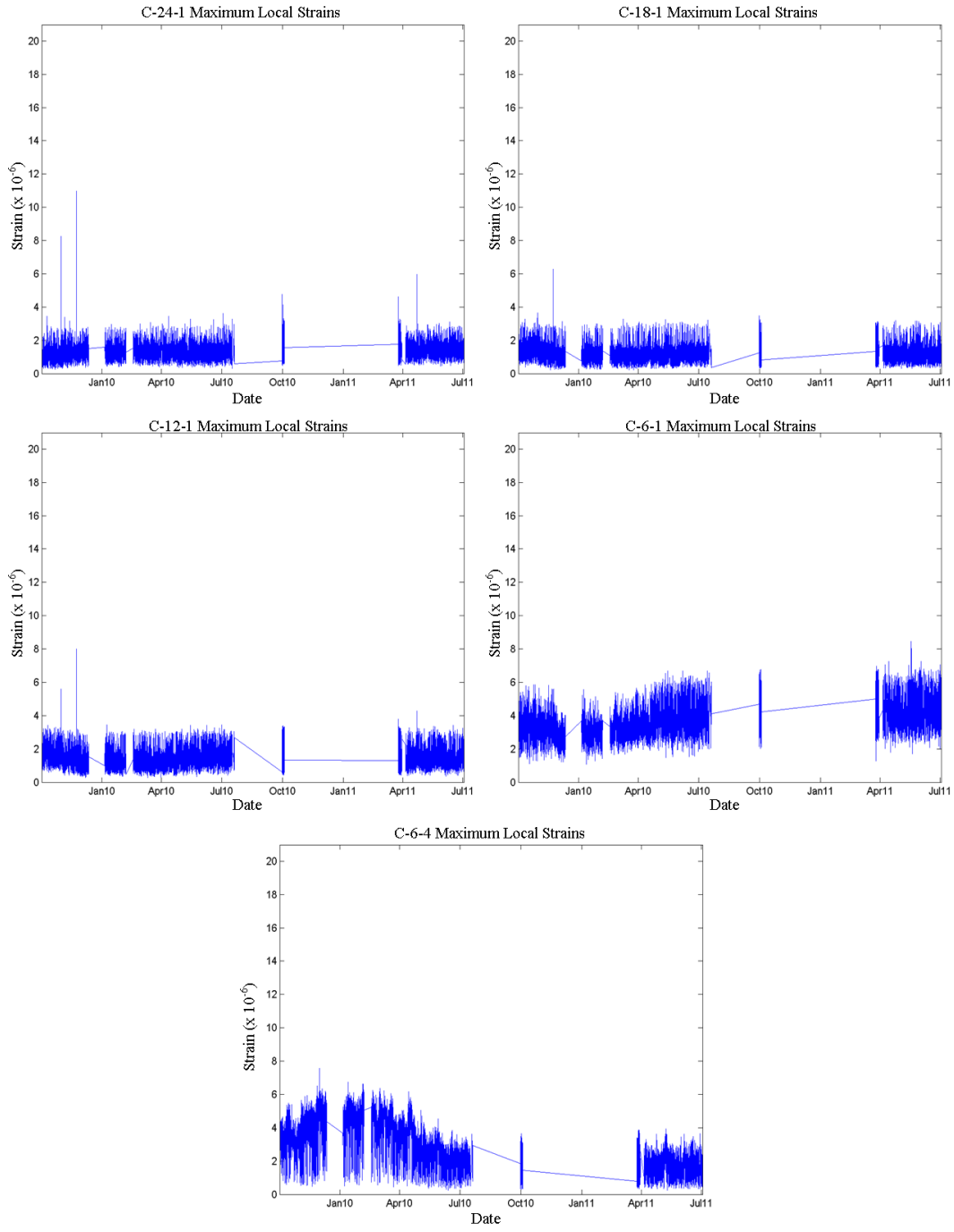

Figure C. 2. Maximum local strains versus the dates they were recorded for sensors at stirrup C.

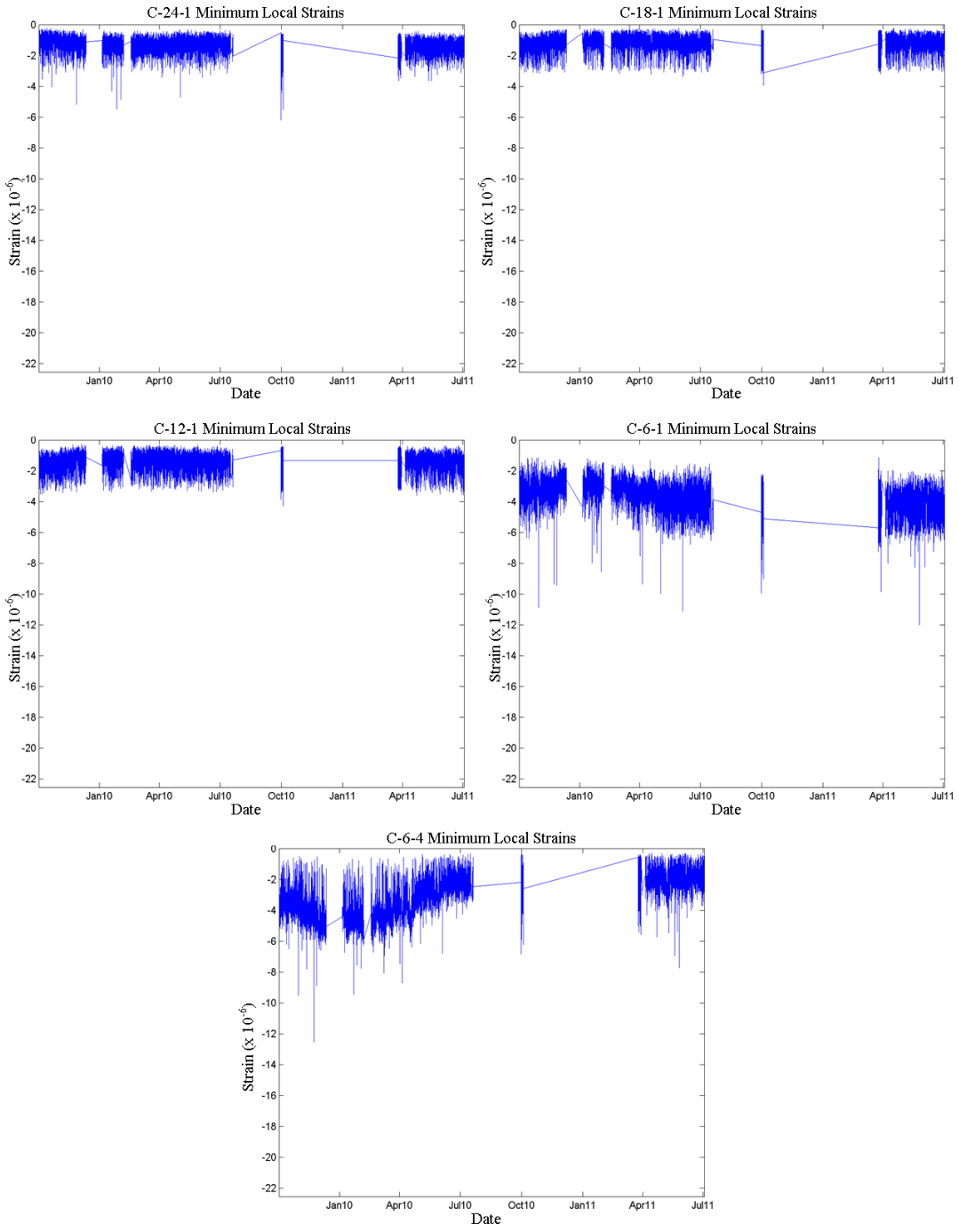

Figure C. 3. Minimum local strains versus the dates they were recorded for sensors at stirrup C.

Through the correction of the datasets with no null wavelength calculated from the initial post-processing and the assessment of abnormally high null wavelength values, the anomalies were corrected. Comparing the null wavelength errors against the precision of the sensors demonstrated that the null wavelength errors lie within a justifiable range. Checking for a decrease in maxima values demonstrated that the FBG sensors have not debonded. Therefore, it can be concluded that the FBG system on stirrup C was in good working order over the range of recorded data.

C.2 FRP Limit Analysis

The envelope plots of the growth in the absolute local maximum and minimum strain values over the duration of data presented in this work for the sensors on stirrup C can be seen in Figure C.4. Sensors C-6-1 and C-6-4 were the sensors applied over the shrinkage crack between the infill and bottom bulb of the girder. A quick observation of these graphs shows that by 2010 the maxima for all of the sensors became relatively constant. A few increases in the absolute local minimum strain for all of the sensors not located over the shrinkage crack can be seen, but these increases were by only a few microstain. Furthermore, with both the absolute local maximum and minimum strains for all of the sensors on stirrup C being less than fifteen microstrain, the comparison of the sensors not applied over the shrinkage crack to sensors C-6-1 and C-6-4 was unnecessary. Therefore, it can be concluded that debonding or peel has not occurred for stirrup C.

The absolute minimum strains for C-6-1 and C-6-4 are significantly smaller in magnitude than the absolute minimum held by sensor A-6-1. Since sensor A-6-1 has not buckled, and it has been concluded that peel has not occurred for stirrup C, composite buckling was not considered to be a possible limit state for Stirrup C.

The continual activity of sensors C-6-1 and C-6-4 as seen through the local maximum and minimum plots in Figures C.3 and C.4, respectively, confirm that adhesive failure has not occurred for stirrup C.

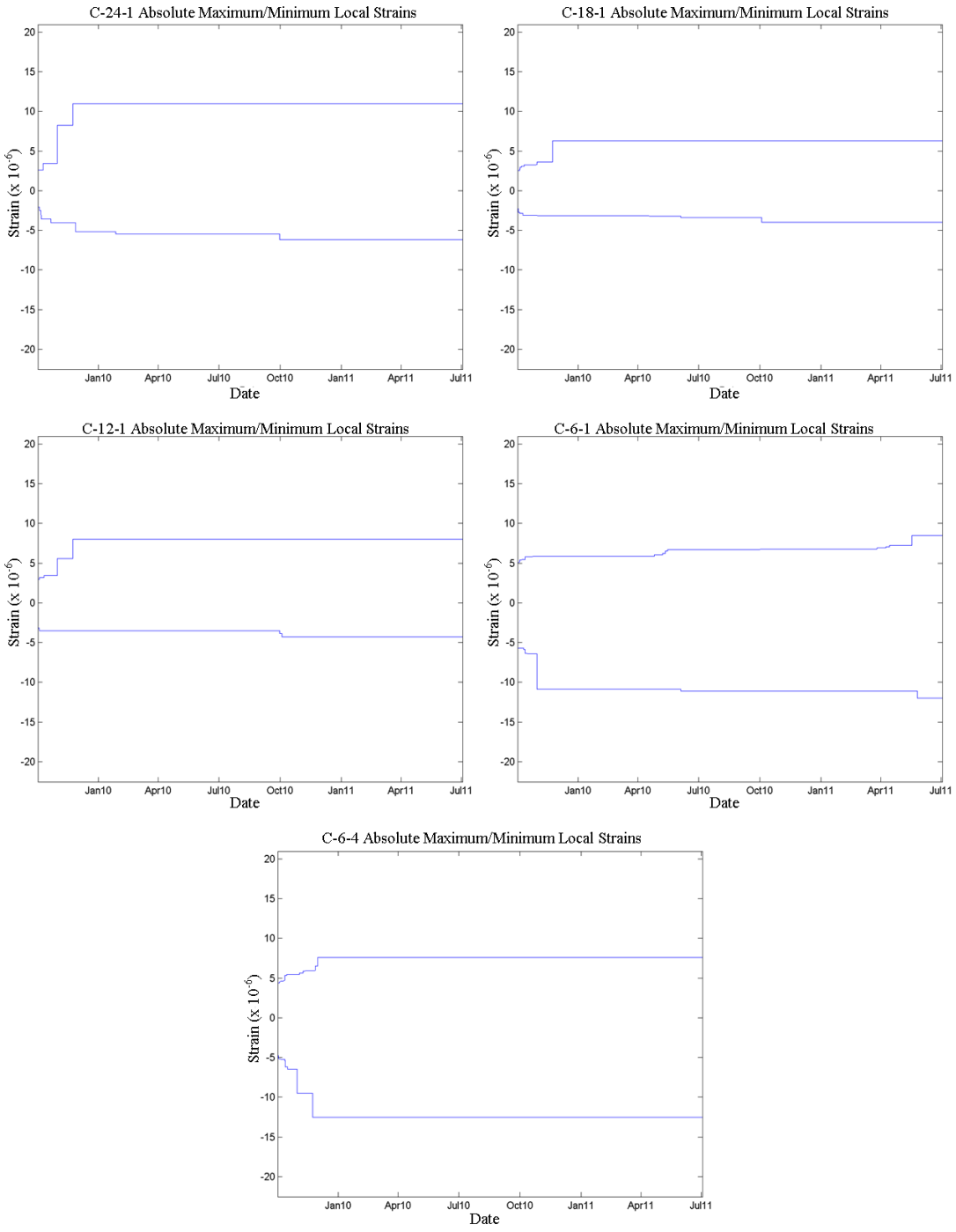

Figure C. 4. Absolute local maxima envelope versus recording date for sensors on stirrup C.

With the design-specified required minimum ultimate tensile strain of 0.0126, the first threshold value, T1, became 6,300 microstrain. Table C.2 lists the maximum global strain ε_{GM}, the maximum local strain ε_{LM}, the absolute strain, ε_{abs}, obtained using method 1 (see 4.2.4.4.1), as well as the normalized percentage of the absolute strain against T1 for each sensor on stirrup C. From Table C.2 it can be seen that the maximum absolute strain for all of the sensors on stirrup C only reaches 2.10% of T1. Therefore, the induced tensile strains on stirrup C were nowhere near the onset of tension rupture.

Table C. 2. The maximum global strains, maximum local strains, absolute strains, and the normalized percentage of the absolute strains against the threshold T1 for each sensor on stirrup C.

	T1 = 6300 x 10^{-6}			
	Maximum strains (10^{-6})			
Sensor	**Global (ε_{GM})**	**Local (ε_{LM})**	**Absolute (ε_{abs})**	**% of T1**
C-6-4	110	8	118	1.87
C-6-1	124	8	132	2.10
C-12-1	39	8	47	0.75
C-18-1	35	6	41	0.65
C-24-1	50	11	61	0.97

For the sensors on stirrup C, through both the individual assessment of each sensor as well as the comparison of the sensors not placed over the shrinkage crack to sensors C-6-1 and C-6-4, no debonding or peel has been observed. It has also been determined that the limit states of composite buckling and adhesive failure have not occurred. Finally, the absolute strain values did not come remotely close the T1 threshold value. Therefore, it can be concluded that stirrup C was in good working condition over the duration of the recorded data.

APPENDIX D. SECTION 5.5 SUPPLEMENT - STIRRUP D

D.1 FBG System Analysis and Results

For stirrup D, 683 or 1.79% of the total sensor datasets did not have a null wavelength established from the automated post-processing. The individual sensor breakdown of these values, their respective percentages, as well as the range of amplification values can be seen in Table D.1.

Table D. 1. Breakdown of the number and percentage of individual sensor datasets where a null wavelength value was not established for stirrup D, as well as the range of amplification factors required to processes the sets.

	No established null wavelength		Amplification range	
Sensor	Number of sets	%	β Min	β Max
D-6-4	162	2.12	1.4	2.0
D-6-1	387	5.06	1.4	1.8
D-12-1	101	1.32	1.4	1.8
D-18-1	18	0.24	1.6	2.4
D-24-1	15	0.20	1.6	2.4

As can be seen from Table D.1, the maximum amplification of the maximum variation between successive data points was 2.4. This maximum amplification was deemed insufficient to warrant an investigation into the individual datasets.

The null wavelength error plots for the sensors at stirrup D are presented in Figure D.1. From these plots it can be seen that no abnormally high value exists for all five of the sensors.

It can also be seen from Figure D.1 that the null wavelength errors for sensors D-24-1 and D-18-1 never exceeded the recording precision of the sensors (0.002 nm). Sensor D-12-1 had a typical upper bound error of 0.003 nm but rose to 0.004 nm twice. Sensors D-6-4 and D-6-1 had a typical upper bound of 0.004 nm, but the error did rise to 0.005 nm twice for D-6-1 and once for D-6-4.

Figure D.2 and Figure D.3 show the plots of the local maximum and minimum strains plotted against the date they were recorded for the sensors on stirrup D respectively. Through examining these plots it can be seen that maxima remained relatively constant or increased over time for all of the sensors. Therefore, FBG debonding has not occurred for any of the sensors on stirrup D.

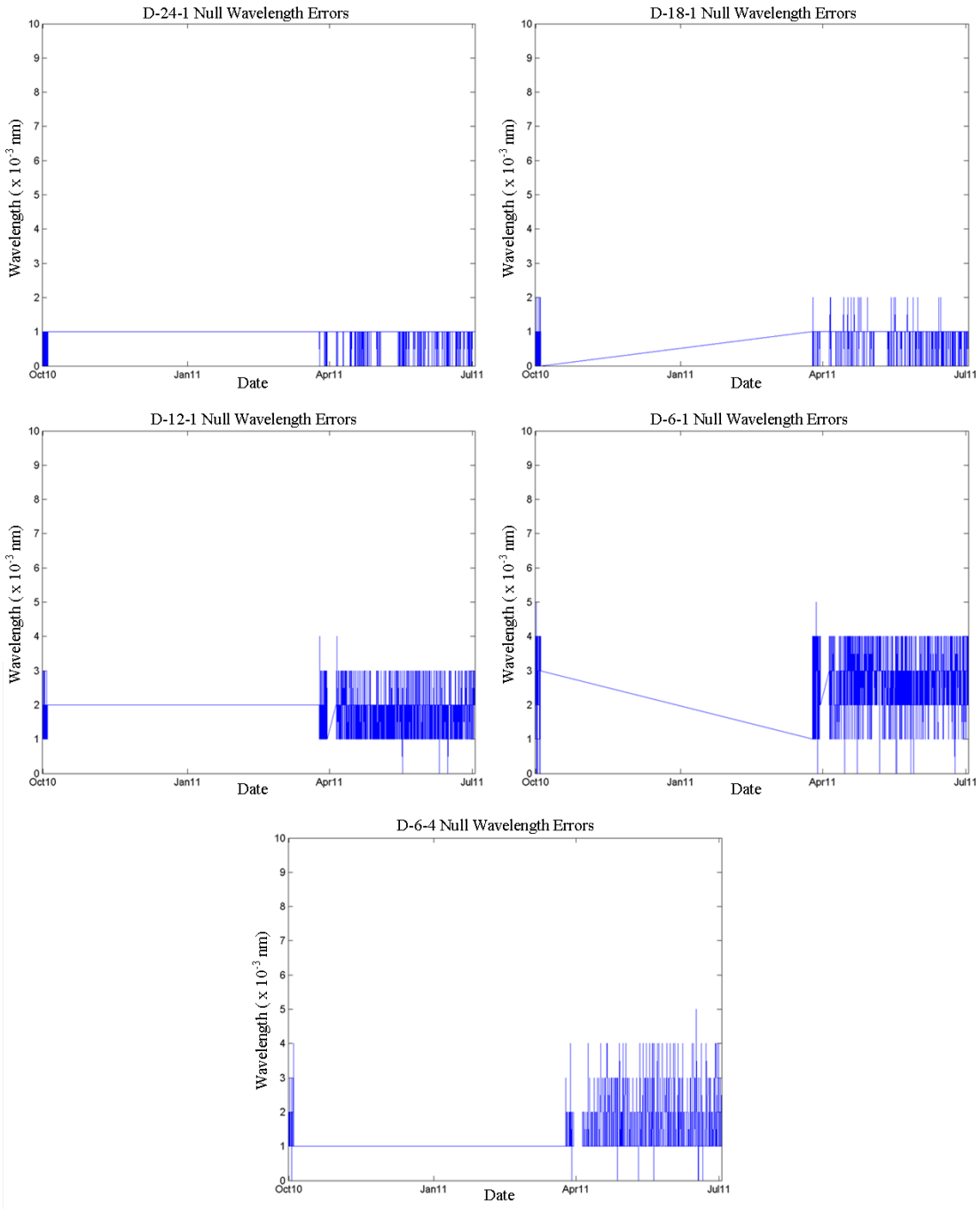

Figure D. 1. Null wavelength error versus the dates they were recorded for sensors on stirrup D.

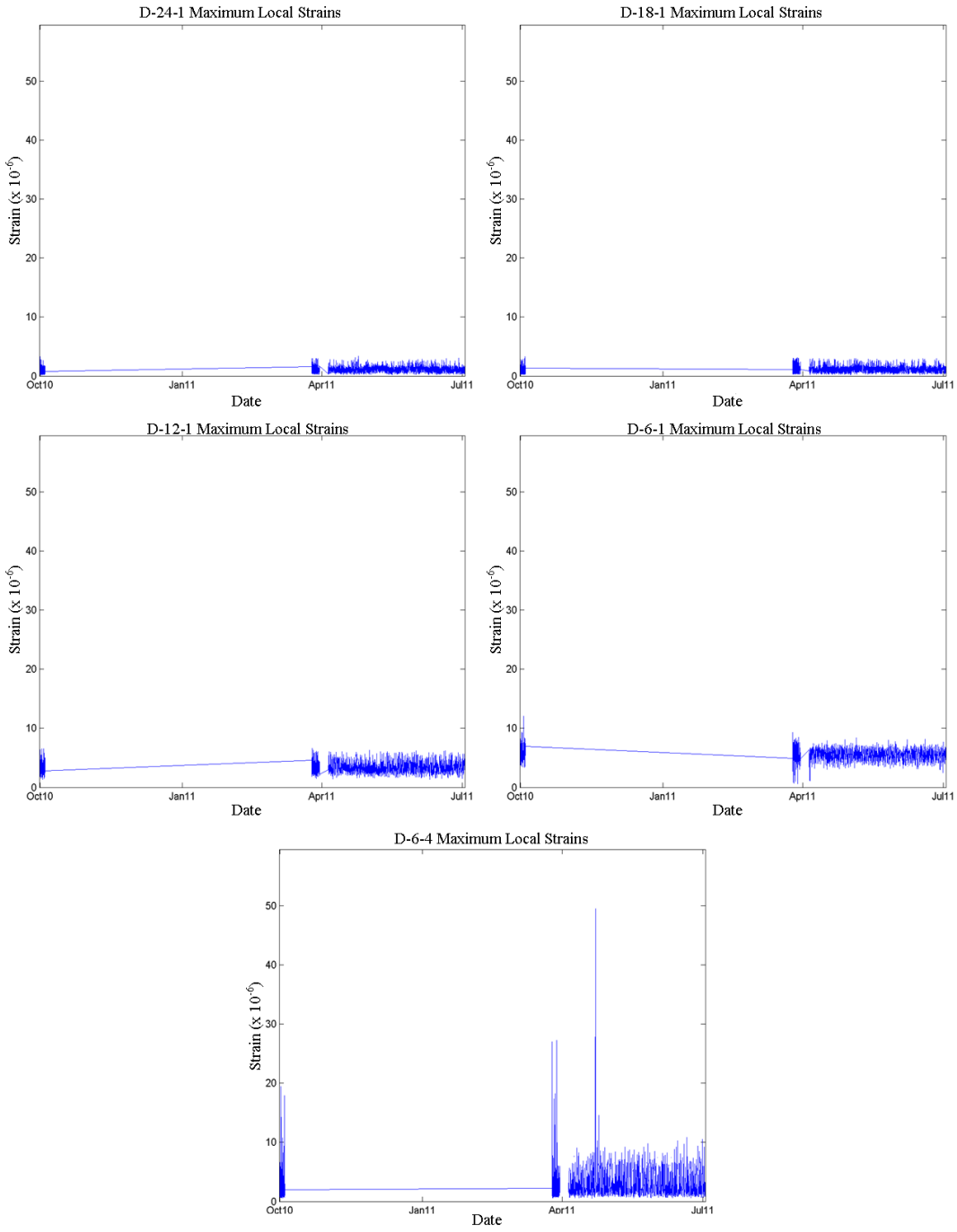

Figure D. 2. Maximum local strains versus the dates they were recorded for sensors at stirrup D.

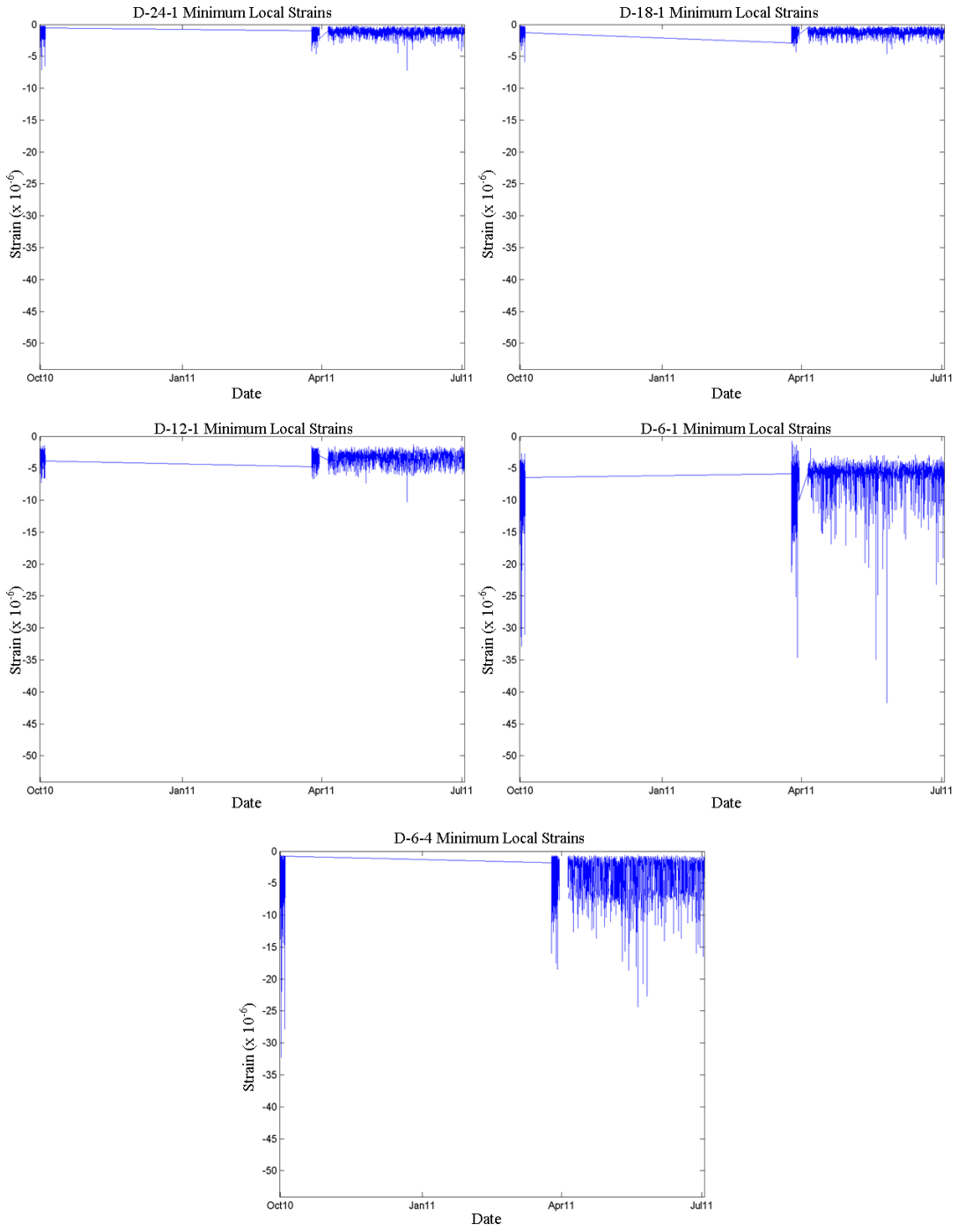

Figure D. 3. Minimum local strains versus the dates they were recorded for sensors at stirrup D.

Through the correction of the datasets with no null wavelength calculated from the initial post-processing and the assessment of abnormally high null wavelength values, the anomalies were corrected. Comparing the null wavelength errors against the precision of the sensors demonstrated that the null wavelength errors lie within a justifiable range. Checking for a decrease in maxima values demonstrated that the FBG sensors have not debonded. Therefore, it can be concluded that the FBG system on stirrup D was in good working order over the range of recorded data.

D.2 FRP Limit Analysis and Results

The envelope plots of the growth in the absolute local maximum and minimum strain values over the duration of data presented in this work for the sensors on stirrup D can be seen in Figure D.4. Sensors D-6-1 and D-6-4 were the sensors applied over the shrickage crack between the infill and bottom bulb of the girder. A quick observation of these graphs shows that the maxima for all of the sensors not placed over the shrinkage crack are constant, minus an increase of a few microstrain in the absolute local minimum strain of sensor D-12-1. Furthermore, the maximum range in local maximum and minimum strains for all of the sensors not associated with the shrinkage crack, sensor D-12-1, was only about 30% of sensor D-6-1. Therefore, it can be concluded that debonding or peel has not occurred for stirrup D.

The absolute minimum strains for D-6-1 and D-6-4 were significantly smaller in magnitude than the absolute minimum held by sensor A-6-1. Since sensor A-6-1 has not buckled, and it has been concluded that peel has not occurred for stirrup D, composite buckling is not considered to be a possible limit state for Stirrup D.

The continual activity of sensors D-6-1 and D-6-4 as seen through the local maximum and minimum plots in Figures D.3 and D.4, respectively, confirm that adhesive failure has not occurred for stirrup D.

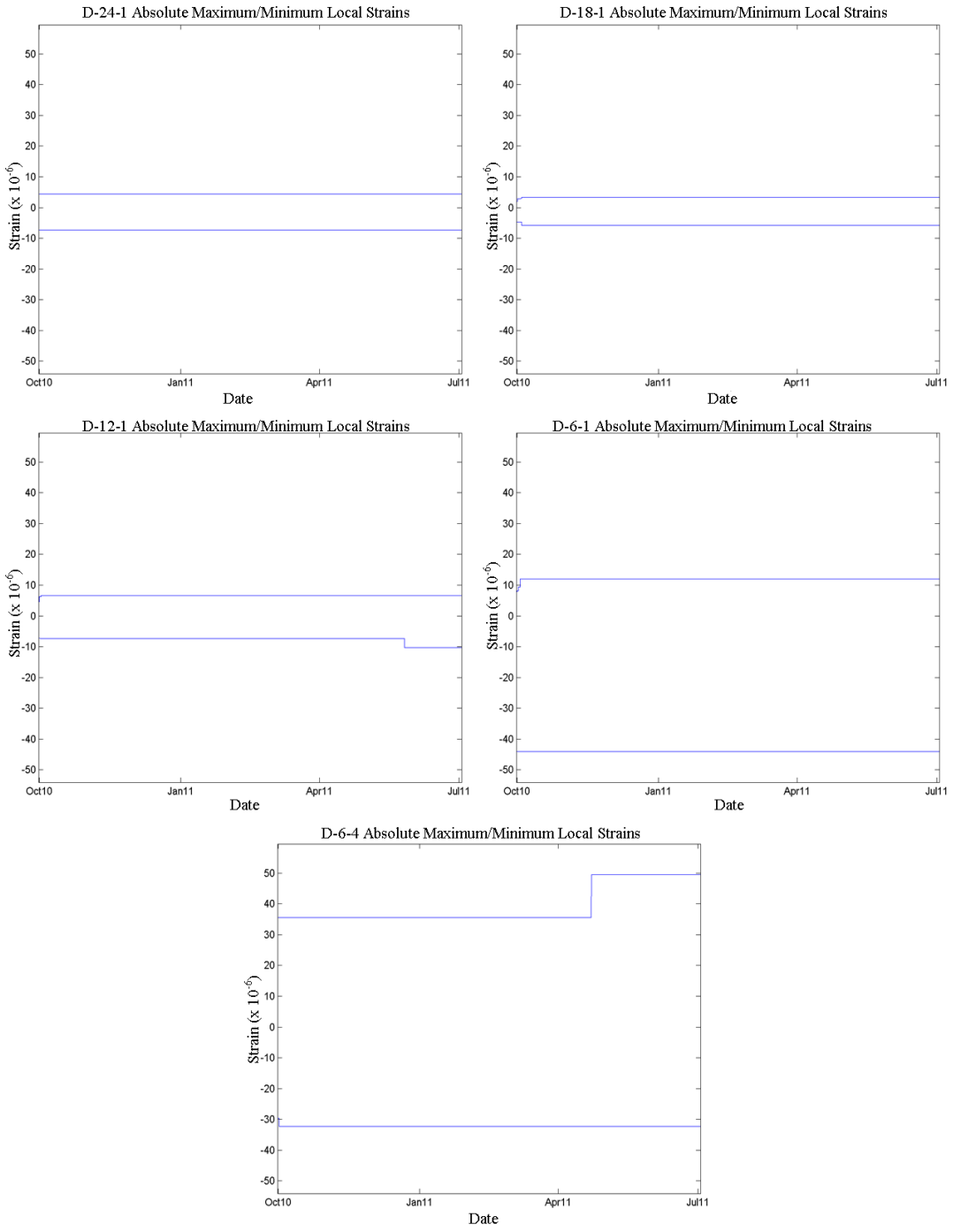

Figure D. 4. Absolute local maxima envelope versus recording date for sensors on stirrup D.

With the design-specified required minimum ultimate tensile strain of 0.0126, the first threshold value, T1, becomes 6,300 microstrain. Table D.2 lists the maximum global strain ε_{GM}, the maximum local strain ε_{LM}, the absolute strain, ε_{abs}, obtained using method 1 (see 4.2.4.4.1), as well as the normalized percentage of the absolute strain against T1 for each sensor on stirrup D. From Table D.2 it can be seen that the maximum absolute strain for all of the sensors on stirrup D only reaches 2.38% of T1. Therefore, the induced tensile strains on stirrup D are nowhere near the onset of tension rupture.

Table D. 2. The maximum global strains, maximum local strains, absolute strains, and the normalized percentage of the absolute strains against the threshold T1 for each sensor on stirrup D.

	T1 = 6300 x 10^{-6}			
	Maximum strains (10^{-6})			
Sensor	**Global (ε_{GM})**	**Local (ε_{LM})**	**Absolute (ε_{abs})**	**% of T1**
D-6-4	100	50	150	2.38
D-6-1	5	12	17	0.27
D-12-1	25	7	32	0.51
D-18-1	19	3	22	0.35
D-24-1	18	4	22	0.35

For the sensors on stirrup D, through both the individual assessment of each sensor as well as the comparison of the sensors not placed over the shrinkage crack to sensors D-6-1 and D-6-4, no debonding or peel has been observed. It has also been determined that the limit states of composite buckling and adhesive failure have not occurred. Finally, the absolute strain values did not come remotely close to the T1 threshold value. Therefore, it can be concluded that stirrup D was in good working condition over the duration of the recorded data.

APPENDIX E. SECTION 5.5 SUPPLEMENT - STIRRUP E

E.1 FBG System Analysis and Results

For stirrup E, 586 or 2.43% of the total sensor datasets did not have a null wavelength established from the automated post-processing. The individual sensor breakdown of these values, their respective percentages, as well as the range of amplification values can be seen in Table E.1.

Table E. 1. Breakdown of the number and percentage of individual sensor datasets where a null wavelength value was not established for stirrup E, as well as the range of amplification factors required to processes the sets.

	No established null wavelength		Amplification range	
Sensor	Number of sets	%	β Min	β Max
E-6-4	7	0.09	1.6	1.6
E-6-1	28	0.37	1.4	2.0
E-12-1	64	0.84	1.4	2.0
E-18-1	122	1.59	1.4	2.0
E-24-1	365	4.77	1.4	2.0

As can be seen from Table E.1, the maximum amplification of the maximum variation between successive data points was 2.0. This maximum amplification was deemed insufficient to warrant an investigation into the individual datasets.

The null wavelength error plots for the sensors on stirrup E are presented in Figure E.1. From these plots it can be seen that no abnormally high value existed for all five of the sensors.

It can also be seen from Figure E.1 that the null wavelength errors for sensors E-12-1, E-6-4, E-6-1, and E-18-1 never exceeded the recording precision of the sensors (0.002 nm), except on one occasion for E-6-1, and a handful of times for E-18-1 when the error for both rose to 0.003 nm. Sensor E-24-1 had a typical upper bound error of 0.004 nm.

Figure E.2 and Figure E.3 show the plots of the local maximum and minimum strains plotted against the date they were recorded for the sensors on stirrup E. Through examining these plots it can be seen that maxima remained relatively constant or increased over time for all of the sensors. Therefore, FBG debonding has not occurred for any of the sensors on stirrup E.

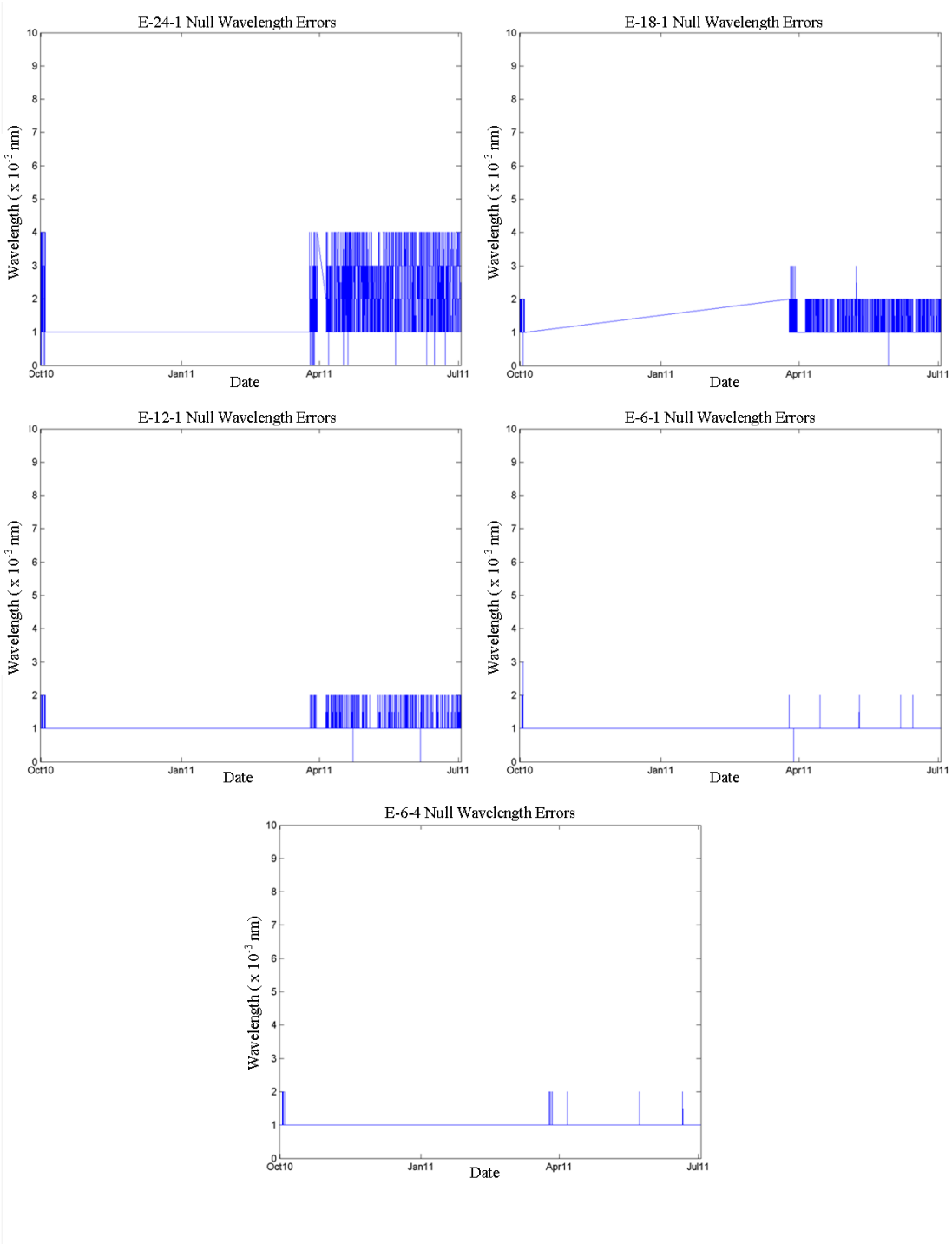

Figure E. 1. Null wavelength error versus the dates they were recorded for sensors on stirrup E.

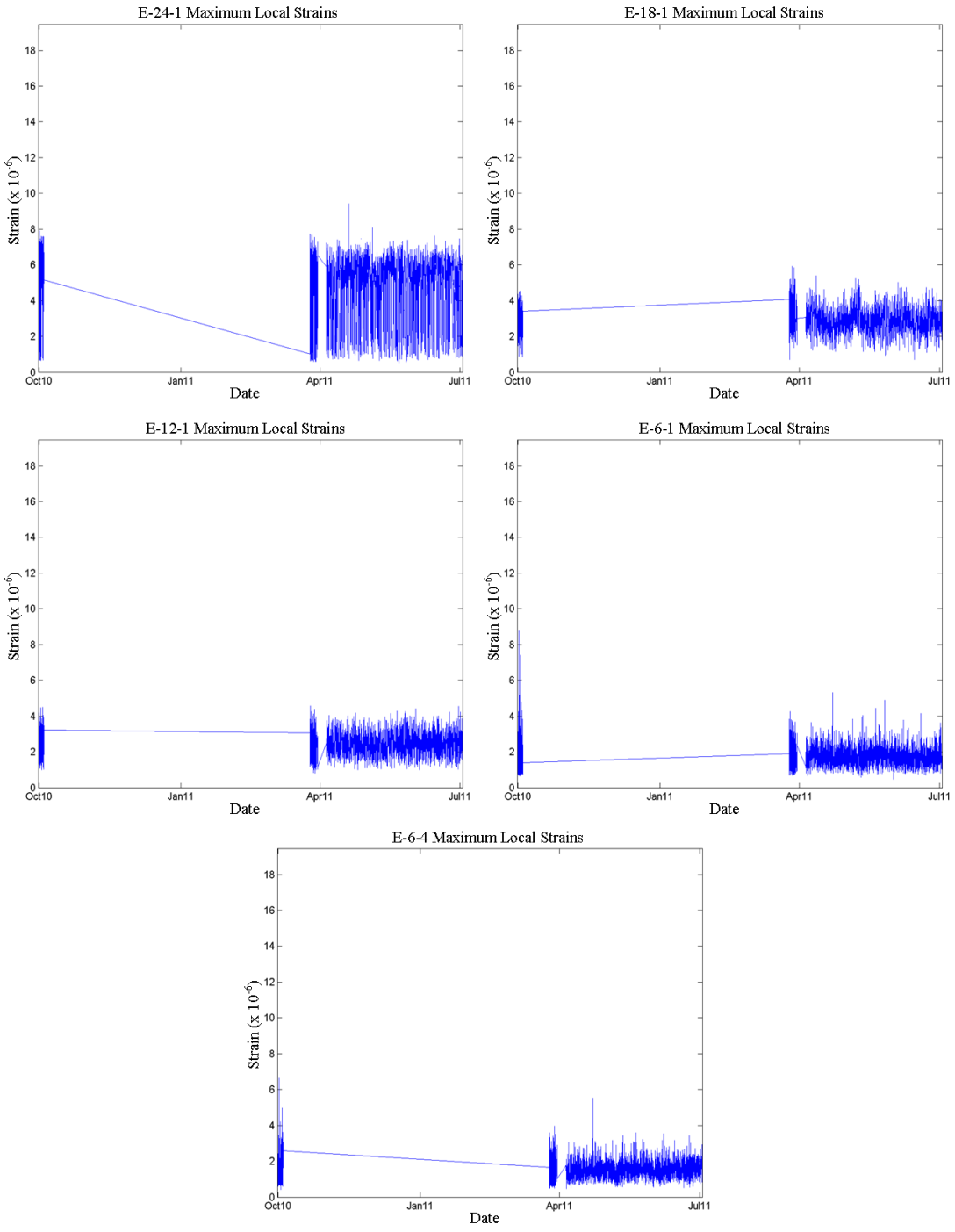

Figure E. 2. Maximum local strains versus the dates they were recorded for sensors at stirrup E.

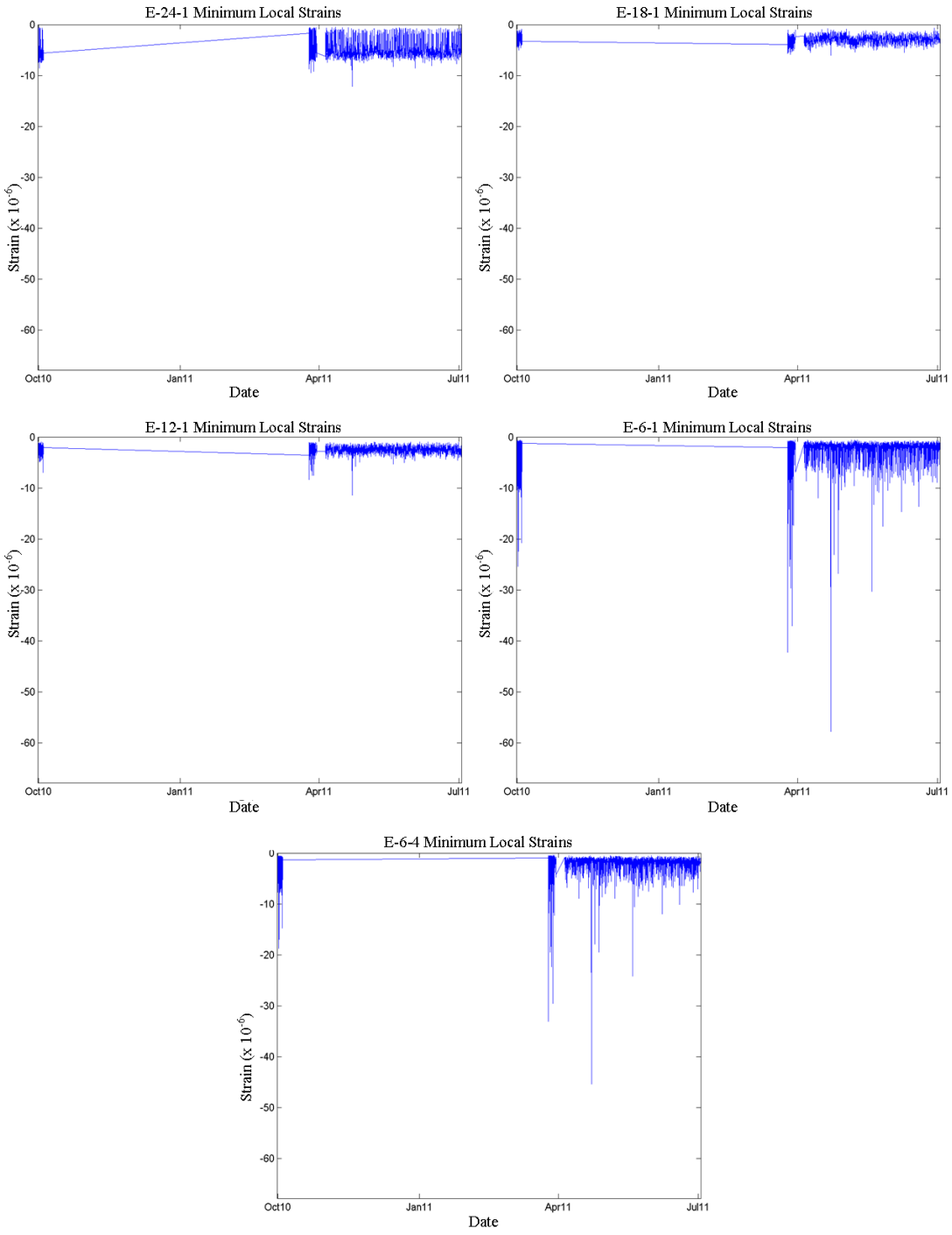

Figure E. 3. Minimum local strains versus the dates they were recorded for sensors at stirrup E.

Through the correction of the datasets with no null wavelength calculated from the initial post-processing and the assessment of abnormally high null wavelength values, the anomalies were corrected. Comparing the null wavelength errors against the precision of the sensors demonstrated that the null wavelength errors lie within a justifiable range. Checking for a decrease in maxima values demonstrated that the FBG sensors have not debonded. Therefore, it can be concluded that the FBG system on stirrup E was in good working order over the range of recorded data.

E.2 FRP Limit Analysis and Results

The envelope plots of the growth in the absolute local maximum and minimum strain values over the duration of data presented in this work for the sensors on stirrup E can be seen in Figure E.4. Sensors E-6-1 and E-6-4 were the sensors applied over the shrinkage crack between the infill and bottom bulb of the girder. A quick observation of these graphs shows that in the maxima for all of the sensors not located over the shrinkage crack recorded, only a slight increase of a few microstrain occurred in the absolute local minimum strain of sensor E-12-1, the absolute local maximum strain for sensor E-18-1, and both the local minimum and maximum for sensor E-24-1. Furthermore, the maximum range in local maximum and minimum strains for all of the sensors not located over the shrinkage crack, sensor E-24-1, is only about 35% of the minimum range of sensors E-6-1 and E-6-4. Therefore, it can be concluded that debonding or peel has not occurred for stirrup E.

The absolute minimum strains for E-6-1 and E-6-4 are significantly smaller in magnitude than the absolute minimum held by sensor A-6-1. Since sensor A-6-1 has not buckled, and it has been concluded that peel has not occurred for stirrup E, composite buckling is not considered to be a possible limit state for Stirrup E.

The continual activity of sensors E-6-1 and E-6-4, as seen through the local maximum and minimum plots in Figures E.3 and E.4, respectively, confirm that adhesive failure has not occurred for stirrup E.

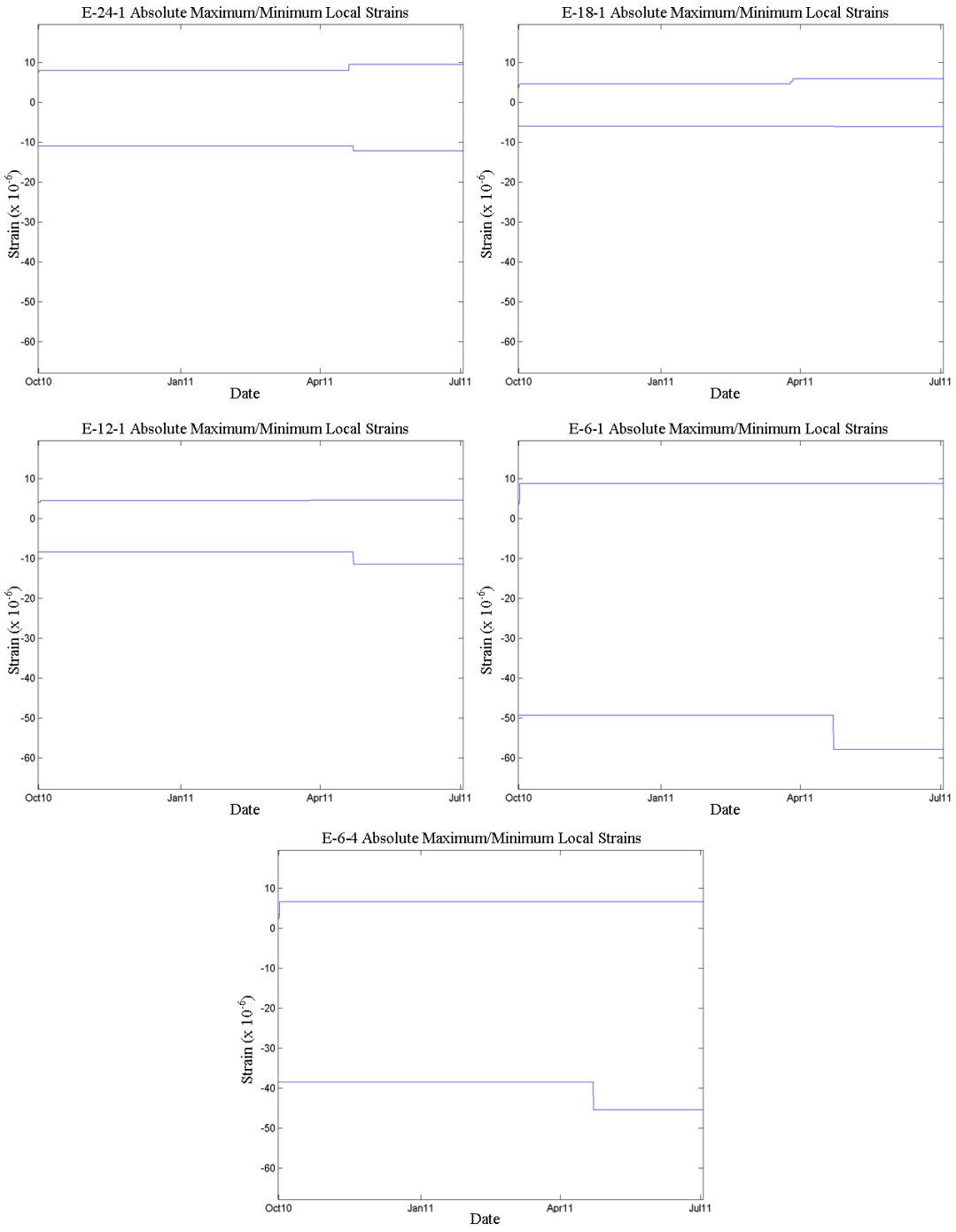

Figure E. 4. Absolute local maxima envelope versus recording date for sensors on stirrup E.

With the design-specified required minimum ultimate tensile strain of 0.0126, the first threshold value, T1, became 6,300 microstrain. Table E.2 lists the maximum global strain ε_{GM}, the maximum local strain ε_{LM}, the absolute strain, ε_{abs}, obtained using method 1 (see 4.2.4.4.1), as well as the normalized percentage of the absolute strain against T1 for each sensor on stirrup E. From Table E.2 it can be seen that the maximum absolute strain for all of the sensors on stirrup E only reached 0.54% of T1. Therefore, the induced tensile strains on stirrup E are nowhere near the onset of tension rupture.

Table E. 2. The maximum global strains, maximum local strains, absolute strains, and the normalized percentage of the absolute strains against the threshold T1 for each sensor on stirrup E.

	T1 = 6300 x 10^{-6}			
	Maximum strains (10^{-6})			
Sensor	**Global (ε_{GM})**	**Local (ε_{LM})**	**Absolute (ε_{abs})**	**% of T1**
E-6-4	27	7	34	0.54
E-6-1	20	9	29	0.46
E-12-1	27	4	31	0.49
E-18-1	23	6	29	0.46
E-24-1	19	9	28	0.44

For the sensors on stirrup E, through both the individual assessment of each sensor as well as the comparison of the sensors not positioned over the shrinkage crack to sensors E-6-1 and E-6-4, no debonding or peel has been observed. It has also been determined that the limit states of composite buckling and adhesive failure have not occurred. Finally, the absolute strain values did not come remotely close to the T1 threshold value. Therefore, it can be concluded that stirrup E was in good working condition over the duration of the recorded data.

APPENDIX F. SECTION 5.5 SUPPLEMENT - STIRRUP F

F.1 FGB System Analysis and Results

For stirrup F, 1,631 or 2.34% of the total sensor datasets did not have a null wavelength established from the automated post-processing. The individual sensor breakdown of these values, their respective percentages, as well as the range of amplification values can be seen in Table F.1.

Table F. 1. Breakdown of the number and percentage of individual sensor datasets where a null wavelength value was not established for stirrup F, as well as the range of amplification factors required to processes the sets.

	No established null wavelength		Amplification range	
Sensor	Number of sets	%	β Min	β Max
F-6-4	51	0.37	1.4	2.0
F-6-1	77	0.56	1.4	2.4
F-12-1	331	2.40	1.4	2.0
F-18-1	854	6.20	1.4	2.0
F-24-1	300	2.18	1.4	2.0

As can be seen from Table F.1, the maximum amplification of the maximum variation between successive data points was 2.4. This maximum amplification was deemed insufficient to warrant an investigation into the individual datasets.

The null wavelength error plots for the sensors at stirrup F are presented in Figure F.1. From these plots it can be seen that three abnormally high value exists from all five of the sensors. These error values were 0.006 nm for sensor F-18-1 recorded on May 17th, 2010 at 4:53 AM, 0.005 nm associated with sensor F-12-1 recorded on April 10th, 2011 at 9:28 PM, and sensor F-6-1 recorded on October 2nd, 2010 at 12:28 AM. Although the errors were higher than the norm, the values were too small to warrant an investigation into the local strain files.

It can also be seen from Figure F.1 that the null wavelength errors for sensor F-6-4 never exceeded the recording precision of the sensors (0.002 nm). Sensor F-6-1's errors only exceed the sensors precision on a few occasions. For sensors F-24-1 and F-12-1, the upper bound of the null wavelength error was typically 0.003 nm. The typical upper bound for sensor F-18-1 was 0.004 nm, although it did rise to 0.005 nm occasionally as well as once to 0.006 nm.

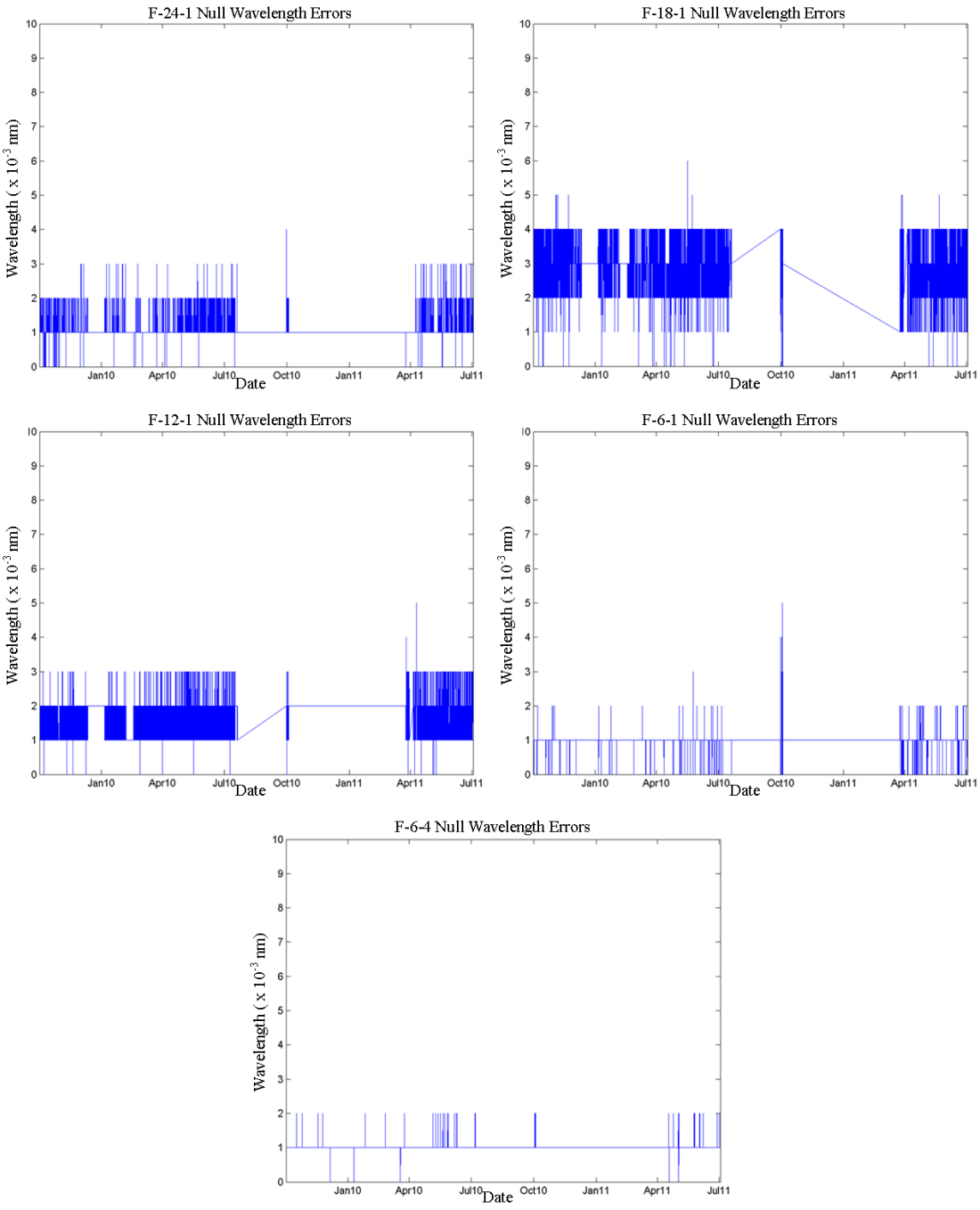

Figure F. 1. Null wavelength error versus the dates they were recorded for sensors on stirrup F.

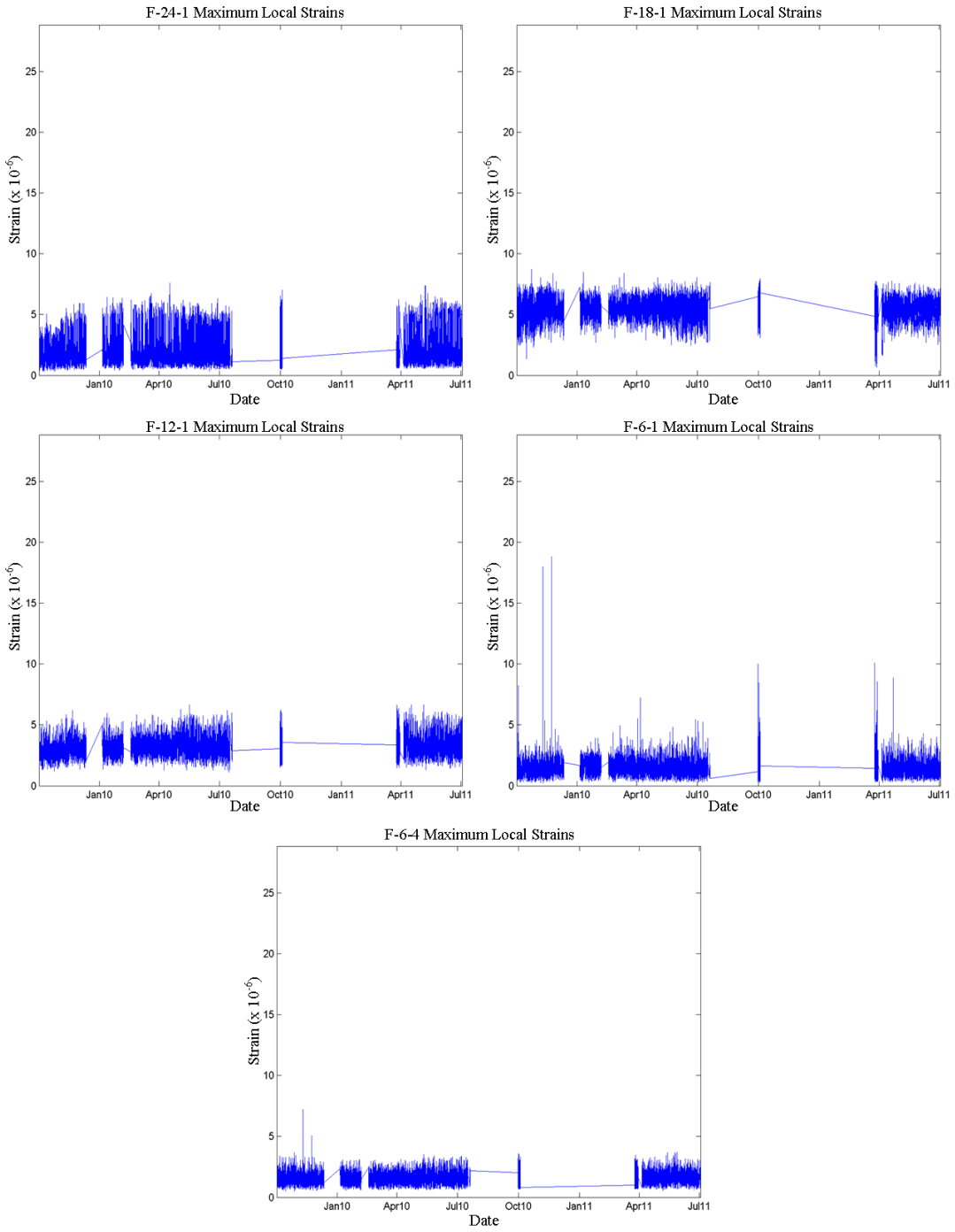

Figure F. 2. Maximum local strains versus the dates they were recorded for sensors at stirrup F.

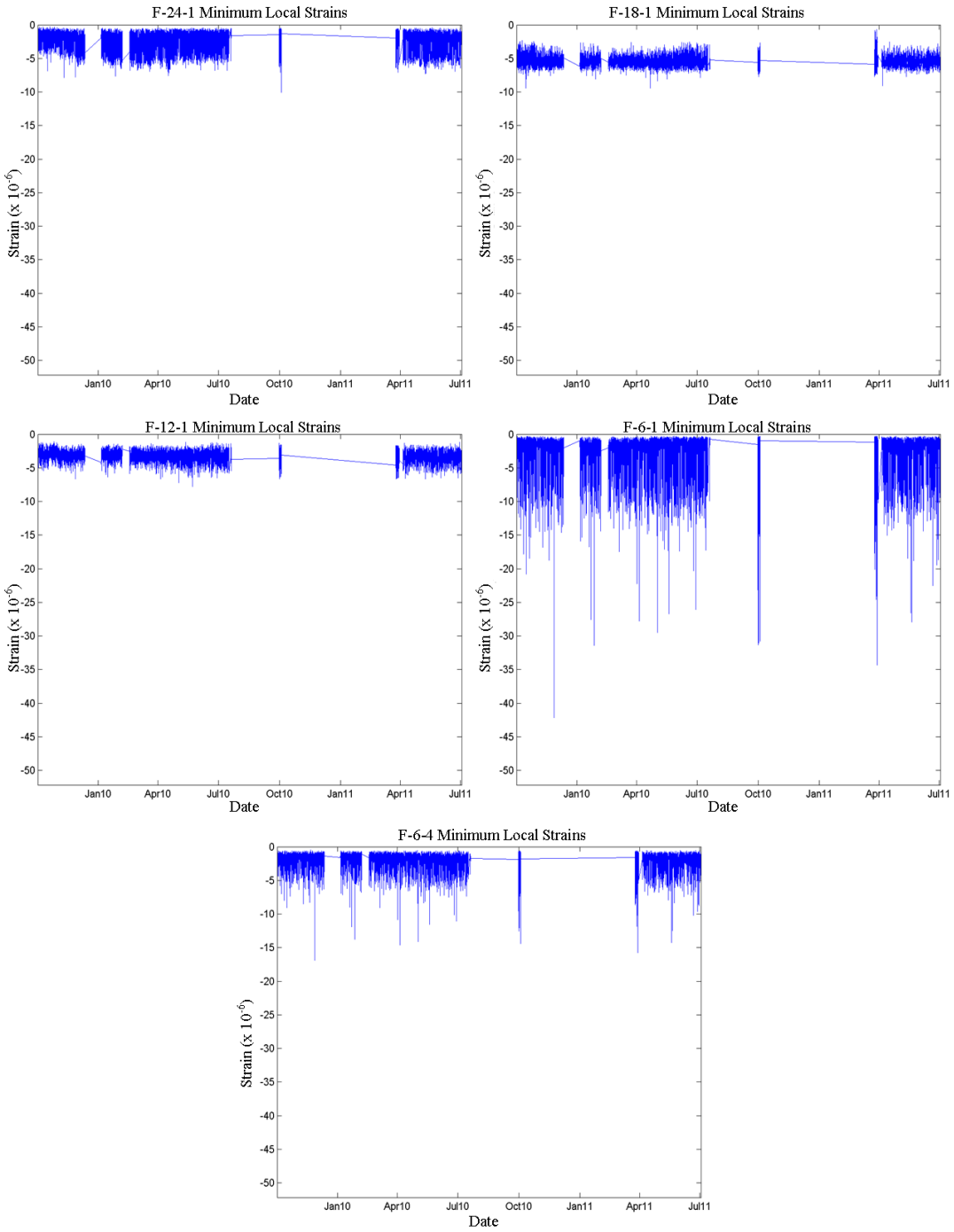

Figure F. 3. Minimum local strains versus the dates they were recorded for sensors at stirrup F.

Figure F.2 and Figure F.3 show the plots of the local maximum and minimum strains plotted against the date they were recorded for the sensors on stirrup F. Through examining these plots, it can be seen that maxima remained relatively constant, or increased over time for all of the sensors. Therefore, FBG debonding has not occurred for any of the sensors on stirrup F.

Through the correction of the datasets with no null wavelength calculated from the initial post-processing and the assessment of abnormally high null wavelength values, the anomalies were corrected. Comparing the null wavelength errors against the precision of the sensors demonstrated that the null wavelength errors lie within a justifiable range. Checking for a decrease in maxima values demonstrated that the FBG sensors have not debonded. Therefore, it can be concluded that the FBG system on stirrup F was in good working order over the range of recorded data.

F.2 FRP Limit Analysis and Results

The envelope plots of the growth in the absolute local maximum and minimum strains values over the duration of data presented in this work for the sensors on stirrup F can be seen in Figure F.4. Sensors F-6-1 and F-6-4 were the sensors applied over the shrinkage crack between the infill and bottom bulb of the girder. A quick observation of these graphs shows that by 2010 the maxima for the sensors F-18-1, F-6-1, and F-6-4 became constant. Sensors F-24-1 and F-12-1 continued to increase for several more months before reaching constant values, but these increases were only by a few microstrain. Also, the behavior of sensor F-6-4 more resembles a sensor not applied ovr the shrinkage crack. Furthermore, by comparing the sensors not associated with the shrinkage crack to sensor F-6-1, it can be seen that the maxima strains of was only about 30% of F-6-1. Therefore, it can be concluded that debonding or peel has not occurred for stirrup F.

The absolute minimum strains for F-6-1 and F-6-4 are significantly smaller in magnitude than the absolute minimum held by sensor A-6-1. Since sensor A-6-1 has not buckled, and it has been concluded that peel has not occurred for stirrup F, composite buckling is not considered to be a possible limit state over the course of the recorded data.

The continual activity of sensors F-6-1 and F-6-4 as seen through the local maximum and minimum plots in Figures F.3 and F.4, respectively, confirm that adhesive failure has not occurred for stirrup F.

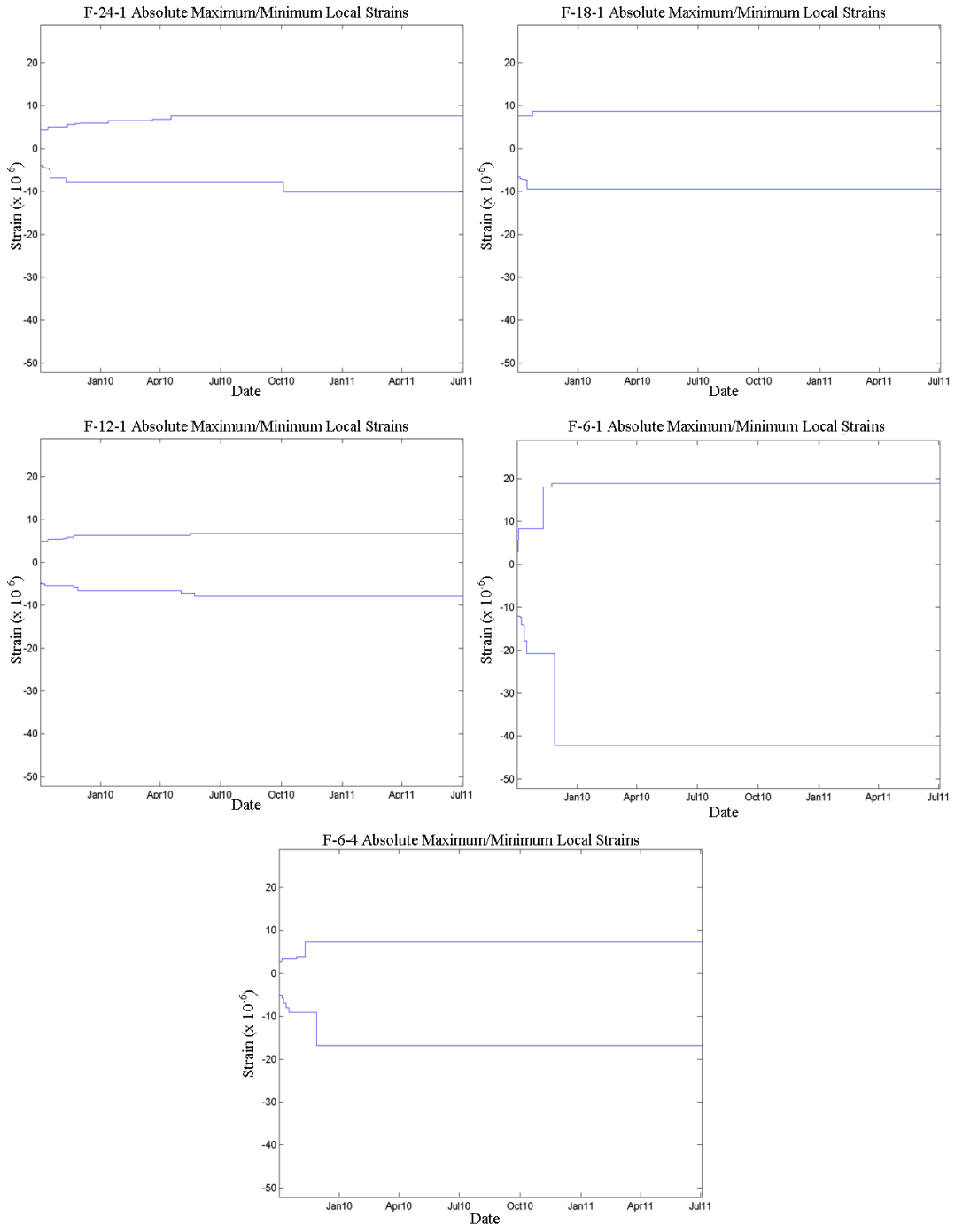

Figure F. 4. Absolute local maxima envelope versus recording date for sensors on stirrup F.

With the design-specified required minimum ultimate tensile strain of 0.0126, the first threshold value, T1, became 6,300 microstrain. Table F.2 lists the maximum global strain ε_{GM}, the maximum local strain ε_{LM}, the absolute strain, ε_{abs}, obtained using method 1 (see 4.2.4.4.1), as well as the normalized percentage of the absolute strain against T1 for each sensor on stirrup F. From Table F.2 it can be seen that the maximum absolute strain for all of the sensors on stirrup F only reaches 0.54% of T1. Therefore, the induced tensile strains on stirrup F are nowhere near the onset of tension rupture.

Table F. 2. The maximum global strains, maximum local strains, absolute strains, and the normalized percentage of the absolute strains against the threshold T1 for each sensor on stirrup F.

	T1 = 6300 x 10^{-6}			
	Maximum strains (10^{-6})			
Sensor	**Global (ε_{GM})**	**Local (ε_{LM})**	**Absolute (ε_{abs})**	**% of T1**
F-6-4	30	7	37	0.59
F-6-1	55	19	74	1.17
F-12-1	47	7	54	0.86
F-18-1	34	9	43	0.68
F-24-1	43	8	51	0.81

For the sensors on stirrup F, through both the individual assessment of each sensor as well as the comparison of the sensors not associated with the shrinkage crack to sensor F-6-1, no debonding or peel has been observed. It has also been determined that the limit states of composite buckling and adhesive failure have not occurred. Finally, the absolute strain values did not come remotely close to the T1 threshold value. Therefore, it can be concluded that stirrup F was in good working condition over the duration of the recorded data.

APPENDIX G. GLOBAL STRAIN GRAPHS

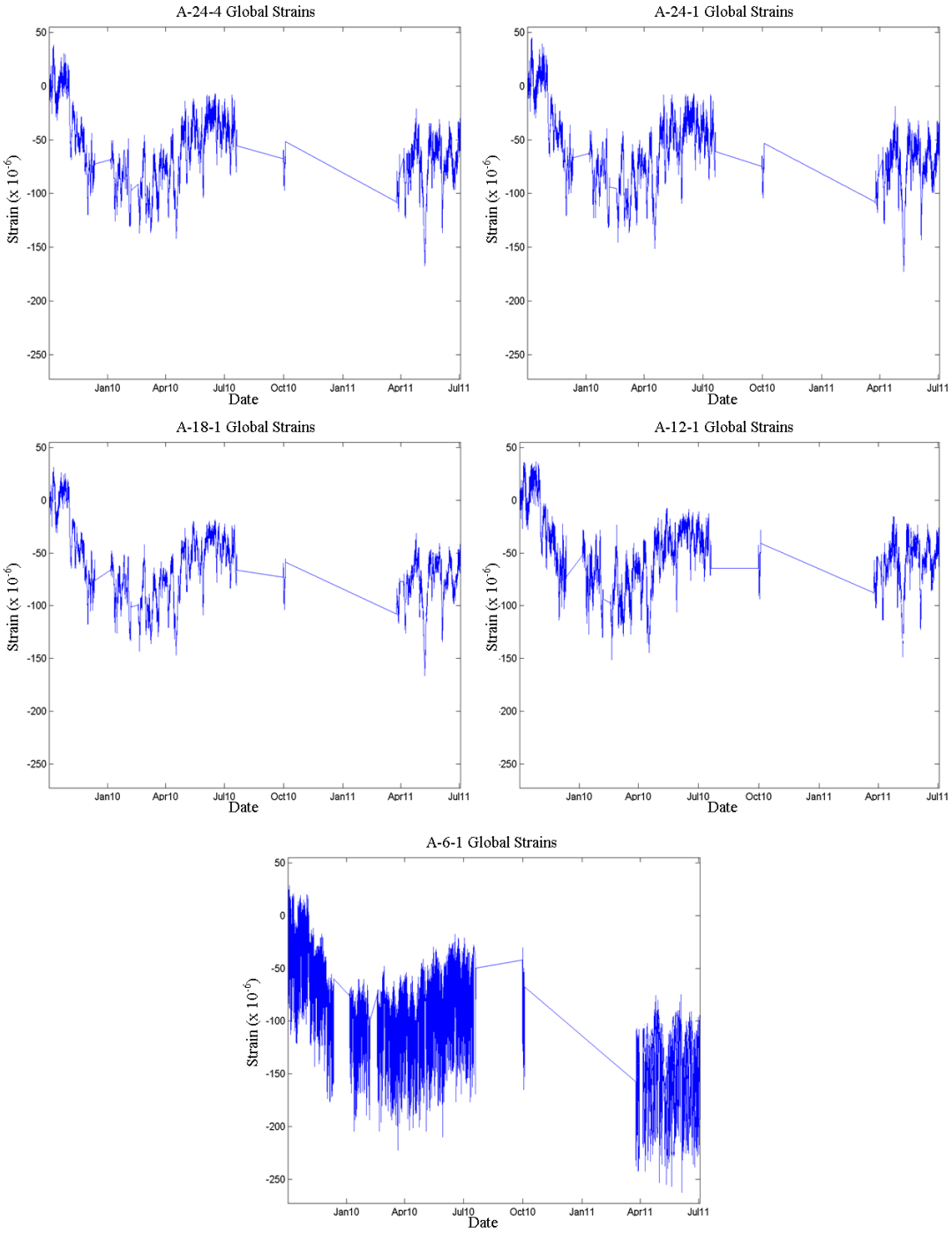

Figure G. 1. Global strain plots for the sensors on stirrup A.

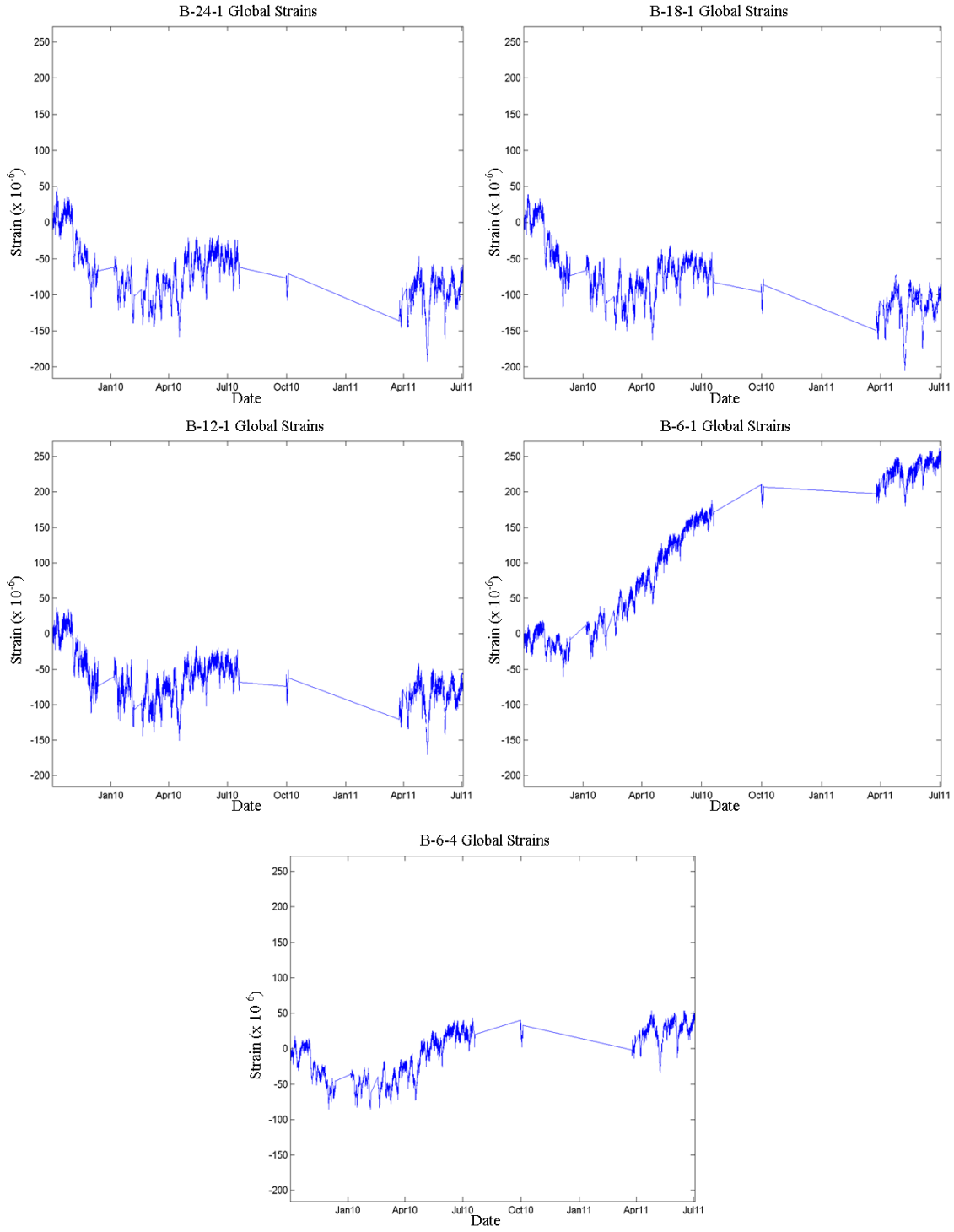

Figure G. 2. Global strain plots for the sensors on stirrup B.

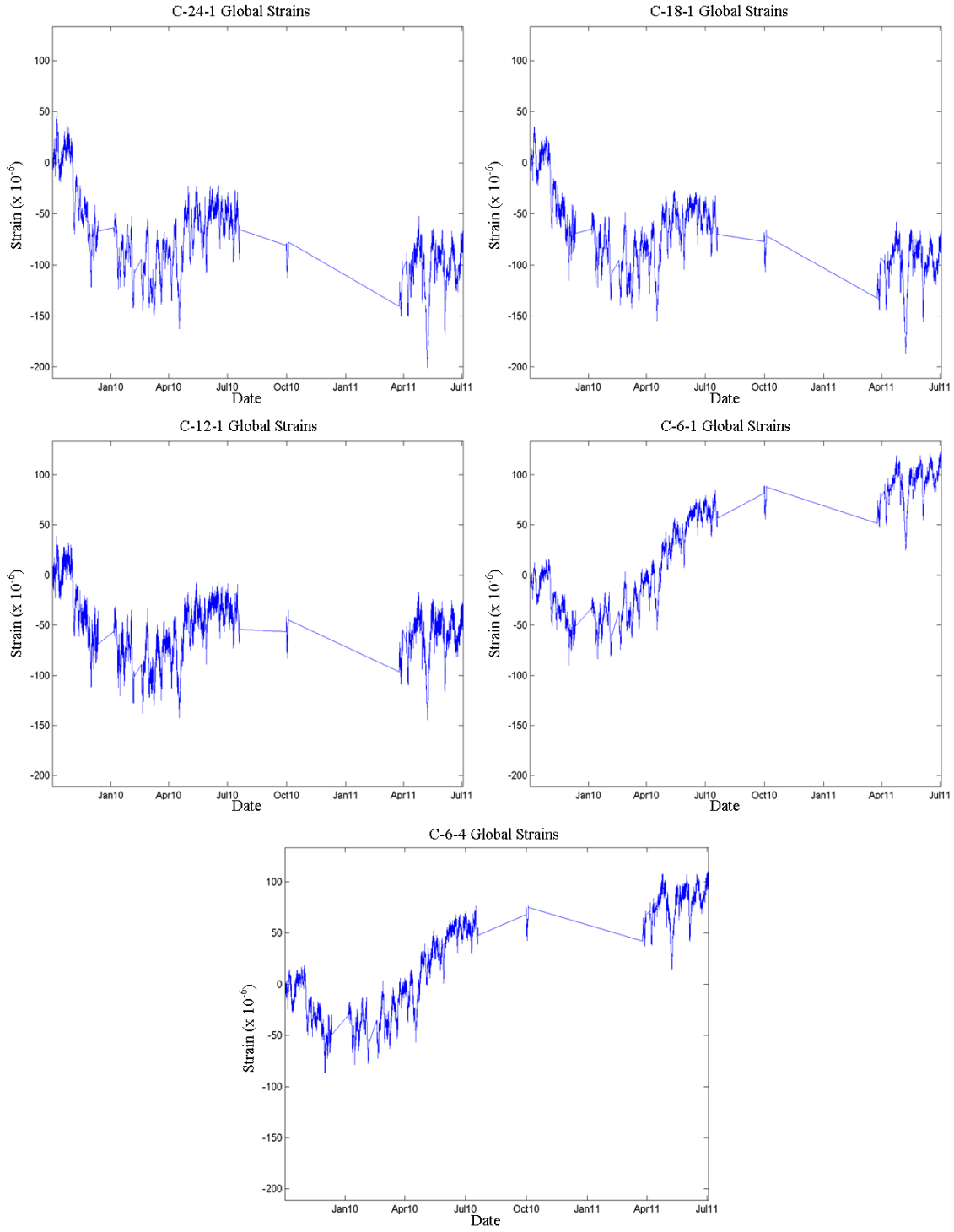

Figure G. 3. Global strain plots for the sensors on stirrup C.

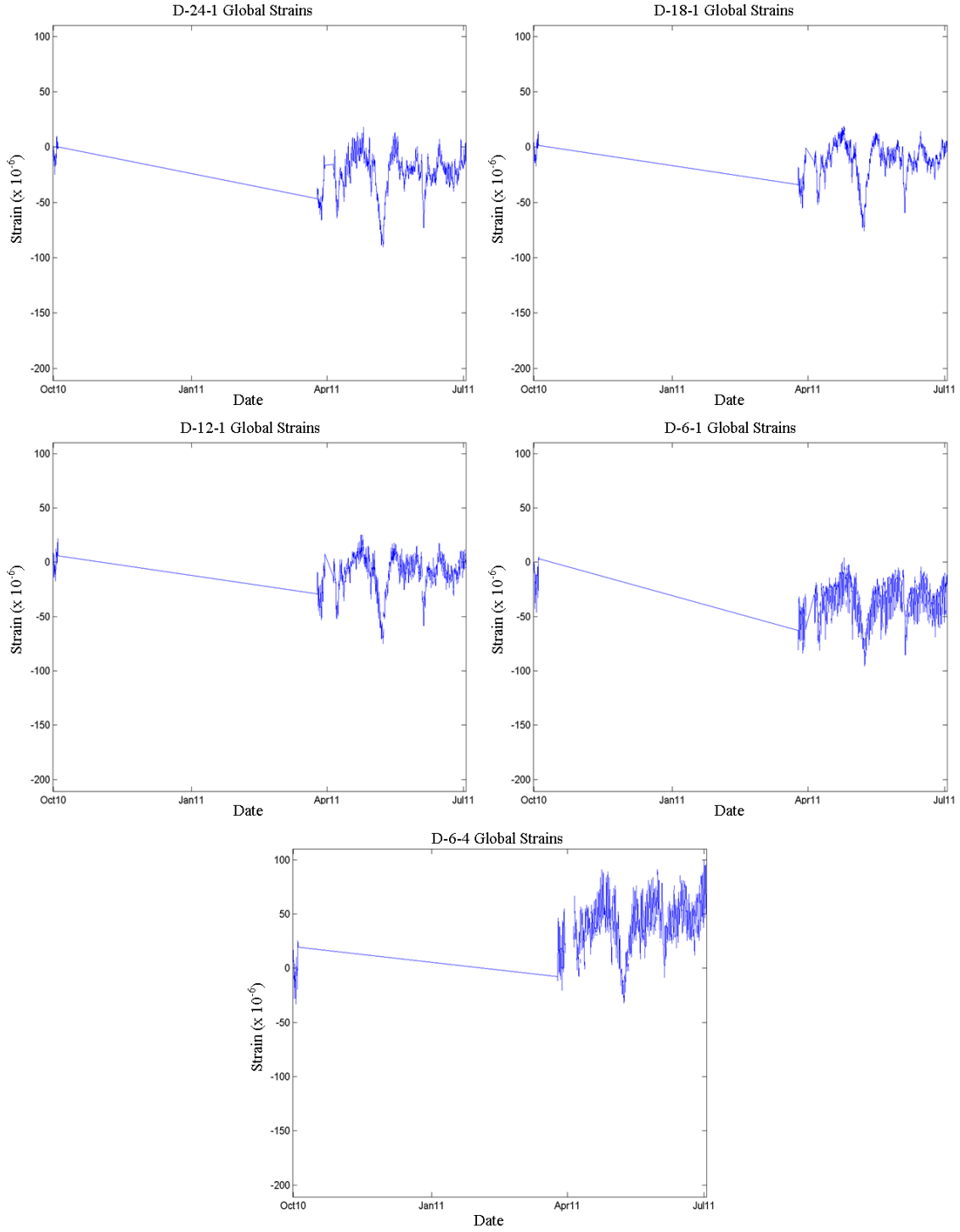

Figure G. 4. Global strain plots for the sensors on stirrup D.

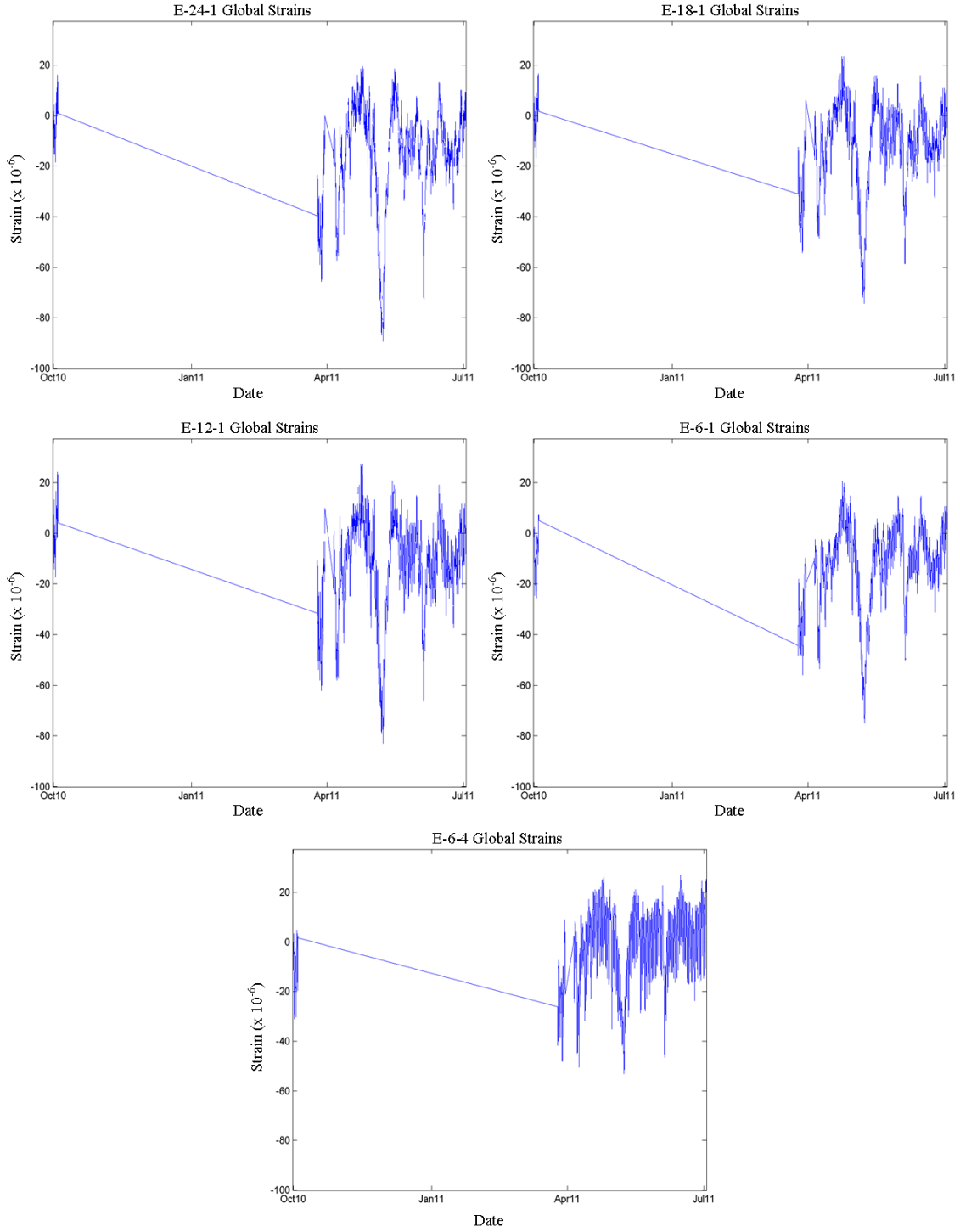

Figure G. 5. Global strain plots for the sensors on stirrup E.

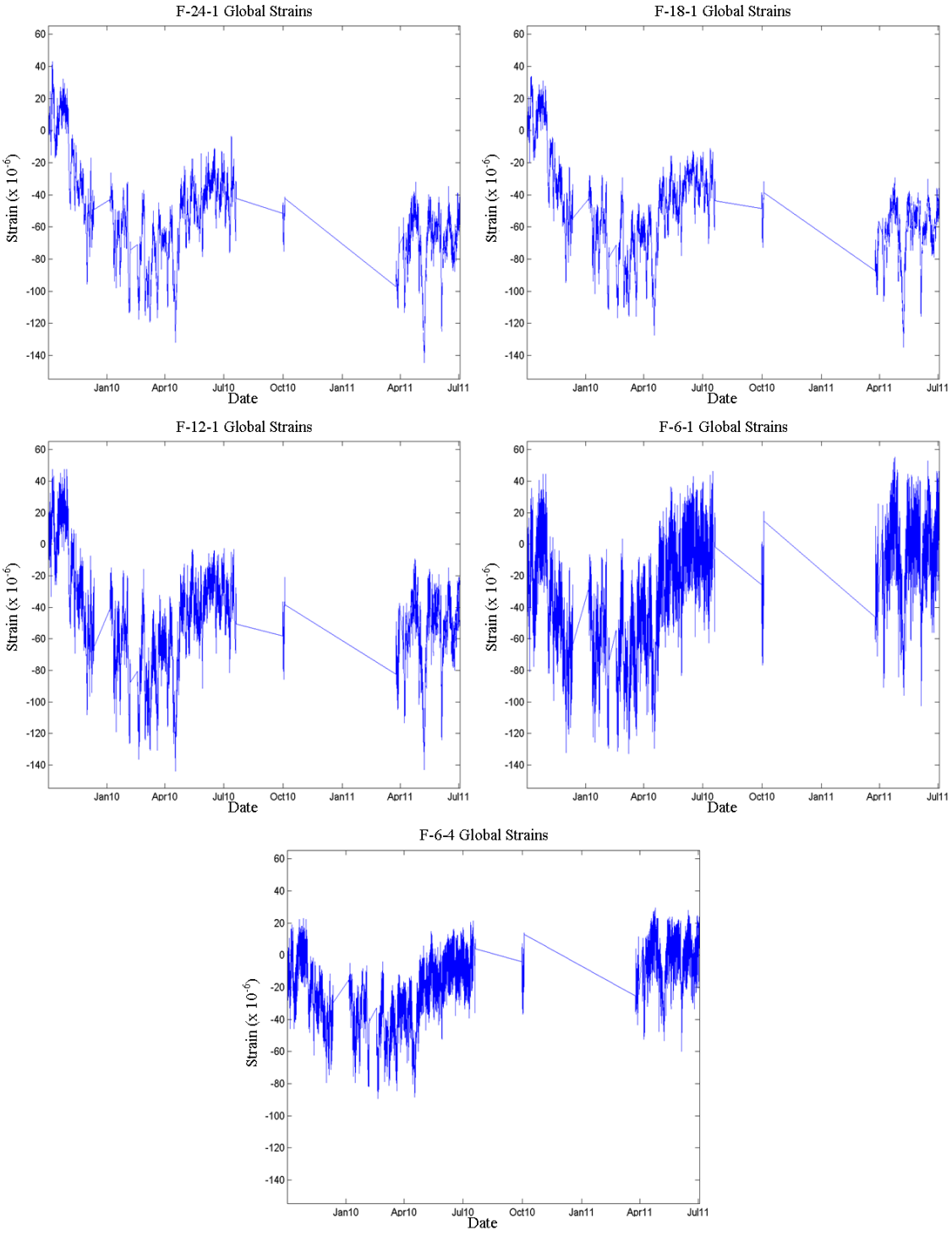

Figure G. 6. Global strain plots for the sensors on stirrup F.

REFERENCES

[1] H.-N. Li, D.-S. Li, and G.-B. Song, "Recent applications of fiber optic sensors to health monitoring in civil engineering," *Engineering Structures*, vol. 26, no. 11, pp. 1647-1657, Sep. 2004.

[2] W. L. Schulz, J. P. Conte, E. Udd, and J. M. Seim, "Static and dynamic testing of bridges and highways using long-gage fiber Bragg grating based strain sensors," in *Proceedings of SPIE*, 2000, vol. 4202, pp. 79-86.

[3] M. A. Issa, H. I. Shabila, and M. Alhassan, "STRUCTURAL HEALTH MONITORING SYSTEMS FOR BRIDGE DECKS AND REHABILITATED PRECAST PRESTRESSED CONCRETE BEAMS," in *Sensing Issues in Civil Structural Health Monitoring*, F. Ansari, Ed. Dordrecth, The Netherlands: Springer, 2005, pp. 363-372.

[4] P. Labossière, P. Rochette, K. W. Neal, and M. Demers, "FRP-STRENGTHENED STRUCTURES: MONITORING ISSUES FROM QUÉBEC APPLICATIONS," in *Sensing Issues in Civil Structural Health Monitoring*, F. Ansari, Ed. Dordrecth, The Netherlands: Springer, 2005, pp. 117-126.

[5] B. Torres, I. Payá-Zaforteza, P. A. Calderón, and J. M. Adam, "Analysis of the strain transfer in a new FBG sensor for Structural Health Monitoring," *Engineering Structures*, vol. 33, no. 2, pp. 539-548, Feb. 2011.

[6] C. Rodrigues, C. Félix, A. Lage, and J. Figueiras, "Development of a long-term monitoring system based on FBG sensors applied to concrete bridges," *Engineering Structures*, vol. 32, no. 8, pp. 1993-2002, Aug. 2010.

[7] B. Glišić and D. Inaudi, *Fiber Optic Methods for Structural Health Monitoring*. Chichester, England: John Wiley & Sons Ltd., 2007.

[8] J. R. Casas and P. J. S. Cruz, "Fiber Optic Sensors for Bridge Monitoring," *Journal of Bridge Engineering*, vol. 8, no. 6, p. 362, 2003.

[9] M. Majumder, T. K. Gangopadhyay, A. K. Chakraborty, K. Dasgupta, and D. K. Bhattacharya, "Fibre Bragg gratings in structural health monitoring—Present status and applications," *Sensors and Actuators A: Physical*, vol. 147, no. 1, pp. 150-164, Sep. 2008.

[10] A. Belarbi, A. Ayoub, D. Kuchma, A. Mirmiran, and A. Okeil, "NCHRP REPORT 678 - Design of FRP Systems for Strengthening Concrete Girders in Shear," National Academy of Sciences, Washington, DC, 2011.

[11] Y. T. Obaidat, S. Heyden, O. Dahlblom, G. Abu-Farsakh, and Y. Abdel-Jawad, "Retrofitting of reinforced concrete beams using composite laminates," *Construction and Building Materials*, vol. 25, no. 2, pp. 591-597, Feb. 2011.

[12] B. A. Sundaram, K. Kesavan, S. Parivallal, A. K. F. Ahmed, and K. Ravisankar, "Monitoring of FRP Strengthened Concrete Structures Using FBG Sensors," *Procedia Engineering*, vol. 14, pp. 1549-1556, Jan. 2011.

[13] U. S. Camli and B. Binici, "Strength of carbon fiber reinforced polymers bonded to concrete and masonry," *Construction and Building Materials*, vol. 21, no. 7, pp. 1431-1446, Jul. 2007.

[14] A. A. Mufti, "FRPs and FOSs lead to innovation in Canadian civil engineering structures," *Construction and Building Materials*, vol. 17, no. 6-7, pp. 379-387, Sep. 2003.

[15] V. M. Karbhari, "HEALTH MONITORING, DAMAGE PROGNOSIS AND SERVICE-LIFE PREDICTION - ISSUES RELATED TO IMPLEMENTATION," in *Sensing Issues in Civil Structural Health Monitoring*, F. Ansari, Ed. Dordrecth, The Netherlands: Springer, 2005, pp. 301-310.

[16] V. E. Saouma, D. Z. Anderson, K. Ostrander, B. Lee, and V. Slowik, "Application of fiber Bragg grating in local and remote infrastructure health monitoring," *Materials and Structures*, vol. 31, no. 4, pp. 259-266, May 1998.

[17] R. Maaskant, T. Alavie, R. M. Measures, G. Tadros, S. H. Rizkalla, and A. Guha-Thakurta, "Fiber-optic Bragg grating sensors for bridge monitoring," *Cement and Concrete Composites*, vol. 19, no. 1, pp. 21-33, Jan. 1997.

[18] C. Schizas, S. Stutz, J. Botsis, and D. Coric, "Monitoring of non-homogeneous strains in composites with embedded wavelength multiplexed fiber Bragg gratings: A methodological study," *Composite Structures*, vol. 94, no. 3, pp. 987-994, Feb. 2012.

[19] Y. M. Gebremichael, W. Li, W. J. O. Boyle, B. T. Meggitt, K. T. V. Grattan, B. McKinley, G. F. Fernando, G. Kister, D. Winter, L. Canning, and S. Luke, "Integration and assessment of fibre Bragg grating sensors in an all-fibre reinforced polymer composite road bridge," *Sensors and Actuators A: Physical*, vol. 118, no. 1, pp. 78-85, Jan. 2005.

[20] G. Kister, D. Winter, R. A. Badcock, Y. M. Gebremichael, W. J. O. Boyle, B. T. Meggitt, K. T. V. Grattan, and G. F. Fernando, "Structural health monitoring of a composite bridge using Bragg grating sensors. Part 1: Evaluation of adhesives and protection systems for the optical sensors," *Engineering Structures*, vol. 29, no. 3, pp. 440-448, Mar. 2007.

[21] L. C. Hollaway, "A review of the present and future utilisation of FRP composites in the civil infrastructure with reference to their important in-service properties," *Construction and Building Materials*, vol. 24, no. 12, pp. 2419-2445, Dec. 2010.

[22] AASHTO, *AASHTO LRFD Bridge Design Specifications*, 4th ed. Washington, DC: .

[23] G. Hackmann, F. Sun, N. Castaneda, C. Lu, and S. Dyke, "A holistic approach to decentralized structural damage localization using wireless sensor networks," *Computer Communications*, Jan. 2012.

[24] X. Zhang, D. Liang, J. Zeng, and A. Asundi, "Genetic algorithm-support vector regression for high reliability SHM system based on FBG sensor network," *Optics and Lasers in Engineering*, vol. 50, no. 2, pp. 148-153, Feb. 2012.

[25] M. A. Prada, J. Toivola, J. Kullaa, and J. Hollmén, “Three-way analysis of structural health monitoring data,” *Neurocomputing*, vol. 80, pp. 119-128, Mar. 2012.

[26] A. Mojtahedi, M. A. Lotfollahi Yaghin, Y. Hassanzadeh, M. M. Ettefagh, M. H. Aminfar, and A. B. Aghdam, “Developing a robust SHM method for offshore jacket platform using model updating and fuzzy logic system,” *Applied Ocean Research*, vol. 33, no. 4, pp. 398-411, Oct. 2011.

[27] P. Giaccari, G. R. Dunkel, L. Humbert, J. Botsis, H. G. Limberger, and R. P. Salathé, “On a direct determination of non-uniform internal strain fields using fibre Bragg gratings,” *Smart Materials and Structures*, vol. 14, no. 1, pp. 127-136, Feb. 2005.

[28] W. W. Morey, J. R. Dunphy, and G. Meltz, “Multiplexing fiber bragg grating sensors,” *Fiber and Integrated Optics*, vol. 10, no. 4, pp. 351-360, Oct. 1991.

[29] W. R. Habel, “STABILITY AND RELIABILITY OF FIBER-OPTIC MEASUREMENT SYSTEMS - BASIC CONDITIONS FOR SUCCESSFUL LONG-TERM STRUCTURAL HEALTH MONITORING,” in *Sensing Issues in Civil Structural Health Monitoring*, F. Ansari, Ed. Dordrecth, The Netherlands: Springer, 2005, pp. 341-351.

[30] D. A. Harold and J. C. J. Duke, “Long Term Durability Assessment of Optical Fiber Sensors,” *AIP Conference Proceedings*, vol. 820, no. 1, pp. 1718-1725, 2006.

[31] D. Hull and T. W. Clyne, *An Introduction to Composite Materials*, 2nd ed. Chambridge, Great Britain: Cambridge University Press, 1996.

[32] I. Robertson, “Photographs.” Department of Civil and Environmental Engineering, University of Hawai‘i at Mānoa, Honolulu, HI, 2008.

[33] Shigemura, Lau, and Sakanashi, “Final report, bridge no. 911, Salt Lake Boulevard Bridge over Halwa Stream.,” Honolulu, HI, 2001.